Berichte aus dem
Institut für Meereskunde
an der
Christian-Albrechts-Universität zu Kiel

No. 306

The influence of phytoplankton aggregation on sedimentation – A model study

von
Iris Kriest

Kopien dieser Arbeit können bezogen werden über
Institut für Meereskunde
Abteilung Marine Planktologie
Düsternbrooker Weg 20
D-24105 Kiel

Diese Arbeit wurde als Dissertation von der
Mathematisch-Naturwissenschaftlichen Fakultät
der Christian-Albrechts-Universität zu Kiel angenommen

Contents

1 Introduction 1

2 Phytoplankton aggregates and marine snow 5
2.1 The biology of marine aggregates 5
2.2 Measurement of marine particles and aggregates 6
2.3 The size distribution of particles in the ocean 7
2.4 Aggregation of particles in the ocean 9
2.5 Effects of aggregation in ecological models 13

3 The 0-dimensional model 15
3.1 Model structure 15
3.1.1 Mass balances 15
3.1.2 Representation of aggregates 15
3.1.3 Sinking of phytoplankton cells 17
3.1.4 Aggregation of particles 18
3.1.5 Cell growth, colony formation and particle seperation 18
3.2 Model Setup 19
3.3 Results and discussion 20

4 The 1-dimensional model 27
4.1 Model Structure 27
4.1.1 Mass balances 28
4.1.2 Implementation of sedimentation and aggregation 29
4.1.3 Colony formation and aggregate fragmentation 31
4.2 Model Setup 32
4.3 Results 33
4.3.1 The Base Run 33
4.3.2 Experiments 36
4.4 Discussion 41

5 Simulations for the Northeastern North Atlantic 45
5.1 Model structure 45
5.1.1 Mass balances 47
5.2 Model Setup 47
5.3 Results and discussion 50
5.3.1 The Base Run 50
5.3.2 Scenario "Sticky" 54
5.3.3 The "Detritus" Scenario 55
5.4 Discussion 57

6 Simulations for the Arabian Sea 61
6.1 Hydrography and biology of the Arabian Sea 61
6.1.1 Hydrography 61
6.1.2 Biogeochemistry 63
6.1.3 The JGOFS Process Study 1995 – Cruise METEOR 32/5 65
6.2 Model setup 70
6.3 Simulations for Station S15 (10°N 65°E) 73
6.3.1 The Base Run 73

6.3.2 Scenario "Sticky" . . . .
6.3.3 The "Detritus" Scenario . . . .
6.4 Simulations for Station S04 (17°N 60°E) . . . .
6.4.1 The base run with climatological forcing . . . .
6.4.2 The base run with nitrate intrusion . . . .
6.4.3 Scenario "Sticky" . . . .
6.4.4 The "Detritus" scenario 1
6.4.5 Model and observed sedimentation at station S04 1
6.5 Comparison and discussion 1

7 Discussion 1(
7.1 The influence of aggregation in different oceanic regimes 1
7.2 Implications for biogeochemical models 1
7.3 Outlook: Model and reality 1

8 Summary/Zusammenfassung 1

References 1

A Solutions 1
A.1 Aggregation in the 0D-model 1
A.2 Sedimentation in the 1D-model 1
A.3 Aggregation in the 1D-model 1

B List of Symbols 1

6.3.2 Scenario "Sticky" 80
6.3.3 The "Detritus" Scenario 82
6.4 Simulations for Station S04 (17°N 60°E) 85
6.4.1 The base run with climatological forcing 85
6.4.2 The base run with nitrate intrusion 93
6.4.3 Scenario "Sticky" 99
6.4.4 The "Detritus" scenario 101
6.4.5 Model and observed sedimentation at station S04 101
6.5 Comparison and discussion 104

7 Discussion **109**
7.1 The influence of aggregation in different oceanic regimes 109
7.2 Implications for biogeochemical models 112
7.3 Outlook: Model and reality 114

8 Summary/Zusammenfassung **117**

References **123**

A Solutions **131**
A.1 Aggregation in the 0D-model 131
A.2 Sedimentation in the 1D-model 131
A.3 Aggregation in the 1D-model 132

B List of Symbols **135**

1 Introduction

Particulate organic matter in the ocean is important as a pool of carbon, a food source and as a vehicle for the removal of carbon from the upper, well-lit layers that are in contact with the atmosphere. The removal of particulate organic carbon takes place via the sedimentation of particles that sink through the water instead of simply moving with it. Sinking of organic carbon away from the surface thus enhances the capacity of the ocean to absorb carbon dioxide from the atmosphere via the so-called "biological pump", i.e the process of uptake of dissolved inorganic carbon by phytoplankton and its subsequent transport to the ocean interior by sedimentation.

The amount and the timing of sedimentation of organic matter from the upper layers of the ocean depends on the amount of organic matter in these layers, and on its sinking speed. These in turn depend on the structure of the pelagic ecosystem, which mainly governs how much of the primary production is being recycled by microbial degradation and grazing. As the biomass and composition of this system in many regions of the ocean shows strong seasonal variability, it is evident that the flux of organic mass is in general not a steady input of matter to the sediment, but comes in the form of large pulses, especially following phytoplankton blooms, when high biomass can be found in the euphotic zone (Billet *et al.*, 1983; Haake *et al.*, 1993; Beaulieu and Smith Jr., 1998). Besides the occurrence of high biomass in the euphotic zone, a high sinking speed is necessary to explain the rapid sedimentation of bloom type material. Two different explanations have often been proposed for the occurence of sedimentation pulses. One pathway can be seen in the sedimentation of zooplankton fecal pellets, which can settle at a sinking velocity of several hundreds of meters per day (Fowler and Knauer, 1986; Noji, 1991). The second pathway is via the sinking of live or dead phytoplankton cells. These cells are generally of small size, sinking less than 1 m d^{-1} if at all (Smayda, 1970; Bienfang, 1981). Aggregation may increase their size and sinking speed. For example, aggregates of phytoplankton of several millimeters in diameter have been found in several regions of the coastal and open ocean (Billet *et al.*, 1983; Lampitt, 1985; Alldredge and Gotschalk, 1989; Riebesell, 1991). These aggregates show sinking velocities of hundreds of meters per day (Alldredge and Gotschalk, 1988), depending on their size. An increase of sinking speed with increasing aggregate or colony size has also been found by Smayda (1970). From the time between the appearance of high surface phytoplankton biomass and the deposition of phytodetritus on the sea floor

Lampitt (1985) calculated sinking speeds of 100 to 150 m d^{-1}.

The formation of large aggregates of phytoplankton cells may happen by a variety of processes such as zooplankton grazing and defecation, mucus feeding webs etc. (see Alldredge and Silver, 1988). Physical aggregation, i.e. the collision of phytoplankton cells by physical mechanisms and their attachment to each other, may happen without the mediation of zooplankton shortly after the onset of a bloom, when there is no or little zooplankton (Smetacek, 1985). Because aggregation of phytoplankton cells by collision depends on number and size of the particles (McCave, 1984) and on their stickiness (see also chapter 2 for the biology, measurement and theoretical description of marine aggregates), the rate at which the particle size distribution changes strongly depends on the ecological state of the system.

It is therefore of interest to investigate how the particle size distribution and its sinking speed in a model of the pelagic ecosystem change with time, how they affect the shallow and deep flux of organic matter, and how the different processes contribute to this change in sedimentation. This has been done so far in models that are explicitely designed to investigate aggregation and consider many discrete size classes (Jackson, 1990; Riebesell and Wolf-Gladrow, 1992; Hill, 1992). Such models have a high computational cost, so that it would not be possible to use them in models that also have a detailed horizontal and vertical resolution of water movement.

When biogeochemical models consider sinking, they have usually one and at most three classes of particles each with a constant sinking speed (Evans and Garçon 1997). Fasham *et al.* (1990) could not decide on a single correct detrital sinking speed, and reported results from their plankton ecosystem model with two different sinking speeds; Slater *et al.* (1993) did likewise when they investigated the same model in a 3-dimensional setting at ocean-basin scales.

Here a new technique for representing the distribution of phytoplankton size distribution and sinking speed is presented. Numbers and total mass of particles are treated as separate state variables in the model, each obeying its own conservation law, so that the size distribution or the average aggregate size and sinking speed are themselves dynamical variables. The main questions to be addressed in this work are how important it is to take account of seasonally variable sinking speeds, and how accurate this new representation is. There are two representations for phytoplankton aggregation and sinking: one is concerned with the representation of aggregation in a well mixed parcel of water in the upper water column,

representative e.g. for the mixed layer, and one with the representation of aggregates in a vertically resolved water column. The second approach requires slightly different algorithms for aggregation and sedimentation, so they are presented in two different chapters. The first approach, hereafter called the box model (chapter 3), serves the purpose of comparing the outcome of the representation of the size–continuous model with the results of previous, size–discrete models (Jackson, 1990; Riebesell and Wolf-Gladrow, 1992). Experiments performed with this model give an overview on the importance of some of the parameters for phytoplankton growth and sedimentation. The second approach modifies the equations as presented in the first approach to fit into a vertically resolved 1-D model of ocean biogeochemistry (chapter 4). The results of this model are again checked vs. the box model, and again experiments are performed to test the influence of the vertical resolution on sensitivity of the model to alterations in parameters. The importance of phytoplankton aggregation on ocean biogeochemistry is then tested with simulations for a site in the Northern North Atlantic (chapter 5) and two different sites in the Arabian Sea (chapter 6). To provide the possibility to estimate the relative contribution of phytoplankton and pellet sedimentation to total flux in these simulations, zooplankton and fecal pellets have been added to the model.

2 Phytoplankton aggregates and marine snow

2.1 The biology of marine aggregates

Particles in the ocean come in a range of sizes covering many orders of magnitude. New particles (large organic molecules, dead or living phytoplankton cells, fecal pellets, etc.) are generally small (a few micrometres in diameter). Although small particles like this are usually the most abundant, aggregates 0.5 mm or greater in diameter ("marine snow") can be important for sedimentation, and for the functioning of the biological system in the pelagial.

There are different pathways for the production of marine aggregates. One is *de novo* production by zooplankton, e.g. tunicate houses and discarded mucus feeding webs (Alldredge and Silver, 1988). Another pathway is the collision and subsequent aggregation of particles, especially phytoplankton cells, by physical or kinetic aggregation. A third pathway has been proposed by Passow *et al.* (1994) via production of TEP (transparent exopolymer particles) and the subsequent collision of these large organic molecules, plus scavenging of phytoplankton cells. It should be noted that this last mechanism introduces a transition from dissolved organic matter to particulate organic matter by merely physical, and not biological interactions.

As a consequence, marine snow can be present in variety of compositions and forms. It comes in forms of globules, clouds and stringers, i.e. elongated, comete shaped aggregates (for terminology see Stachowitsch *et al.*, 1990). In the Adriatic Sea Bochdansky and Herndl (1992a) found globules and stringers in 1989 and 1990, and dense clouds of several meters in length in the summer of 1991. Beside aggregates consisting mainly of phytoplankton cells (Alldredge and Gotschalk, 1989; Alldredge and Gotschalk, 1990; Alldredge *et al.*, 1995; Riebesell and Wolf-Gladrow, 1992) – phytoplankton in marine snow can account for 30% of total Chl *a* of the water column – aggregates have been found to be colonized by polychaete larve, and fecal pellets have been found to be enriched in marine snow by a factor ranging up to 3800 (Bochdansky and Herndl, 1992b). Enrichment of bacteria, cyanobacteria and autotrophic picoplankton on marine aggregates has for example been found by e.g. Lampitt *et al.* (1993b) in the Northern North Atlantic. Because marine snow or aggregates often consists of photosynthetically active diatoms e.g. of the genera *Chaetoceros* and *Nitzschia*, they can account for a large fraction (up to 40%) of photosynthesis in the water column (Alldredge and Gotschalk, 1990; Kaltenböck and Herndl, 1992).

Aggregates also serve as a food source for larger zooplankton. In laboratory experiments Hansen (1992) found that three calanoid copepod species (*Temora longicornis*, *Centropages hamatus* and *Calanus finmarchicus*) were able to feed on colonies of the prymnesiophyte *Phaeocystis sp.*, with a preference of the copepods for colonies, and of female copepods even for larger colonies ($>$ 0.1 mm). No grazing could be detected for *Acartia clausi* when fed with *Phaeocystis*. Nevertheless, in situ measurements of copepod ingestion rate during a *Phaeocystis* bloom in the North Sea showed that copepods grazing was of little importance for the development of the bloom (Hansen, 1992). Significant grazing of *Acartia clausi* on aggregates was detected by Bochdansky and Herndl (1992a) when feeding the copepod with aggregates consisting of *Nitzschia closterium* and with aggregates which were produced from natural seawater collected in the Gulf of Trieste by rolling tank incubations. Lampitt *et al.* (1993b) discuss feeding of the amphipod *Themisto compressa* on marine snow containing large amounts of autotrophic picoplankton as a short cut in the food web. By aggregating, or by being scavenged by larger aggregates, small cells become available to larger zooplankton.

The specific density of aggregates usually decreases with increasing aggregate size due to the space between the single constituents, or the contribution of matter with a low density, as, for exmaple, TEP, to the aggregate mass (Alldredge and Gotschalk, 1988; Engel, 1998). As a consequence, their excess density decreases with increasing size, and thus the sinking speed relates to diameter by a power less than two (as would be given by Stoke's law and constant density) but larger than zero (Alldredge and Gotschalk, 1988; Alldredge and Gotschalk, 1989). Fecal pellets can be effectively scavenged by marine snow (Bochdansky and Herndl, 1992b). Because aggregates in the Northern Adriatic Sea tend to remain more or less neutrally buoyant over several weeks (Kaltenböck and Herndl, 1992), trapping of fecal pellets in this type of aggregates has been considered to even prolong the residence time of pellets in the upper layers of the water column, and thus diminish their flux to the sediment.

2.2 Measurement of marine particles and aggregates

There are various problems associated with the measurement of large aggregates, most of which lead to an underestimate of their abundance. Large particles are generally fragile, and easily break apart during collection and handling (Alldredge and Gotschalk, 1988).

Due to the low abundance of large aggregates (at most few tens per cubic metre or less), with standard collection methods, where only a few millilitres are sampled, these large aggregates are likely to be missed. The problem of breakage and undersampling has been overcome by the collection of aggregates by large volume water samples or filtration systems (e.g. Lampitt *et al.*, 1993b), and by *in-situ* collection of aggregates by divers (see Alldredge and Silver, 1988b). Sampling of aggregates by SCUBA divers is only applicable for the nearshore environment, but not for the open ocean. The Coulter Counter, which can be used for sampling particles aboard research vessels in the open ocean is only capable of measuring particles between ca. 1 - 100 μm, so larger particles have to be collected and counted by other methods. Recently, the use of underwater optical systems (Honjo *et al.*, 1984; Lampitt, 1985; Lampitt *et al.*, 1993b; Kilps *et al.*, 1994; Beaulieu and Smith Jr., 1998) have revealed the existence of large aggregates and their importance for open ocean processes. Because optical analysis of aggregates usually starts at larger sizes of one to several 100 μm depending on the resolution, investigations on how to combine the results of different methods such as Coulter Counter technique and optical analysis are necessary. One step towards a combination of both techniques, which gives an insight on the size distribution over a large range of particle size can be found in Jackson *et al.* (1995).

2.3 The size distribution of particles in the ocean

Different functions have been proposed for the representation of marine size distributions of particles as measured by various methods such as Coulter Counter technique, scanning electron microscopy or light scattering. A log-normal function has been proposed by Lambert *et al.* (1981) and Jonasz and Fournier (1996). Zuur and Nyffeler (1992) found that the size spectrum could be well described by the sum of two exponential functions, for the size spectrum from zero to infinity. On the basis of observations of particles $> 1\mu$m in oceanic waters, it has been found that the particle size distribution may also be well described by a power law distribution (McCave, 1984):

$$p(\theta) = \frac{\mathrm{d}\,N}{\mathrm{d}\,\theta} = A\theta^{-\epsilon} \tag{1}$$

where $p(\theta)$ is the particle size distribution as a function of particles diameter θ, $\mathrm{d}N$ is the number concentration of particles in the size range from θ to $\theta + \mathrm{d}\theta$ and A is a coefficient related to the total number of particles present in a water parcel. The positive exponent ϵ

can then be evaluated by log-log plots of $n(\theta)$ vs. θ. Expressed as cumulative number of particles $P(m)$ (particles larger than a given size m), equation 1 then becomes

$$P(m) = A \int_m^\infty \theta^{-\epsilon} d\theta = A \frac{m^{1-\epsilon}}{\epsilon - 1} \qquad \text{if} \qquad \epsilon > 1 \tag{2}$$

Examples of two cumulative size distributions are given in figure 1. If there are many small particles, the slope of the size distribution becomes steeper (i.e. ϵ increases, broken line in figure 1), if there are many large particles, the slope of the size distribution becomes lower (solid line). The effect of a flattening of the size distribution (decrease in ϵ) can either be achieved by reducing the number of particles, or by increasing their mass. The former process has an effect on the size distribution coefficient A, i.e. on the intercept of the curve at $\theta = m$ or the total number of particles $\geq m$, the latter only has an effect on the slope ϵ.

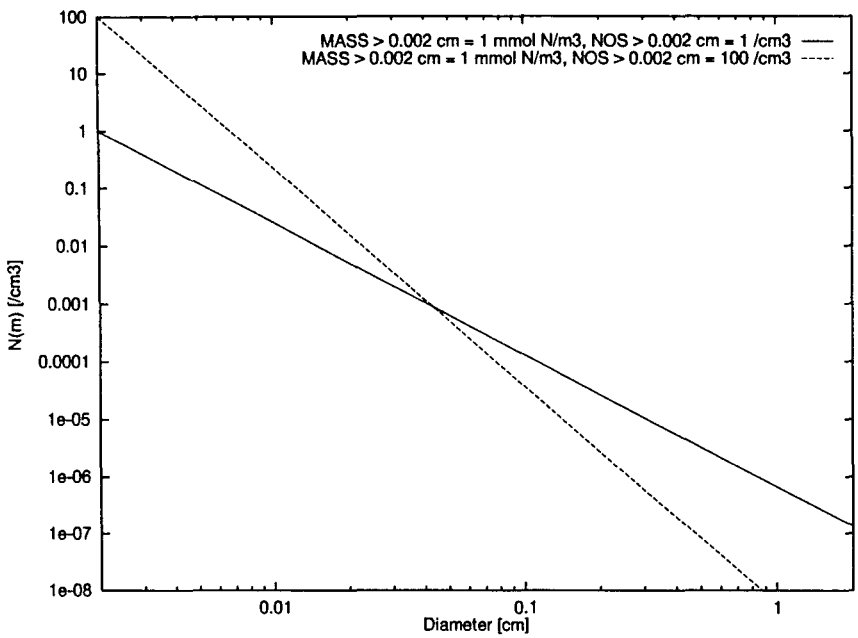

Figure 1: Example of two cumulative particle size distributions. The x-axis represents the diameter of particles from 20 μm to 2 cm on a logarithmic scale, the y-axis the of particles large than a given size (log scale). The exponents ϵ for the size distribution are 3.29 (solid line) and 4.79 (broken line). The total number of particles > 20μm is 1 (intercept of solid line with y-axis) and 100 (intercept of broken line with y-axis). For further explanations see text.

If θ is the diameter of particles, and the particles are assumed to be of spherical shape, with the volume given by $v = \pi/6\,\theta^3$, then the volume of particles larger than a given size, $V(m)$ can be evaluated according to

$$V(m) = \int_m^\infty \frac{\pi}{6} A\theta^{(3-\epsilon)} \mathrm{d}\theta = \frac{A\pi m^{4-\epsilon}}{6(\epsilon - 4)} \qquad \text{if} \qquad \epsilon > 4 \tag{3}$$

Typical values for the exponent of the cumulative number distribution that have been found using Coulter Counter techniques (which, in contrast to the equations given above, only measures within a limited size range, see above) lie in the range of $\epsilon = 4$ for oceanic waters, which implies equal particle volume in logarithmically increasing size classes (so-called "flat distributions"). It is evident that equation 3 can only be solved for $\epsilon > 4$. If the particles were of uniform specific density (i.e. the specific density does not vary with diameter), this means that total mass would be infinite. If instead the specific density of the aggregates is related to aggregate diameter by a power function with a negative exponent, the particles become less dense with increasing size. The function that relates mass of particles to diameter can than be described by a function $C\theta^\zeta$, where ζ may be less than 3. This has in fact been found by several authors (Li and Logan, 1995; Mullin *et al.*, 1966; Alldredge and Gotschalk, 1988). The cumulative mass distribution $M(\theta)$ is then given by

$$M(m) = AC \int_m^\infty \theta^{(\zeta-\epsilon)} \mathrm{d}\theta = \frac{AC m^{1+\zeta-\epsilon}}{(\epsilon - \zeta - 1)} \qquad \text{if} \qquad \epsilon > \zeta + 1 \tag{4}$$

Again, it can be seen that ϵ cannot be smaller than $1 + \zeta$, or the total mass of all particles would be infinite.

2.4 Aggregation of particles in the ocean

The theory of particle aggregation in the ocean is well worked out. The collision of particles depends on the rate at which particles get into close proximity to each other: this rate depends on their density, their size, and the speed of the particles relative to each other. For a size range from m to ∞, the total number of collisions between all particles is given by

$$\frac{\mathrm{d}N(m)}{\mathrm{d}t} = -0.5 \int_m^\infty \int_m^\infty \beta(\theta, \Theta)\, p(\theta)\, p(\Theta)\, \mathrm{d}\theta\, \mathrm{d}\Theta \tag{5}$$

where $p(\theta)$ and $p(\Theta)$ are the particle number distributions as defined above, and $\beta(\theta, \Theta)$ is the collision kernel. McCave (1984) in his theoretical work has shown that the aggregation equation for aerosol dynamics may be applied to particle aggregation in the ocean. Three

main processes determine the speed of particles relative to each other: turbulent and laminar shear, differential settlement and Brownian motion. Collisions due to Brownian motion mainly affect particles of small size (ca. 1–10 μm), and will be neglected in this work. For large particles, shear is the dominant mechanism in bringing particles together.

Jackson (1990) used the equations for turbulent shear and differential settlement, together with the formulation of collision efficiency according to Pruppacher and Klett (1978). The kernel (β_{shear}) for the equation of shear depends on the cube of the sum of the diameters of two particles, times the rate of turbulent shear:

$$\beta_{shear}(\theta, \Theta) = 0.163\, shear\, (\theta + \Theta)^3 \tag{6}$$

where θ and Θ are the diameters of two particles, and *shear* is the turbulent shear. Differences in the fluid velocity carry the particles to each other. The larger the particles are, the higher is the chance that they touch each other. Due to the power of three shear mainly affects the collisions of large particles and the function increases with increasing particle diameters (see also figure 2).

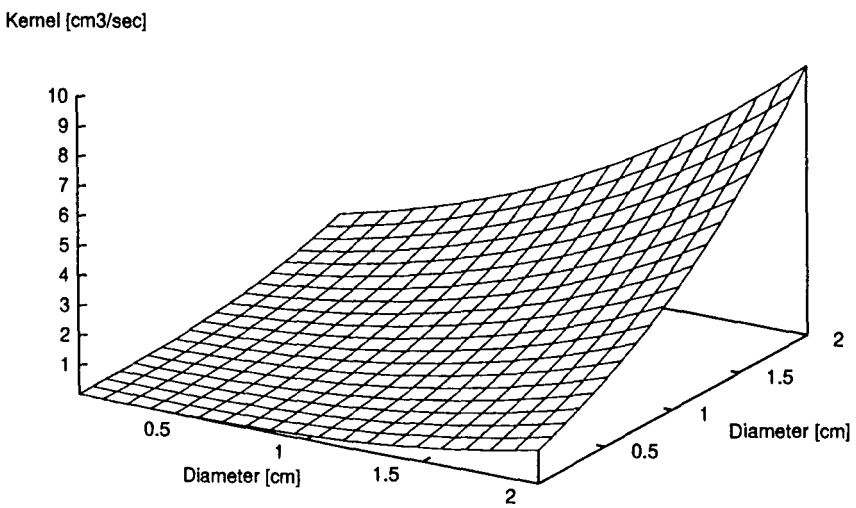

Figure 2: Collision kernel for turbulent shear. The x- and y-axis represent the diameter of particles from 20 μm to 2 cm, the z-axis the number of collisions due to turbulent shear, according to function 6, with shear = 0.84 s^{-1}. For further explanations see text.

The second mechanism is differential settlement of particles. If sinking velocity is related to diameter, then two particles of different sizes settle at different speeds and one particle can overtake and contact the other. The area that two spherical particles can occupy while sinking is given by the area of the circle that is defined by the sum of their particles. Thus

the settlement kernel β_{sett} is given by the differences in the sinking speed of two particles, times the area they pass through:

$$\beta_{sett}(\theta, \Theta) = 0.25\,\pi\,(\theta + \Theta)^2\,(w(\Theta) - w(\theta))\,(E_C + E_D) \tag{7}$$

where $w(\theta)$ and $w(\Theta)$ is the sinking speed of the particles of size θ and Θ, respectively. E_C and E_D are the contact efficiency and the diffusion efficiency, respectively. As diffusion is negligible for particles $\gg 1\mu$m, taking the contact efficiency, i.e. the probability that two particles close to each other come into contact, as formulated by Pruppacher and Klett (1978):

$$E_C = \frac{(\theta/\Theta)^2}{2(1+\theta/\Theta)^2} \qquad \text{with} \qquad \theta < \Theta \tag{8}$$

equation 7 reads

$$\beta_{sett}(\theta, \Theta) = 0.125\,\pi\,\theta^2\,(w(\Theta) - w(\theta)) \qquad \text{with} \qquad \theta < \Theta \tag{9}$$

(See also Jackson, 1990, who uses the same formulation for the evaluation of the settlement kernel.) The function is zero for $\theta = \Theta$ if the sinking - diameter relationship for both size classes involved is the same (see also figure 3).

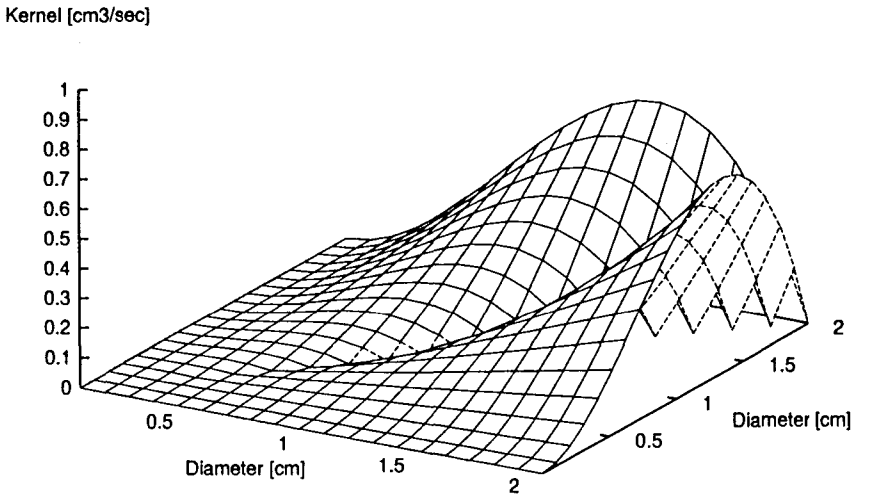

Figure 3: Collision kernel for differential settlement. The x- and y-axis represent the diameter of particles from 20 μm to 2 cm, the z-axis the number of collisions due to differential settlement, according to function 9, with $w(\theta) = 1.1\theta^{1.17}$. For further explanations see text.

The joint effect of the two processes is assumed to be given by the sum of their kernels. This sum times the number of particles in the corresponding size class finally gives the number of collisions that occur between those particles. Because usually there are many more small particles than large ones (see also figure 1) the shape of the particle size distribution will counteract the effect of increasing particle size on the collision kernel.

Depending on the sinking-diameter relationship that is used, the settlement kernel generally may depend as strongly on the diameter as the shear kernel (Stoke's sinking with a power of two) or show a weaker dependence (see figure 3 for $w(\theta) = 1.1\theta^{1.17}$). The collision kernel does not increase monotonically with increasing diameter of both particles involved in the collision, as it is the case in the shear kernel, but shows a maximum at a certain relationship of θ and Θ (figure 3). An maximum of this function can be found at the point $\frac{\theta}{\Theta} = (\frac{2}{2+\eta})^{1/\eta}$, where η is the exponent that relates sinking speed to the diameter, at which the first derivative vanishes.

If for example, η is 1.17, as used in many aggregation models (Jackson, 1990; Riebesell and Wolf-Gladrow, 1992), the smaller particle has to be about two third (0.675) of the size of the larger particle to yield the largest value for the collision kernel (see also figure 3). Taking, for example, a particle of diameter 2 cm, a shear rate of 0.84 s^{-1} and a sinking relationship of the form $w(\theta) = 1.1\,\theta^{1.17}$, the maximum of the shear collision kernel that can be achieved is $0.163 \times 8 \times 2^3 \approx 10$ cm^3 s^{-1}, and the maximum rate of due to differential settlement is $1.1 \times \pi \times 0.125 \times 0.675^2 \times 2^{3.17}(1 - 0.697^{1.17}) \approx 0.65$ cm^3 s^{-1}. The maximum collision rate due to shear is more than one order of magnitude higher than the collision rate due to differential settlement, if at least one particle is of size 2 cm. Summarizing, when there is high turbulent shear, collisions due to shear are more effective in bringing particles together than collisions due to differential settlement. Yet this very large size has been chosen for illustrative purposes - because there will be very few of those large aggregates (about 10^{-8} cm^{-3} (see figure 1) despite of the high collision kernel at this large sizes, most collisions will happen between smaller aggregates, because they are more abundant.

To aggregate, two particles must collide and stick together. The probability that two particles stick together after collision is given by the parameter of stickiness (*stick*), which may vary between 0 (particles do not stick together) and 1 (every collision creates a new aggregate). Empirical investigations show, that in reality stickiness varies largely and may correlate to different factors such as type of aggregate, nutritional status, etc. (Alldredge and McGillivary, 1991; Kiørboe *et al.*, 1990; Dam and Drapeau, 1995). Especially the

existence of transparent exopolymer particles (TEP) (Dam and Drapeau, 1995) or mucopolysaccharide sheaths (Engel, 1998) produced by diatoms have been found to increase stickiness of particles. Also the spines that many diatoms bear can have the effect of entangling the cells with each other (Hustedt, 1930), thus giving a kind of morphological stickiness to the algae.

Aggregation reduces the number of particles, but conserves mass - the new particle's mass is given by the sum of the masses of the two particles involved in the aggregation event. Thus it has an effect on the particle's size and size distribution via the reduction of numbers. The same effect of a flattening of the size distribution may be exhibited by the addition of mass while maintaining the total number of aggregates. This effect can be found if cells inside aggregates grow, or even divide and stick together after division, and may happen by several mechanisms, e.g. production of extracellular mucus surrounding the cells or by entangling of cells bearing spines and other protuberances, as it is the case for the setose chain-forming diatom *Chaetoceros* or the colonies of *Nitzschia* and the starlike *Asterionella* (Hustedt, 1930). This process, which is generally called "colony formation", can often been found in diatoms.

2.5 Effects of aggregation in ecological models

Models that combine aggregation theory and/or phytoplankton growth often use many size classes (e.g. Jackson, 1990; Riebesell und Wolf-Gladrow, 1992) or involve the sectional representation approach presented by Gelbard *et al.* (Gelbard *et al.*, 1980; Jackson and Lochmann, 1992) with fewer size classes. Jackson (1990) showed that in an exponentially growing population of phytoplankton cells, when cell concentrations were high enough, aggregation was sufficient to produce many large particles that sank rapidly and prevented any further population growth, even without biological packaging into fecal pellets. There is a rapid increase in the number of large aggregates once particles become sufficiently abundant. Riebesell and Wolf-Gladrow (1992) investigated further the effects at depth, incorporating nutrient exhaustion and the degradation of slower-sinking particles at intermediate depths, and the influence of colony formation. Both of these models represented the particle size distribution by hundreds of individual size classes. Riebesell and Wolf-Gladrow (1992) had 1000 size classes, and thus half a million pairs of size classes whose propensity to collide must be computed. The outcome of these models is mostly given

as number of aggregates per size class and day, or as mass per size class and day. These models have the advantage of providing a size distribution, which is not constrained to decreasing particle numbers and mass with increasing particle size, but may produce the above mentioned "humped" spectra over a certain range of particle sizes, but on the other hand have a rather high computational cost. The next sections will present a different approach based on the assumption, that the particle size distribution can be presented by a power law, which then only requires one additional variable beside the phytoplankton mass to compute phytoplankton aggregation.

3 The 0-dimensional model

The simulations and tests performed with a 0-dimensional model of a single well-mixed box including phytoplankton aggregation address the question of the importance of aggregation on mass flux out of a mixed layer of constant depth. For this purpose the aggregation equations as formulated by Jackson (1990) have been solved and implemeted in a box model for the oceanic mixed layer, as presented in Evans and Parslow (1985). To check for the accuracy of the parameterization of aggregation, the model has been tested with respect to previous, size resolved models (Jackson, 1990; Riebesell and Wolf-Gladrow, 1992).

3.1 Model structure

The model presented in this chapter is a 0-dimensional model of the flow of nitrogen from dissolved inorganic form (NO3) to phytoplankton in the mixed layer. The concentration of phytoplankton is computed in units of nitrogen (PHY: mmol N m^{-3}) and numbers (PHYNOS: cm^{-3}). The model does not include the effects of light limitation or exchange with deeper layers. All phytoplankton cells have the same growth rate regardless what size of aggregate they are in. It is solved using a fourth-order Runge-Kutta routine with adaptive stepsize.

3.1.1 Mass balances

Mass flows from NO3 to PHY, and thence out of the system by sinking. Phytoplankton growth is limited by the nutrient availability using a Monod function of nitrate concentration with half saturation constant k_{NO3}. Phytoplankton loss Ψ due to sedimentation out of the mixed layer depends on aggregate size and will be described in the next section.

$$\frac{\mathrm{dPHY}}{\mathrm{d}t} = \frac{\mathrm{NO3}}{k_{\mathrm{NO3}} + \mathrm{NO3}}\mathrm{PHY} - \Psi \tag{10}$$

$$\frac{\mathrm{dNO3}}{\mathrm{d}t} = -\frac{\mathrm{NO3}}{k_{\mathrm{NO3}} + \mathrm{NO3}}\mathrm{PHY} \tag{11}$$

3.1.2 Representation of aggregates

The main novelty of this approach is that it keeps track of the number as well as the mass of aggregates, and makes an assumption so that these two quantities suffice to fully describe

the distribution of aggregate sizes. Specifically, it is assumed that this distribution is a function of the aggregate diameter θ and follows a power law, as described in chapter 2:

$$p(\theta) = A\,\theta^{-\epsilon} \quad m < \theta < \infty \tag{12}$$

where m is the diameter of a single cell. A large ϵ means that there are many small particles, whereas a small epsilon describes a size distribution with a predominance of large particles. The total concentration (cm^{-3}) of all aggregates $> m$ can then be evaluated by

$$\mathrm{PHYNOS} = A \int_m^\infty \theta^{-\epsilon}\,\mathrm{d}\theta = A\,\frac{m^{1-\epsilon}}{\epsilon - 1} \qquad \text{if} \qquad \epsilon > 1 \tag{13}$$

Let C_m be the mass of a single cell, so that

$$N = \frac{\mathrm{PHY}}{\mathrm{PHYNOS}\ C_m} \tag{14}$$

is the average number of cells in an aggregate. There is empirical evidence that the density of phytoplankton aggregates decreases with increasing aggregate size, so their mass grows more slowly than the cube of their diameter (Alldredge and Gotschalk, 1988). If the mass (nmol N) of a particle of diameter θ is $C\,\theta^{\zeta}$, then the total mass of phytoplankton PHY can be represented by

$$\mathrm{PHY} = AC \int_m^\infty \theta^{\zeta-\epsilon}\,\mathrm{d}\theta = AC_m\,\frac{m^{1+\zeta-\epsilon}}{\epsilon - 1 - \zeta} \qquad \text{if} \qquad \epsilon > \zeta + 1 \tag{15}$$

Dividing equations 13 and 15 and solving for ϵ then gives

$$\epsilon = \frac{(1+\zeta)\,\mathrm{PHY} - C_m\,\mathrm{PHYNOS}}{\mathrm{PHY} - C_m\,\mathrm{PHYNOS}} \quad \text{or equivalently} \quad \epsilon = \frac{(1+\zeta)N - 1}{N - 1}. \tag{16}$$

Starting with $\epsilon > 1 + \zeta$, a necessary precondition for equation 15 to be valid, because the total mass of particles is finite, the model never gets out of the range of convergence (see chapter 2). If the particles were spheres of uniform density, C would be $\pi/6$ times a number for mass content per unit volume, and $\zeta = 3$. This work follows Jackson (1990) and Riebesell and Wolf-Gladrow (1992) by choosing $C = 4.3 \times 10^{-6}$ nmol $\mu\mathrm{m}^{-2.28} = 5.7 \times 10^{3}$ nmol $\mathrm{cm}^{-2.28}$ and $\zeta = 2.28$. The value of 2.28 also corresponds with what Li and Logan

(1995) found at the beginning of a bloom in a mesocosm experiment. An example for the evaluation of ϵ according to the equation 16 for different concentrations of particles $> 20\mu$m (1 and 100 cm^{-3}) while keeping total mass of particles constant at 1 mmol N m^{-3} is shown in figure 1 in the previous chapter.

3.1.3 Sinking of phytoplankton cells

The relation between sinking speed w and aggregate diameter θ has been described by a power law (Alldredge and Gotschalk, 1988; Smayda, 1970):

$$w(\theta) = B\,\theta^{\eta} \tag{17}$$

with $B = 1.1$ $cm^{-0.17}s^{-1}$ and $\eta = 1.17$ (Jackson, 1990). The contribution of sinking to the rate of change of concentration of numbers (Φ) or mass (Ψ) is the number or mass flux across the bottom of the mixed layer, divided by the mixed layer depth (MLD). Combining equation (17) with (13) and (15) gives:

$$\Phi = A\,\frac{B}{MLD}\int_m^{\infty}\theta^{\eta-\epsilon}\,d\theta = \text{PHYNOS}\,\frac{w_m}{MLD}\,\frac{\epsilon-1}{\epsilon-1-\eta} \qquad \text{if} \qquad \epsilon > \eta+1 \tag{18}$$

$$\Psi = A\,\frac{B}{MLD}\,C\int_m^{\infty}\theta^{\zeta+\eta-\epsilon}\,d\theta = \text{PHY}\,\frac{w_m}{MLD}\,\frac{\epsilon-1-\zeta}{\epsilon-1-\zeta-\eta} \qquad \text{if} \qquad \epsilon > \zeta+\eta+1 \tag{19}$$

where w_m is the sinking velocity of a cell as defined from equation 17. Because $\frac{\epsilon-1}{\epsilon-1-\eta} > 1$, the sinking velocity of snow particles is greater than w_m. Combining equations (13, 15, 18, 19, 16) yields an expression for the number of cells in the average particle sinking out of the mixed layer:

$$N_{\text{sink}} = \frac{\Psi}{\Phi C_m} = \frac{\epsilon-1-\eta}{\epsilon-1-\zeta-\eta} > N. \tag{20}$$

Sinking preferentially removes large particles and increases ϵ. The average mass sinking speed

$$\bar{w} = w_m\,\frac{\epsilon-1-\zeta}{\epsilon-1-\zeta-\eta} \tag{21}$$

corresponds to the (constant) detrital sinking speed parameter in other models as, for example, the model by Fasham *et al.* (1990); in this model it depends on phytoplankton mass and numbers, and is thus a dynamical variable.

3.1.4 Aggregation of particles

Small particles can collide and stick to form larger ones. The probability of collision between two particles is a function of the concentration of particles, their sizes, the intensity of turbulent shear in the water, and the difference of the settling velocities of two different particles (see chapter 2). To calculate the number of particles colliding (ξ), the master equations for both processes as formulated by Jackson (1990) have been converted to a size-continuous form and integrated over the range of sizes:

$$\xi = 0.5\ stick \int_m^\infty \int_m^\infty (\beta_{shear}(\theta,\Theta) + \beta_{sett}(\theta,\Theta))p(\theta)p(\Theta)\,\mathrm{d}\theta\,\mathrm{d}\Theta \tag{22}$$

where

$$\beta_{shear} = 0.163\ shear\ (\theta+\Theta)^3 \qquad \text{and}$$

$$\beta_{sett} = 0.125\,\pi\,B\,\theta^2\,(\Theta^\eta - \theta^\eta) \qquad \text{for all} \qquad \theta < \Theta$$

shear is a constant describing turbulent shear, and is assumed to be constant in the mixed layer, B and η are as in equation 17. The collision kernel of equation 22 is the sum of two parts β_{shear} and β_{sett}, describing the size dependence of aggregation on the rate of turbulent shear and differential settlement, respectively. The solution of the double integral from m to ∞ can be found in appendix A.1.

3.1.5 Cell growth, colony formation and particle seperation

Growth and division of phytoplankton aggregates will increase the number of particles only if the aggregates separate after division. Of course, solitary algae seperate immidiately after cell division. The probability of seperation thus depends on the mix of species in the phytoplankton community, being greater for dinoflagellates than for colony-forming species. In this model the species mix is presented through a single separation probability $0 \leq b \leq 1$ which does not change with time or with the size of the particle. For the sake of simplicity, in all but one of the experiments this parameter has been chosen to be 1

aggregate numbers, which means that both numbers and mass increase at the same rate, and phytoplankton growth has no effect on the particle size distribution, or on the average size of particles. By setting the parameter to a value < 1, the mass grows faster than the numbers, and the average size increases.

Combining all these processes yields the equation for change in aggregate numbers:

$$\frac{\mathrm{dPHYNOS}}{\mathrm{d}t} = b \frac{\mathrm{NO3}}{k_{\mathrm{NO3}} + \mathrm{NO3}} \mathrm{PHYNOS} - \Phi - \xi \tag{23}$$

3.2 Model Setup

Runs of the box model were designed to address two questions: how accurate is the representation of aggregation and variable sinking speed, and how necessary is it to consider aggregation and variable sinking speed, compared to a simulation with a model with constant sinking speed?

The question of accuracy will be addressed by running the model with 25 m deep mixed layer with constant physical forcing for 90 days, and comparing with the results of the 1000-component model of Jackson (1990) and Riebesell and Wolf-Gladrow (1992), including some of their experiments with the parameter values. The parameters are given in table 3. The half-saturation constant for NO3 uptake is so low that growth continues at almost its maximum rate until nitrate is exhausted. Scenario "Large" doubles the diameter of an individual cell. Scenario "Sticky" doubles the stickiness of phytoplankton. Scenario "Colony" decreases the seperation probability of phytoplankton to a value of 0.5 so that phytoplankton growth, as well as aggregation, can produce larger particles. In scenario "Single", all phytoplankton sinks at the same constant speed: the speed of a single cell. This model scenario determines the importance of aggregation for the development and the fate of a phytoplankton bloom.

The aggregation parameters in Table 1 were chosen to be as consistent as possible with existing size-discrete models for aggregation, especially Riebesell and Wolf-Gladrow (RW) (1992).

The model did not proof to be very sensitive to alterations in its N-content exponent ζ or the exponent that relates sinking speed to diameter (η). In fact, the model results presented here, using $\zeta = 2.28$ and $\eta = 1.17$ are almost the same as when simulating aggregation under the assumption that phytoplankton sink according to Stoke's law ($\eta = 2$) and that

Table 1: Parameters for biological and aggregation module. When two values are given for an aggregation parameter, the second is the value assigned in one of the changed scenarios.

Parameter	Symbol	Value	Unit
phytoplankton parameters			
maximum growth rate	μ_{PHY}	1	d^{-1}
half-sat. const. for NO3 uptake	k_{NO3}	0.050	mmol N m^{-3}
aggregation parameters			
shear rate	*shear*	0.84	s^{-1}
sinking exponent	η	1.17/0	-
sinking factor	B	1.05	$cm^{-0.17}$ sec^{-1}
stickiness	*stick*	0.1/0.2	-
seperation probability	b	1/0.5	-
cell size	m	0.002/0.004	cm
N content exponent	ζ	2.28	-
N content coefficient	C	5.67	nmol N $cm^{-2.28}$

the specific density of aggregates does not decrease with aggregate diameter ($\zeta = 3$, results not shown here). The main difference is that RW allow separation only in small aggregates. Therefore breakup probabilities used in the model presented here, for both standard run and colony experiments, are on average greater than the corresponding RW probabilities (Table 2).

Table 2: seperation probability in different models and model scenarios.

Size (cells per aggregate)	1	2-8	≥9
This model, standard	1	1	1
This model, colony	.5	.5	.5
Riebesell and Wolf-Gladrow (1992), base	1	0	0
Riebesell and Wolf-Gladrow (1992), colony	.8	.8	0

3.3 Results and discussion

The main focus of this presentation of the box model is to compare it with previous, size discrete models and to examine the effects of different scenarios on model behaviour. The

more general development of the phytoplankton bloom, its sinking speed and the mass sedimentation in 25 m depth are shown in the next chapter (4), together with the results of the vertically resolved model.

To examine the effects of simulating aggregation on a size continuum with respect to other models, the model results (ϵ, PHYNOS) have been converted to numbers of particles in certain size classes from 1 to 1000 cells per aggregate. Figure 4 shows the development of the phytoplankton particle size distribution under constant physical forcing. Starting from very low values (PHY =0.001) and a steep size distribution ($\epsilon = 8$ so that PHYNOS= 0.17 particles cm^{-3}) with few large cells, it takes 10 days for the bloom to develop, and particle numbers reach a maximum of 1400 particles per cubic cm.

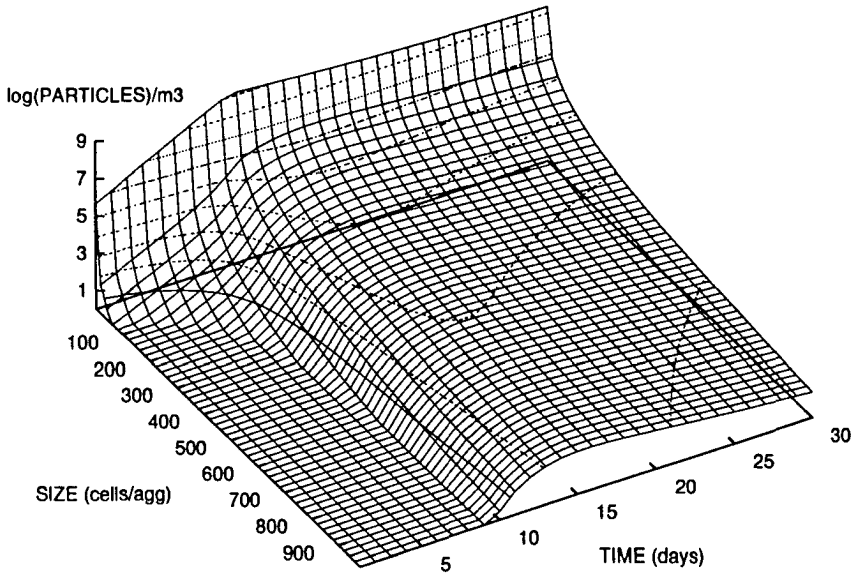

Figure 4: Development of particle size distribution in the mixed layer of 25 m with constant physical forcing. Time and particle size are plotted as linear scales as x-and y-axis, respectively, the logarithm of particle number concentration per cubic m is plotted on the z-axis.

The average particle size reaches a maximum value of 4.5 cells per aggregate on day 17, and then starts to decrease again due to settlement of large particles out of the mixed layer. Total number concentration as well as timing and shape of the development of particle size distribution look similar to the results presented by Jackson (1990) and Riebesell and Wolf-Gladrow (1992).

The model has been constructed so that all of the nitrate must be converted to phytoplankton and then sink; the differences among the experiments are only in how fast this happens. Figure 5 shows the fraction of total primary production so far that has already

been exported (i.e. total export up to this time divided by total production up to this time).

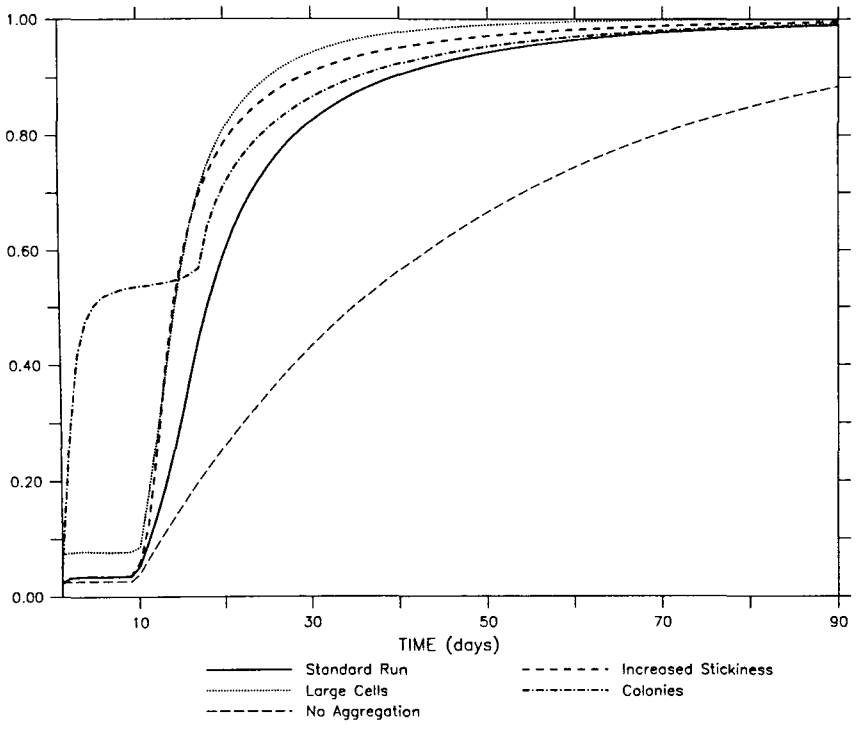

Figure 5: Export production (cumulative sedimentation divides by cumulative primary production) for the standard model and experiments.

The effects of colony formation are most dramatic during the time of high biological activity, because in this scenario phytoplankton grow at almost their maximum speed of almost 1 d^{-1} until day 17, when growth declines to 0 d^{-1} due to nitrate limitation. Colony formation depends linearly on phytoplankton concentration and can become apparent immediately; aggregation depends quadratically on phytoplankton concentration and can become apparent only after a certain amount of growth has taken place. From the first day on, the export production for colony formation is more than 50 % whereas for the other scenarios only about 2-7 % is exported. This pattern changes dramatically on day 10 (when all of the nitrate has been taken up by phytoplankton) for all simulations including aggregation, showing a rapid increase in export production. By day 30 of the simulation the difference between export production between all aggregation scenarios are only about 10 %. The "Single" scenario takes much longer before it too finally exports all of the production.

The export of particulate matter on shorter time scales may be important for other biological processes such as grazing and degradation, so the effects of different modifications on the export during the first 30 days have been examined. Because the speed of particles leaving

the mixed layer can have a strong influence on their fate (faster-sinking particles spend less time, and therefore remineralize less, on their way to the ocean interior), the mass flux of particles sinking faster than 100 m d^{-1} out of the mixed layer has been calculated. The results are presented in table 3.

Table 3: Effects of altering model parameters. The change in parameters and the effect this change on model outcome for different diagnostics (export, sinking mass) are shown for the four different scenarios.

	Scenario				
	Standard	Large	Sticky	Colony	Single
Parameter					
Diameter [μm]	20	40	20	20	20
Stickiness	0.1	0.1	0.2	0.1	0
Breakup	1	1	1	0.5	1
Diagnostic					
% Export in 30 days	82	94	91	86	42
Mean sinking mass	4.2	16.5	6.7	9.5	1
% Fast export	11	8	31	49	0

The scenarios that ought to enhance early settlement do enhance it; but the differences among them are small compared to the effect of introducing aggregation at all (see the "Single" scenario). The average mass of particles sedimenting out of the mixed layer is largest for "Large". Note that the comparison is being done in units of the original single cells, not the ($\approx 5\times$ larger) cells of "Large"; the average particle comprises only 3.4 of those cells. The fraction of particles sinking faster than 100 m d^{-1} is especially enhanced in the "Colony" and in the "Sticky" scenario. Thus, increasing either particle stickiness or the ability of aggregates to form colonies not only incerases total export, but also speeds up the mass that sinks out of the mixed layer.

Figure 6 shows the flux through the thermocline of mass that settles faster than 100 m/day. This increases dramatically in the "Sticky" and "Colony" scenarios. The results of "Large" perhaps need explaining. The starting values of PHY and ϵ have been kept the same as for the other runs, which meant that PHYNOS started at $2^{-\zeta} \approx 20\%$ of its value in the other scenarios. So there weren't the numbers of cells to aggregate, and what cells there were were heavier and settling out sooner in any case. Thus this scenario produces an early

settlement of moderately heavy particles and not so many super-heavy ones later.

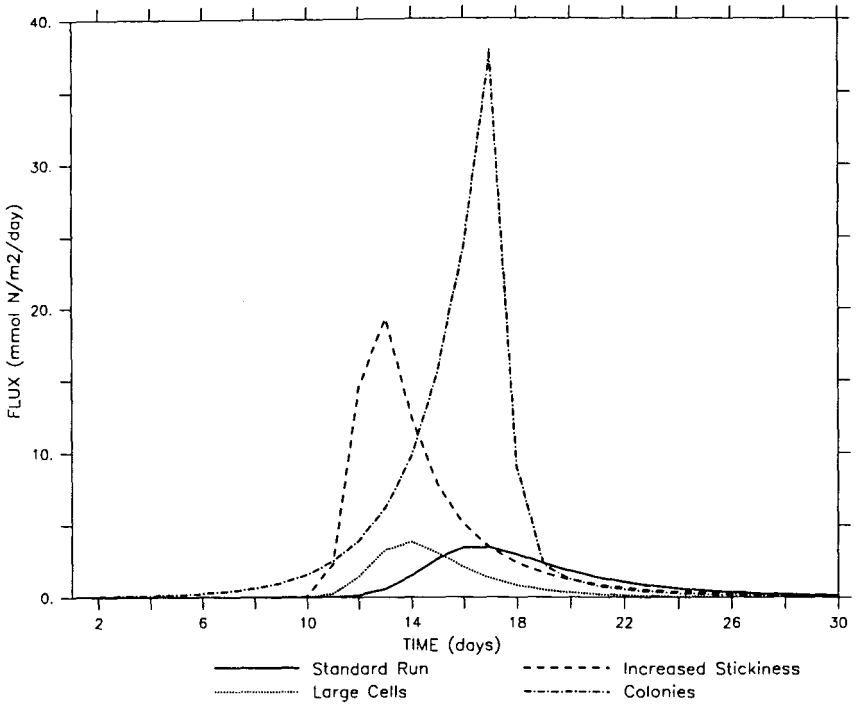

Figure 6: Sedimentation out of the mixed layer for mass of particles sinking faster than 100 m d^{-1}.

The effects of the different processes – aggregation, particle seperation, and number sedimentation – on the average particle size for the four scenarios are shown in figure 7. In the first three scenarios, the sedimentation of large particles counteracts the increase in particle size due to aggregation, while particle seperation has no effect. The change in average particle size is largest for the stickiness experiment. The largest effects are exhibited by the model simulating colony formation. Because this process does not depend on particle number concentration, but is coupled to phytoplankton (mass) growth, growth immediately starts to increase the size of particles, leading to an increase in particle sinking rate.

It is not possible to make close comparisons with the results of corresponding experiments in Riebesell and Wolf-Gladrow (1992) because their standard simulation is quite different. They have a seperation probability of 0 for all aggregates larger than 1 cell, and therefore more growth of aggregates due to colony formation; this makes it harder to see the effects of aggregation in their model. As one might expect, the mean size of sinking particles is much larger in Riebesell and Wolf-Gladrow (1992) (their figure 6) than in the model presented here. Still the qualitative nature of the experiments agrees with their results.

Highest export rates of fast-settling material might be given by sticky, large, chain-forming

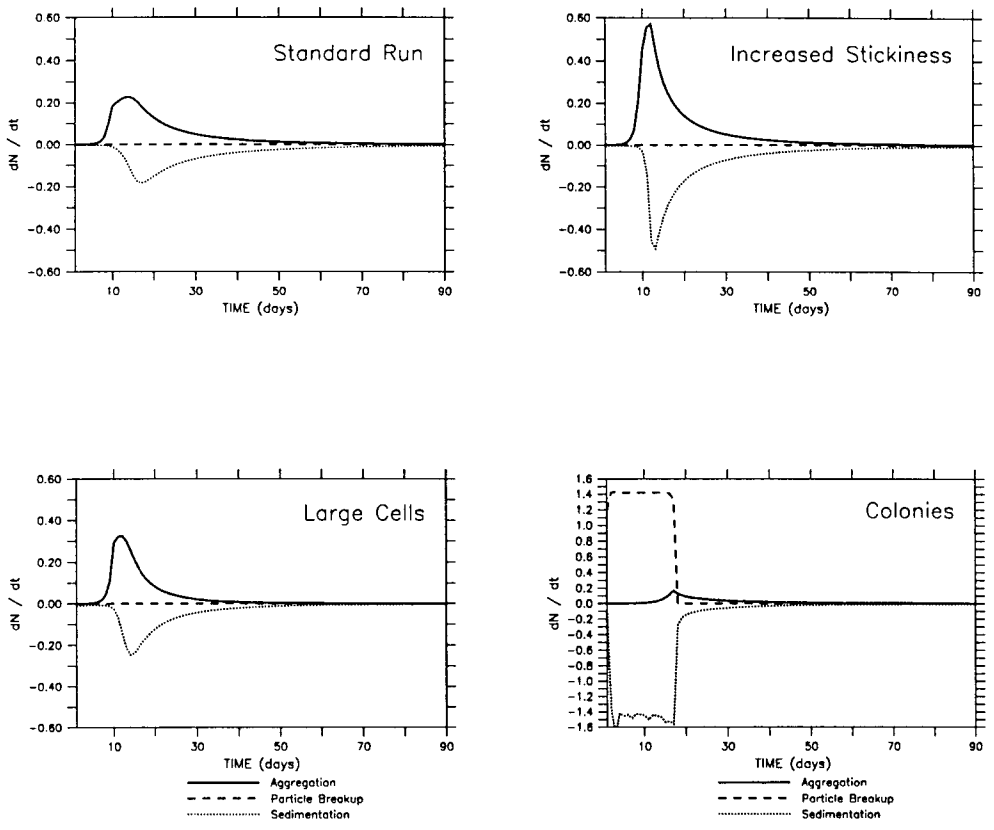

Figure 7: Effects of aggregation, sedimentation and particle breakup on average particle size for standard run and three experiments. The y-axis represents the derivative dN/dt, i.e. the relative contribution of each process to change in average particle size.

cells. *Chaetoceros*, a typical species found in spring blooms in temperate areas, commonly has the appropriate properties. The importance of biological processes such as chain formation and cell size, as exhibited by the model, agrees well with the results of Riebesell and Wolf-Gladrow (1992). Aggregation, especially when combined with higher stickiness or chain-forming species, enhances export on time scales of 30 days up to 100 %, compared to to a model with non-aggregating, slow-sinking species. Simulating chain-forming or sticky species also increases the number of very large particles leaving the mixed layer. Larger aggregates have less time to remineralize in the mid-ocean, leading to an increased export of phytoplankton carbon to deeper layers. The results presented in this chapter stress the importance of phytoplankton biological characteristics such as cell size, colony formation and stickiness on their post-bloom fate. In this model the production of large, fast-settling aggregates, which are not ingested by zooplankton may lead to a sudden flux of particulate matter to the ocean interior after a spring bloom.

As a mixed layer model this model does not account for the fate of phytoplankton once

it has settled out of the mixed layer. To evaluate the importance of rapid aggregation for sedimentation and transport to the ocean interior accurately, a vertically resolved model which includes aggregation and biological processes down to greater depths is needed. This model will be presented in the next chapter.

4 The 1-dimensional model

The previous chapter showed that aggregation and colony formation is important for the quantity and quality of particulate organic matter settling out of the mixed layer. It has become clear that aggregation may greatly enhance the flux of fast settling particles towards greater depth - but as a box model for the mixed layer of course it failed to determine its quantity at a greater depth. The vertically resolved model as presented in this chapter has been constructed to evaluate the influence of phytoplankton aggregation for flux through the maximum depth of the seasonal thermocline and a deep layer. This chapter is specifically determined to check the outcome of a vertically resolved model of phytoplankton aggregation against the results of the 0-dimensional model presented in chapter 3, and also serves for comparing the results with the results for flux through a permanent pycnocline as in Riebesell and Wolf-Gladrow (1992). For this purpose the equations for three compartments NO3, PHY and PHYNOS have been implemented into a 1-dimensional, vertically resolved model, where the mixed layer depth is held constant at 25 m for a period of 90 days. The following chapters will then consider more elaborate formulations for ocean biogeochemical processes such as a varying mixed layer and light, zooplankton feeding and fecal pellet sedimentation.

4.1 Model Structure

The aggregation equations as given by Jackson (1990), and introduced in chapter 2 have been solved and implemented into a 1-dimensional model for a water column of 400 m depth. The grid of Haupt (1995) is used to give extra resolution near the surface where light gradients are strongest: the layer thickness ($dz(iz)$) for a given layer iz increases exponentially with depth:

$$dz(iz) = e^{\frac{iz}{12}}\, dz(1) \qquad \text{with} \qquad dz(1) = 1\ \text{m} \qquad \text{and} \qquad iz = 2, 42 \tag{24}$$

The total depth of the vertically resolved water column is about 401 m. The first 21 boxes are situated in the upper 60 m, where the depth resolution ranges from 1 m for the uppermost box to 5.75 m. The deepest box has a thickness of 33 m. Diffusive exchange between the different layers, with the tracer being defined in the center of every grid box, is calculated using a constant mixed layer depth of 25 m. Above the thermocline, the

turbulent eddy diffusion coefficient is set to $K_{up} = 200$ cm^2 s^{-1}. Below the thermocline, turbulent diffusive mixing is set to $K_{low} = 0.125$ cm^2 s^{-1}. So in addition to the sinks and sources for every compartment, at every depth this model computes loss or gain due to diffusive exchange with its neighbours, following the equation

$$\frac{\delta X}{\delta t} = \frac{\delta}{\delta z} K(z) \frac{\delta X}{\delta z} \quad \text{with} \quad K(z) = \begin{cases} K_{up} & : \; z < thermocline \\ K_{low} & : \; z \geq thermocline \end{cases} \tag{25}$$

No lateral exchange is taken into account, i.e. it is assumed that the water column is not affected by horizontal processes. Having very different time scales for the dependent variables to compute, all model equations are solved using a variable coefficient ordinary differential equation solver (SVODE; Brown *et al.*, 1989) with an implicit method for integration over time.

4.1.1 Mass balances

Phytoplankton growth is limited by the product of nutrient and light terms. Nutrient limitation is a Monod function of nitrate concentration. Light limitation $J(z,t)$ for every grid box iz with lower depth $z(iz)$ is averaged over box thickness $dz(iz)$ and integrated over one day as in Evans and Parsltow (1985), using the rational function approximation of Evans and Garçon (1997). In contrast to the 0-dimensional model, this model explicitely considers phytoplankton self shading (see Evans and Parslow, 1985). Light for a given depth z is calculated by

$$I(z) = I_0 e^{\int_0^z (k_w + k_c \mathrm{PHY}) dz} \tag{26}$$

where k_w and k_c are the attenuation coefficients for water and phytoplankton, respectively. The attenuation coefficient of phytoplankton is independent of its aggregation state. In addition to the phytoplankton mass loss due to sedimentation, another linear term for phytoplankton mortality (λ_{PHY}) has been introduced into this model. This linear term changes both phytoplankton mass and numbers equally, so it has no effect on the particle size distribution. Phytoplankton is assumed to be degraded to nitrate immediately after phytoplankton death, except for one (the detrital) scenario, where it is assumed not to dissolve, but is shifted into the detrital pool. The equation for nitrate (NO3) and phytoplankton mass (PHY) then read:

$$\frac{\mathrm{dNO3}}{\mathrm{d}t} = -\frac{\mathrm{NO3}}{k_{\mathrm{NO3}} + \mathrm{NO3}} J(z,t)\,\mathrm{PHY} + \lambda\,\mathrm{PHY} \tag{27}$$

$$\frac{\mathrm{dPHY}}{\mathrm{d}t} = \frac{\mathrm{NO3}}{k_{\mathrm{NO3}} + \mathrm{NO3}} J(z,t)\,\mathrm{PHY} - \lambda\,\mathrm{PHY} - \Psi \tag{28}$$

4.1.2 Implementation of sedimentation and aggregation

One advantage of the model presented in the previous chapter is that it describes the particle size distribution by a two-parameter function over a size range from some lower boundary m to ∞, and the processes that depend on particle size by simple equations without the necessity of evaluating thousands of equations during run time. Yet for the equations for aggregation and sedimentation of numbers and mass to be solved in advance (prior to the model simulation) some preconditions have to be met:

1. The integral that gives the number of collisions ξ as presented in equation 22 can only be solved if $min(\epsilon - 3, \epsilon - \eta - 2) > 1$.

2. The integral that gives the mass of particles that sink out of the model domain (equation 19 in the previous chapter) can only be solved if $\epsilon - \eta - \zeta > 1$.

If the first condition is not met, the integral diverges over the integration domain, and there would be an infinite number of collisions between all particles. Of course, this cannot be. If the second condition is not met, the mass flux integral diverges.

It has been shown that in the 0-dimensional model sinking especially removes large particles from the mixed layer: Particles sinking out of the mixed layer (ML) have a size distribution $\epsilon_{sink} = \epsilon_{ML} - \eta$, so the large particles in the mixed layer of the box model are automatically removed by sedimentation and moved to the submixed layer. Thus if there are no divergent integrals to begin with, none will develop.

In a 1-dimensional model, the large particles which sunk out of the i-th layer reach the i+1 layer with a distribution $\epsilon_{i+1} = \epsilon_i - \eta = \epsilon_{i-1} - 2\,\eta = ...$ The large particles sinking out of one layer are added to the particles in the next deeper layer, flatten its size distribution, and decrease its distribution coefficient ϵ. Especially in the deeper layers, ϵ may become smaller than $1 + \zeta + \eta$, so some restrictions have been made for the evaluation of the number of collisions: Think of some upper size limit M, beyond which the sinking rate does not

increase as a function of diameter, but is constant at $w_M = \zeta M^\eta$. Further, assume that aggregation of particles larger than this size M does not depend on particle size anymore, but the probability of collisions is constant for any particle larger than this size. In this case, all of the integrals that have to be evaluated have an upper boundary and can be solved without any restrictions.

Sinking of phytoplankton cells Assume a sinking exponent η and a size M beyond which η has no further effect: sinking speed thereafter is constant. Then $w = B\theta^\eta$ is the sinking speed of a particle of size θ, with $m < \theta < M$, and $w_M = BM^\eta$ is the constant sinking speed of particles larger than M. Number and mass sedimentation (Φ and Ψ) at any depth z can then be evaluated according to

$$\Phi(z) = \frac{1}{dz}\left[\int_m^M p(z,\theta)\, w(z,\theta)\mathrm{d}\theta + \int_M^\infty p(z,\theta) w_M \mathrm{d}\theta\right] \tag{29}$$

$$\Psi(z) = \frac{C}{dz}\left[\int_m^M p(z,\theta)\theta^\zeta w(z,\theta)\mathrm{d}\theta + \int_M^\infty p(z,\theta)\theta^\zeta w_M \mathrm{d}\theta\right] \tag{30}$$

where $p(z,\theta)$ is the number distribution of phytoplankton in a depth z as given by equation 12, and the mass of an aggregate of size θ is given by $C\ \theta^\zeta$. The coefficient A and the exponent ϵ for every depth are calculated from the mass and number concentration of the corresponding layer (see equation 16). Having a size distribution exponent varying with depth, average mass and number sinking speed can be computed, using the equation 21.

Aggregation of phytoplankton cells As described in chapter 3, the probability of collision of particles is a function of particle size, concentration, the rate of turbulent shear and the difference of the settling velocities of two different particles. The equations for collisions due to shear and differential settlement as presented by Jackson (1990) have been added together, converted to a size-continuous form, and multiplied by stickiness. To bound the aggregation equations from getting out of the range of convergence, the upper limit M that is used for the sedimentation equations has also been used for the computation of the number of collisions. Assume that the probability to collide of particles dlarger than the same size M no longer varies with increasing particle size. Then for the evaluation of collisions due to shear and settlement, there are four double integrals ($I_1 - I_4$) to be solved.

Because the integration kernels are symetric with respect to the line $\Theta = \theta$ (see chapter 2), $I_2 = I_3$. The domain of particles sizes over which the aggregation equations have to be solved are sketched in diagram 8 and the solutions can be found in appendix A.3. Their sum times the number of stickiness then gives the number of collisions resulting in new aggregates.

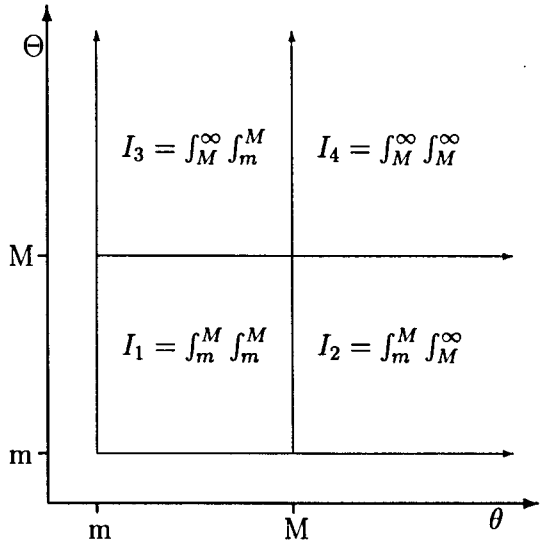

Figure 8: Sketch showing the domain of integration for the aggregation equations in the 1-dimensional model. The x- and y-axis denote particle diameter. The four integration domains are denoted by I_1, I_2, I_3 and I_4 (see appendix A.3).

4.1.3 Colony formation and aggregate fragmentation

Primary production does not necessarily increase the number of aggregates: dividing cells may remain together. The rate of production of aggregates is a fraction $0 < b < 1$ of the rate of production of mass: the fraction of newly divided cells that break apart after cell division. If the seperation probability is set to one, phytoplankton growth has no effect on the size distribution of phytoplankton, otherwise it increases the average aggregate mass by adding mass at a higher proportion than the numebr of particles that is being added.
In a vertically resolved model there has to be a way aggregates disappear due to microbial breakdown especially at greater depths. This may happen by a variety of processes: Aggregates may breakup into smaller ones, without losing overall particulate mass, or they may become eroded at their outer edges, or even degrade to some dissolved constituent. Whereas the former processes would only affect the number of aggregates, but not their

mass, the latter affects only their mass, but not their number. All processes decrease the average size of particles, i.e. they increase the slope of the size distribution, ϵ. Little is known about the processes of erosion and degradation to dissolved organic or inorganic matter. Floc breakup mainly happens due to turbulent shear (Ruiz and Izquierdo, 1997; Riebesell, 1991), or when the cells become senescent (Smayda and Boleyn, 1965). The stability of the connection between the individual cells may vary with the material that interlocks the cells: e.g. *Thalassiosira* cells are joined into colonies by a gelatinous strand which may break apart more easily than the cells of the setose forms of *Chaetoceros.*

For the sake of simplicity, neither of these processes is built into the current model, but as explained above particle degradation is assumed not to have any effect on the size distribution. This is done by reducing the mass and number by the same fraction λ_{phy}.

The equation for phytoplankton numbers then reads

$$\frac{\mathrm{dPHYNOS}}{\mathrm{d}t} = b\frac{\mathrm{NO3}}{k_{\mathrm{NO3}} + \mathrm{NO3}} J(z,t)\,\mathrm{PHYNOS} - \lambda\,\mathrm{PHYNOS} - \Phi(z) - \xi(z) \tag{31}$$

4.2 Model Setup

Most of the parameters that have been assigned in the box model simulation in the previous chapter are also used in the vertically resolved model, except for phytoplankton maximum growth rate μ_{PHY}, which has been set to a rather high value of 2.5 d^{-1}. The parameters for the influence of light on phytoplankton growth have been chosen mainly in accordance with Fasham *et al.* (1990; see table 4). Using these parameters and surface solar radiation as appropriate for e.g. 10°N on January 1 ($\approx$ 141 W m^{-2}) the accomplished phytoplankton growth rate in the first layer is always around 1 d^{-1}, i.e. about the same as in the grid model simulation. In deeper layers, of course phytoplankton growth is reduced due to lower light. Again, the half-saturation constant k_{NO3} for nitrate uptake by phytoplankton has been set to such a low value that almost all of the nitrate in the upper layers will be used by phytoplankton. As turbulent kinetic energy below the mixed layer is usually low, shear below the mixed layer has been set to zero, i.e. below the mixed layer aggregation only takes part due to differential settlement. The upper boundary for the evaluation of the sinking and aggregation equations in all following simulations has been set to a rather high value of 2 cm. This is about the maximum size, for which investigations related to the diameter – sinking relationship exist (Alldredge and Gotschalk, 1988).

Table 4: Parameters for biological and aggregation module for simulations with the grid model and constant physical forcing. When two values are given, the second is the value assigned in one of the changed scenarios.

Parameter	Symbol	Value	Unit
phytoplankton parameters			
maximum growth rate	μ_{PHY}	2.5	d^{-1}
half-sat. const. for NO3 uptake	k_{NO3}	0.05	mmol N m^{-3}
PHY-specific attenuation coefficient	k_c	0.03	mmol N^{-1} m^2
water attenuation coefficient	k_w	0.04	m^{-1}
initial slope of P-I curve	α	0.025	(d W m^{-2})$^{-1}$
mortality	λ_{PHY}	0.00/0.04	d^{-1}
aggregation parameters			
shear rate	*shear*	0.84	s^{-1}
sinking exponent	η	1.17	-
sinking factor	B	1.10	$\mathrm{cm}^{-0.17}$ sec^{-1}
stickiness	*stick*	0.1/0.2	-
breakup probability	b	1/0.5	-
cell size	m	0.002/0.004	cm
N content exponent	ζ	2.28	-
N content coefficient	C	5.67	nmol N $\mathrm{cm}^{-2.28}$

4.3 Results

4.3.1 The Base Run

This model gives not only the concentrations of the prognostic variables NO3 and PHY, but also, as it computes the number of phytoplankton aggregates separatly, the average size of particles and the resulting mass sinking speed. Figure 9 shows phytoplankton mass and sinking speed for the simulation of the 1-D model (hereafter called the "grid" model) over a time period of 90 days with a constant physical forcing. Starting from low phytoplankton concentrations (0.001 mmol N m^{-3}), a steep size distribution ($\epsilon = 8$) and a high nitrate concentration of 10 mmol N m^{-3}, phytoplankton increases until it reaches its maximum value of about 9.5 mmol N m^{-3}. Phytoplankton is distributed homogeneously throughout the mixed layer, and decreases below due to shading. Immediately after the surface bloom, sinking speed increases dramatically especially in deeper layers, until it reaches its maximum

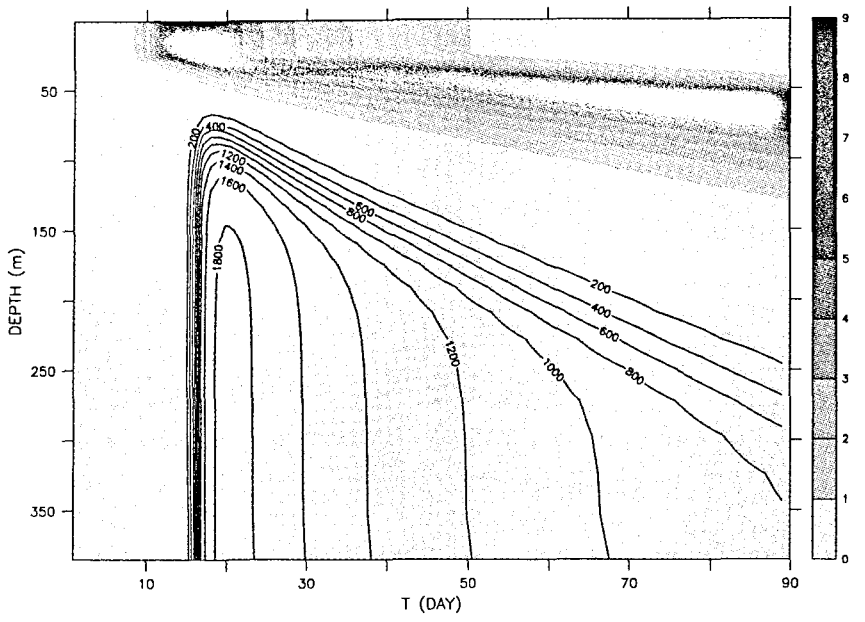

Figure 9: Phytoplankton and sinking speed in the grid model with constant physical forcing. Phytoplankton is filled with grey shade (see contour key on the right side), units are mmol N m^{-3}. Sinking speed (m d^{-1}) is contoured by a thin line.

value of 1856 m d^{-1} (which is close to the maximum sinking speed of $\approx$ 2100 m d^{-1} that can be achived in this model) on day 20 in 400 m depth. The increase in sinking speed is a direct effect of aggregation in the surface layer (shear is set to zero below the mixed layer) and the preferential sedimentation of large, fast settling aggregates (see chapter 3 for explanation). Following day 20, the large aggregates have settled out of the mixed layer and there isit no longer sufficient particle concentrations in the euphotic zone to fuel aggregation anymore and large particle flux to deeper layers, so the particle size and with it the sinking speed decrease again to values less than 1000 m d^{-1}. Surface nitrate at this time has decreased to less than 1 mmol N m^{-3}, but nitrate remains at its initial values of 10 mmol N m^{-3} in deep layers (no figure). Phytoplankton mixed layer concentration has decreased to less than 1 mmol N m^{-3} on day 50. Following the mixed layer bloom, a deep chlorophyll maximum (DCM) is established at a depth where nitrate is still high, and light is still sufficient to promote positive net phytoplankton growth.

Figure 10 shows the logarithm of the rate of aggregation (rate of collisions times stickiness) for collisions due to shear in the mixed layer (upper panel of figure 10) and the vertically resolved plot of collisions due to differential settlement. This plot shows, that collisions due to shear in the mixed layer occur at a much higher rate than collisions due to differential settlement. This fact can be explained by the structure of the kernels of the corresponding

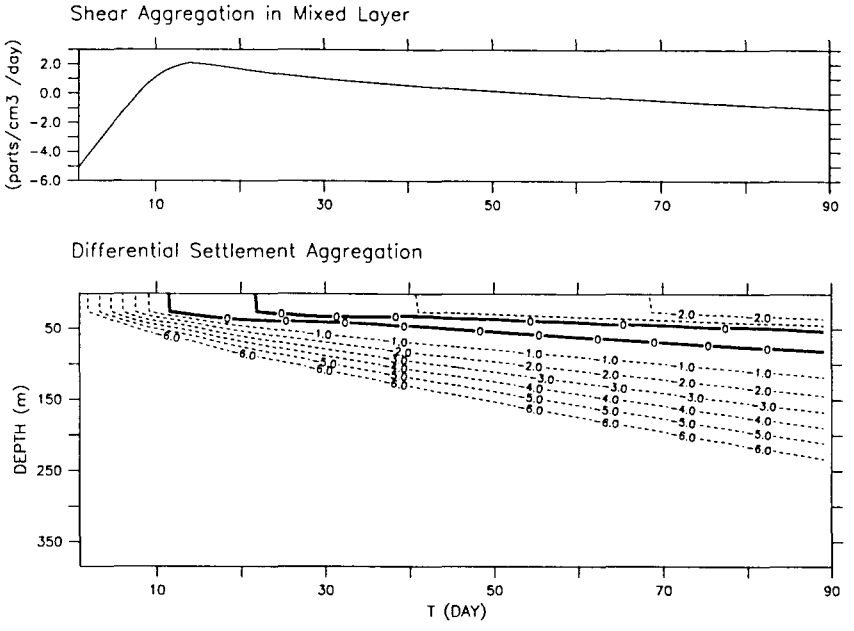

Figure 10: Aggregation (defined as number of collisions times particle stickiness) for collisions due to shear and differential settlement for the base model simulation. The logarithm of particles aggregating due to shear is shown for the mixed layer only in the upper panel over time. The logarithm of aggregation due to differential settlement is shown over time and depth, with contour lines giving the logarithm of particles per cm^3 and second.

equations, which have been discussed in more detail in chapter 2. Because the rate of turbulent shear for layers below the mixed layer in this model has been set to zero, of course there are no collisions due to shear in these depths, and differential settlement is the only mechanism that produces large aggregates. Because aggregation in the submixed layer is low due to missing turbulent shear and low rates of differential settlement aggregation, and the DCM is situated below the mixed layer, it only slowly settles down to deeper layers during the course of the simulation. Primary production in the mixed layer is 317 mmol N m^{-2} – the model has been constructed so that all of the nitrate in the mixed layer (250 mmol N m^{-3}) plus some additional input by diffusion across the base of the mixed layer will be used for production. The model further accounts for production below the mixed layer, which in this case with 300 mmol N m^{-2} is almost as much as mixed layer production. 313 mmol N m^{-2}, i.e. almost all of the mixed layer production settles out during the course of the simulation, with the maximum of nearly 20 mmol N m^{-2} d^{-1} of sedimentation on day 19 (figure 11). Due to the very large sinking rates, most of the bloom phytoplankton once it has settled out of the mixed layer reaches a depth of 400 m within one or two days, leading to a pulse in sedimentation which is more than half of the peak mixed layer

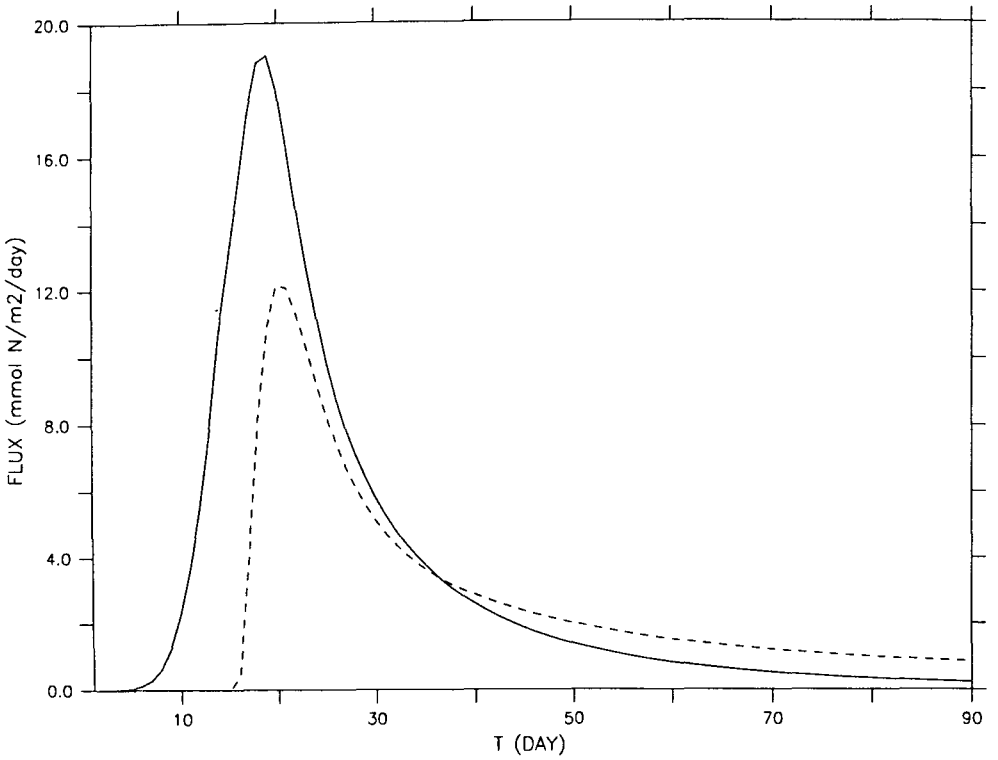

Figure 11: Sedimentation in 25 and 400 m in the grid model with constant physical forcing. Units are mmol N m^{-2} d^{-1}.

sedimentation. There is only little contribution of the deep chlorophyll maximum to particle flux. Aggregation and its impact on particle flux thus plays its major role during the massive bloom event in the mixed layer, but not during the relatively slow development of the DCM. Nevertheless, particle flux over the whole simulation period in 400 m is still large, with an integrated flux of 227 mmol N m^{-2}, which is 73% of mixed layer sedimentation and 37% of water column primary production.

4.3.2 Experiments

The main task of this chapter is to compare the model with the zero dimensional model: not only the standard run, but also the sensitivity of the model to alterations in its parameters. For this purpose, the same experiments – doubling stickiness and cell size, reducing separation probability by 50% and omitting aggregation and size dependent sinking – have been performed with the grid model and the results have been compared with the box model results. Figure 12 shows that there is little difference in outcome of the simulations performed with the grid model for phytoplankton, averaged over the upper 25 m and the results of the box model for most of the experiments. Peak concentrations in the grid

model type are slightly lower, which can be attributed to the self shading of phytoplankton incorporated in this model. Also the decline of phytoplankton in all the simulations is slower, which can be attributed to diffusive processes within and across the mixed layer, when parts of the DCM are mixed into the surface layers.

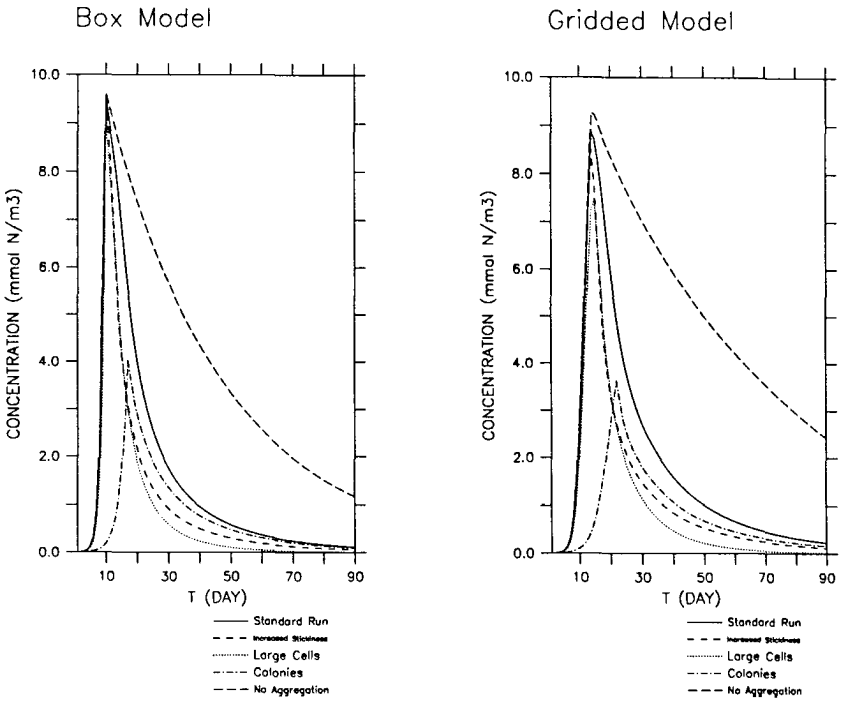

Figure 12: Mixed layer phytoplankton in the box model (chapter 3) and in the grid model (averaged over the upper 25 m) for the five different experiments.

The largest effect can be found in the simulation concerning large cells. Here peak phytoplankton concentration is about 1 mmol N m^{-3} lower in the grid model than in the box model. Also, when simulating colony formation there is a little delay in the timing of the peak bloom. Still the overall pattern of model behaviour and the effects of the different alterations are quite similar in both model types.

There is also little difference in the development of average mass sinking speed between both model types (figure 13). The largest effect of model type again can be found for scenario "Colony", where maximum sinking speed is lower in the grid model than in the box model. This is a result of the reduced growth rate due to light limitation in the grid model. Another effect of the reduction in growth and sinking speed in the grid model then is of course a reduction in peak sedimentation out of the mixed layer, especiall for the "Colony" scenario, from almost 48 mmol N m^{-2} d^{-1} in the box model to less than 35 mmol N m^{-2} d^{-1} in the grid model (figure 14). Nevertheless, these effects are small when

compared to the effects of the alterations in parameters or introducing aggregation at all.

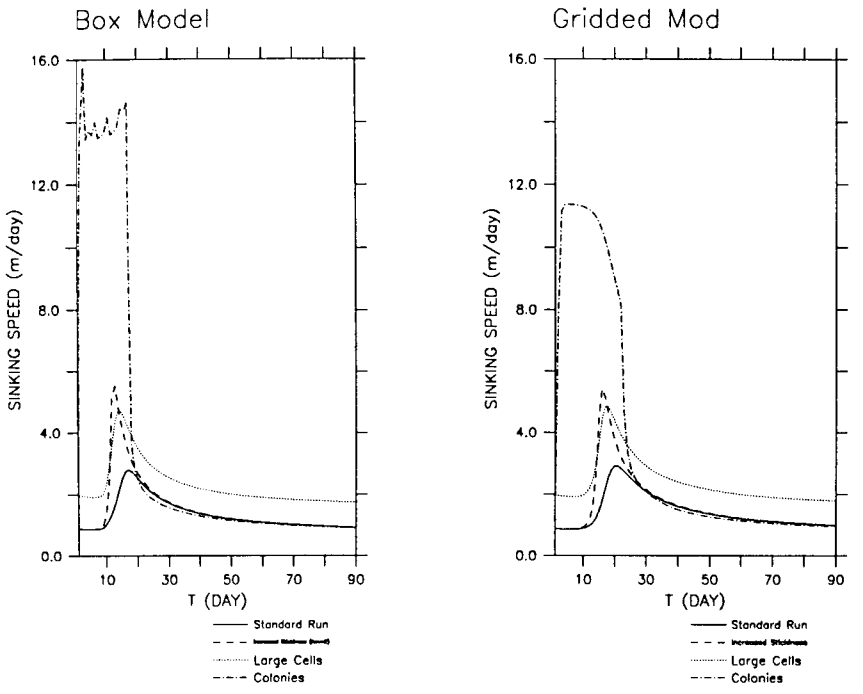

Figure 13: Mixed layer mass sinking speed in the box model (chapter 3) and in the grid model (averaged over the upper 25 m) for the five different experiments.

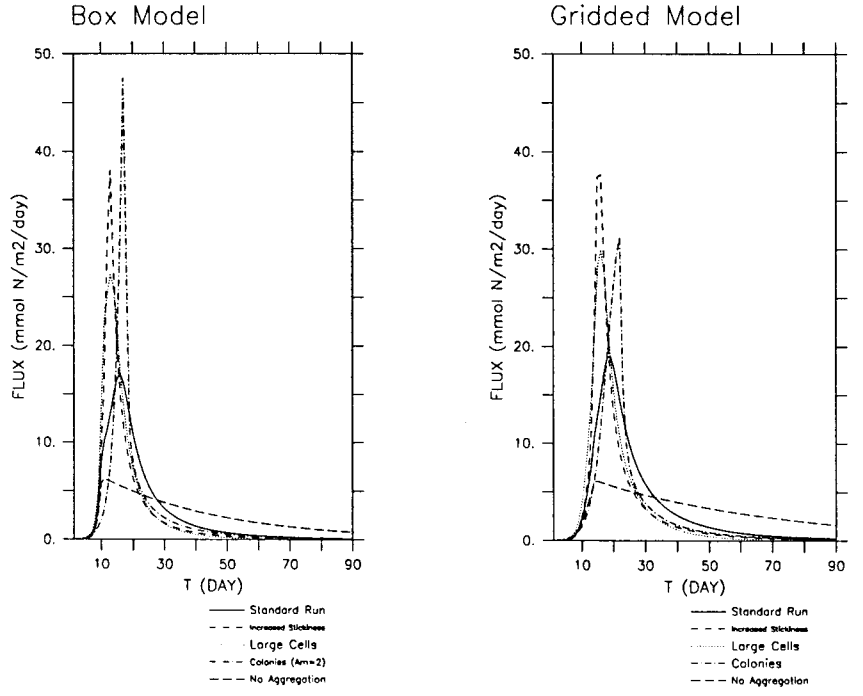

Figure 14: Sedimentation in 25 m in the box model (chapter 3) and in the grid model, for five different experiments.

The advantage of this model is that it provides the possibility to evaluate export to deeper layers than the depth of the mixed layer. Figure 15 shows the flux at 400 m for all five scenarios. The flux is greatly enhanced for all scenarios which include aggregation at all

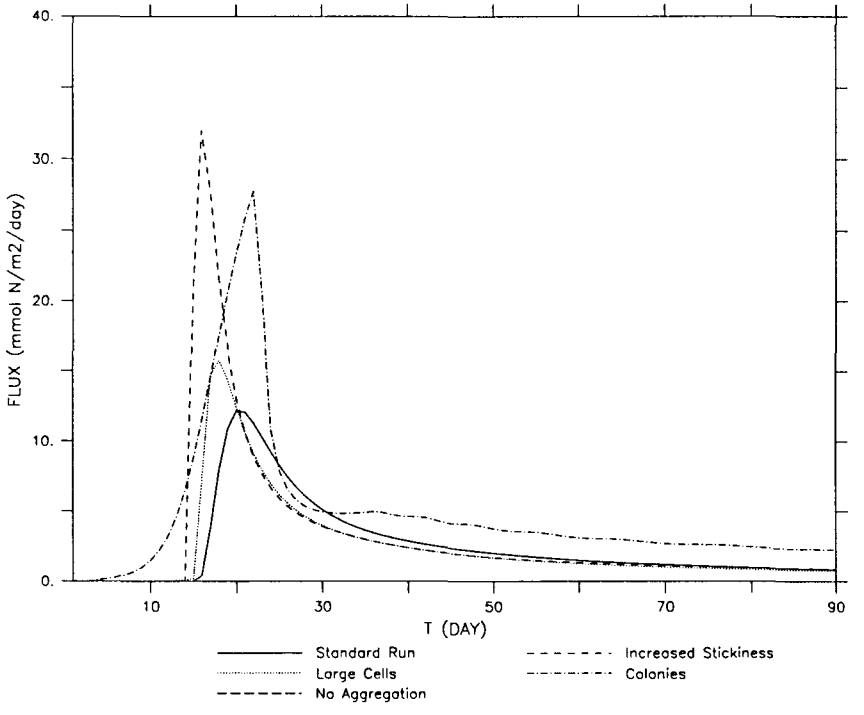

Figure 15: Sedimentation in 400 m in the grid model, for five different experiments.

when compared to the scenario with non-aggregating phytoplankton cells – the enhancement is largest for the "Sticky" scenario with a peak sedimentation more than 30 mmol N m^{-2} d^{-1} and lowest for the "Large" scenario, which is only about 2 mmol N m^{-2} d^{-1} more at its maximum than the base run. There is of course no flux from the scenario without aggregation, but with a constant sinking speed, where phytoplankton sinks at the speed of one single cell (< 0.7 m d^{-1}). It would take over 500 days for the mass to sink out of the water column of 400 m depth - a time period that greatly exceeds the simulation time. The differences in temporal pattern of sedimentation through 400 m in the scenarios are not as pronounced as Riebsell and Wolf-Gladrow (1992) have found with their size-discrete representation (their figure 5). This may be explained by the large upper boundary used in the model presented here: Riebesell and Wolf-Gladrow have a maximum particle size of 1000 cells per aggregate, which corresponds to an aggregate diameter of about 417 μm, or a maximum sinking speed of about 23 m d^{-1}. The model presented here computes much higher sinking speeds due to the upper boundary for size dependent sedimentation

(M = 2 cm), and thus aggregation alone has already a large impact on deep flux, but alterations in its parameters are of little importance compared to introducing aggregation at all. Nevertheless, the increase of deep flux integrated over the simulation of 90 days, as well as the fraction of deep flux to mixed layer flux in this model is largest for the "Sticky" and "Colony" scenario, a result that agrees well with the results presented in Riebesell and Wolf-Gladrow (1992).

The scenarios presented so far also allow for aggregation and growth below the mixed layer, which may additionally increase the deep flux, but lack the process of degradation of aggregates while they settle downwards. To account for this process, a experiment has been performed, in which phytoplankton mortality has been set to 0.04 day-1, the same value as Riebesell and Wolf-Gladrow used for their experiments for submixed layer degradation of phytoplankton aggregates. The degraded phytoplankton goes back to the NO3 pool, and may again be taken up by phytoplankton. In this model, total integrated production with 983 mmol N m^{-2} is greatly enhanced, because a nitrogen molecule may cycle several times through phytoplankton and dissolved inorganic nitrogen before it finally sinks out of the model domain. The recycling of nutrients in this model takes place in the mixed layer as well as in deeper layers, so the additional production also takes place in the upper (0-25 m) as well as in deeper layers (see table 5). Phytoplankton sedimentation at 25 m is only slightly enhanced, whereas deep sedimentation is reduced because some aggregates are decomposed before they reach the bottom of the model water column. The results in phytoplankton and mass sinking speed development are shown in figure 16, together with the results from the base run and the experiments. Comparing all of the plots for the base run and the five experiments, introducing aggregation or increasing the ability of phytoplankton to aggregate or to form colonies has an effect on the maximum phytoplankton concentration that can be achieved during the mixed layer bloom. The reduction in maximum phytoplankton concentrations is largest for the "Colony" scenario, where the bloom only reaches a miximum concentration of about 3.5 mmol N m^{-3}. It can also be seen that in this scenario, sinking speed increases much more rapidly (due to the growth dependent increase in aggregate size) than in the other scenarios. When simulating constantly sinking, non-aggregating species, the decline of phytoplankton after the bloom takes much longer than in the aggregation scenarios, leading to increased phytoplankton in the mixed layer. Consequently, phytoplankton growth below is reduced and does not lead to a formation of a deep chlorophyll maximum as pronounced as in the aggregation scenarios.

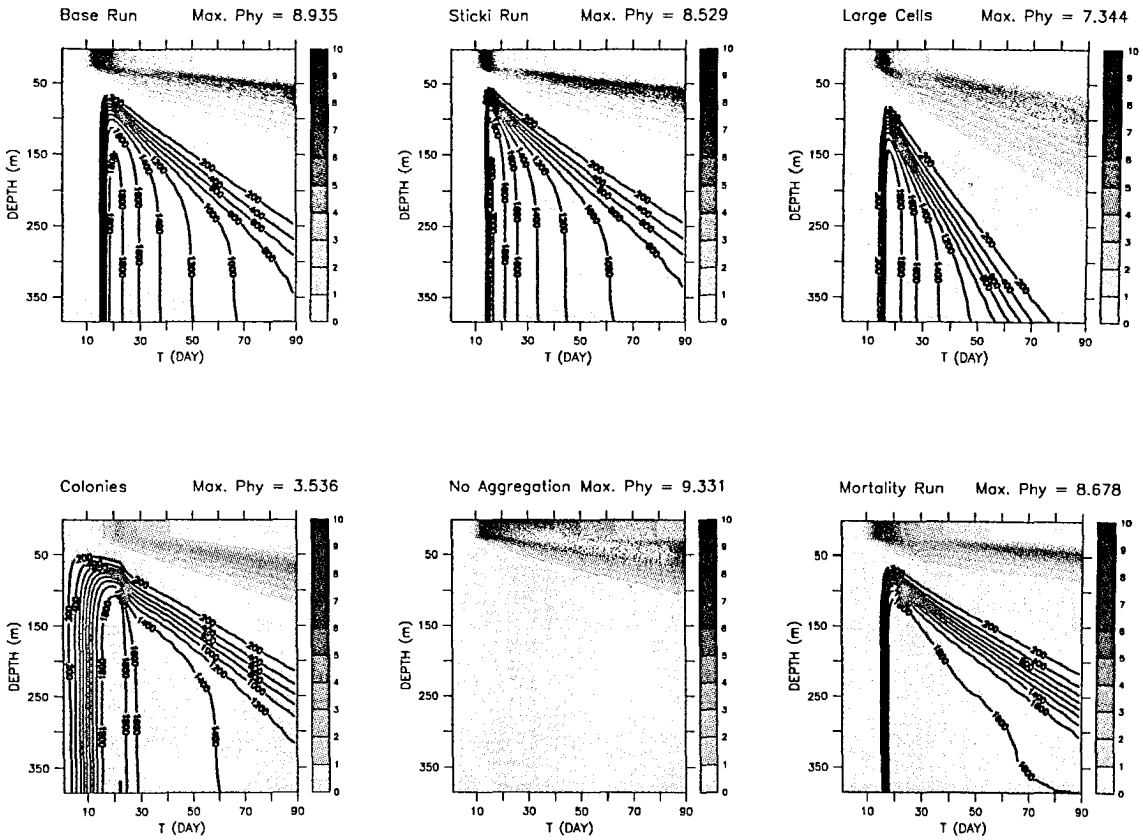

Figure 16: Phytoplankton and sinking speed in the grid model with constant physical forcing for six experiments. Phytoplankton is filled with grey shade (see contour key on the right side), units are mmol N m^{-3}. Sinking speed (m d^{-1}) is contoured by a line.

4.4 Discussion

Table 5 shows primary production and flux at two depths, integrated over the time of simulation for the base scenario and the five experiments. Much of the primary production in this model can be attributed to depths > 25 m. This Deep Chorophyll Maximum (DCM) could theoretically be seen as another source of settling material beside the rapid sedimentation event immediately after the spring bloom. Nevertheless, almost all of the primary production that is produced in the upper 25 m finally settles out of this region - but even though primary production in the deeper layers is of the same order of magnitude as the mixed layer production, deep flux is less (except for the "Colony" scenario) than shallow flux. The reason for this can mainly be seen in the different environments the mixed layer bloom and the DCM phytoplankton population are exposed to: Shear in the mixed layer in this model is high, so aggregation rates are high and together with the high density of

phytoplankton the mixed layer bloom quickly undergoes a rapid change in size distribution and experiences accelerated sinking speeds. This can be seen from the dramatic increase in sinking speed shortly after the bloom event. On the other hand, phytoplankton in the DCM only aggregates due to differential settlement, i.e. at lower rates, and additionally it never reaches as high concentrations as the spring bloom. Thus, there is little change in size and sinking speed, and the DCM persists for a longer time, and contributes little to deep flux (and, of course, not to shallow flux). Summarizing, the DCM cannot be seen as a source of sedimentation at least on a time scale of 90 days. So even when simulating aggregation in a biogeochemical model, if the physical environment as given by mixed layer depth shows little variation, but persists at shallow depths allowing phytoplankton to form a DCM, it is unlikely that there will be a large flux of material out of the upper layers. This behaviour of the model changes if colony formation is simulated by setting the breakup probability to values < 1. Now phytoplankton aggregates may increase their size and settling speed without the need of high aggregation. In this case, the DCM contributes largely to deep flux, which in this scenario is even larger than shallow flux.

Table 5: Depth integrated primary production (PP) and flux through 25 and 400 m for model experiments with the grid model. All units are mmol N m^{-2}.

Scenario	PP ($\int$ 25m)	PP ($\int$ 400m)	Flux (25m)	Flux (400m)
Base	317	617	313	227
Sticky	309	660	307	289
Large Cells	292	776	305	220
Colonies	289	682	292	440
No Aggregation	340	426	280	0
PHY mortality $\lambda_{PHY} = 0.04$	516	983	326	181

Introducing aggregation or increasing one of the parameters which enhance aggregation or colony formation reduces production in the mixed layer, but increases total integrated production. The reason for this can be found in the combined effects of aggregation and phytoplankton self-shading: when mixed layer concentrations are reduced due to the effects of aggregation or colony formation, phytoplankton in the sub-mixed layer have more light and thus a higher effective growth rate. Thus aggregation, although it reduces the maximum peak concentrations that can be achieved during a bloom, enhances integrated primary production. Because the DCM has been shown to have little or no effect on deep flux, the

increased flux in the aggregation scenarios has to be attributed to its changes in parameter values and aggregation and settling characteristics, but mostly not to the total increase in production. The simulation of phytoplankton mortality increases production, because a nitrogen molecule may cycle many times before it sinks out of the model domain. The vertical diffusion of deep nitrate across the base of the mixed layer additionally is a source for mixed layer production. This is why the total amount of sedimentation out of the mixed layer in this scenario is even higher than that of the experiments with no phytoplankton mortality. Nevertheless, slower sinking particles will be degraded before they reach the bottom of the model. If the time rate of change of particles within the model domain is given by $w(\theta)/400m$, then all the particles that sink with a sinking speed less than ($0.04\mathrm{d}^{-1} \times 400\mathrm{m} = 16\ \mathrm{m\ d}^{-1}$) will be dissolved before they can account for sedimentation. Summarizing, while the rate of aggregation as given by the parameters stickiness or cell size govern the timing and pattern of the sedimentation signal, the rate of remineralization (together with the sinking speed of the particles) determines how much of the mass finally sinks to greater depths.

5 Simulations for the Northeastern North Atlantic

The importance of considering aggregation in a biogeochemical model of ocean biogeochemistry has been tested with simulations performed for a location in the Northeastern North Atlantic, at 47°N, 20°W, hereafter called station NABE. At this site during the North Atlantic Bloom Experiment in 1989 extensive investigations of the biogeochemistry were carried out. This site is a typical site for a temperate open ocean environment. The dominant feature of the annual cycle is a spring bloom of phytoplankton (Ducklow and Harris, 1993), which often consists of diatoms that develops on the nutrients which have been entrained during winter deep convection. Zooplankton are important in the time following the phytoplankton spring bloom (Burkill *et al.*, 1993a; Dam *et al.*, 1993; Lenz *et al.*, 1993), which, in case large (meso)zooplankton is present, may contribute significantly to deep flux via the production of large, rapidly settling fecal pellets (Noji, 1989). To account for this pathway of sedimentation, beside the compartments considered in the previous chapters, as additional compartments zooplankton and fecal pellets have been added.

5.1 Model structure

The vertically resolved model as described in the previous chapter has been altered to provide the possibility

- to extract the contribution of phytoplankton sedimentation in comparison to the mass flux due to fecal pellets.
- to investigate the sensitivity of model outcome (annual primary production, grazing and flux through sedimentation) to alterations in its setup.

For this purpose, in addition to the compartments described in chapter 4 the model considers zooplankton and detritus, which, in the base setup, only consists of fecal pellets , which are egested by zooplankton and sink at a constant sinking rate (see figure 17). The model is driven by annual climatology of mixed layer thickness and variation in light. In this and the following chapters, the vertical model resolution has been extended to 800 m depth, using 50 vertical layers as described in the previous section.
The vertically resolved model is driven by daylength and daily integrated solar radiation, which has been computed according to Brock (1981). Light is reduced by cloudiness following Reed (1976), using a constant average cloudiness of 0.875. Diffusive exchange between

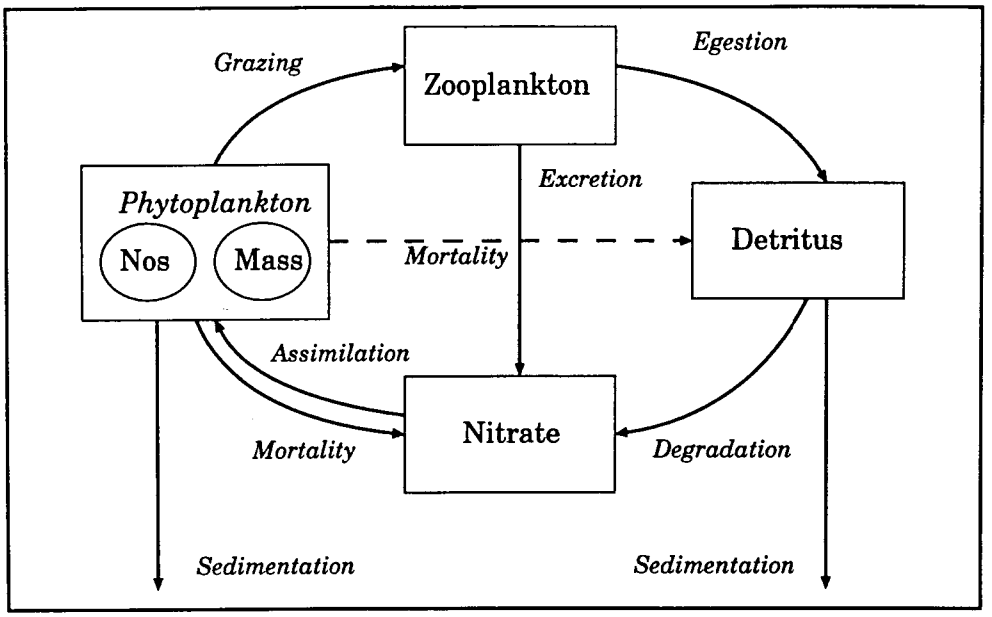

Figure 17: Diagram showing the model structure. The broken line denotes the flux from phytoplankton to detritus in the detrital model. For further explanations see text.

the different layers is calculated using profiles for upper and lower boundary of the thermocline. The depth of the model mixed layer has been set to a typical cycle for this site (as in Levitus 1982), with a deep mixed layer of about 400 m during winter and a shallow mixed layer of 20 - 30 m during summer. The shallowing of the mixed layer in spring in this setup is more rapid than evaluated from the mixed layer climatology, to account for the rapid decline in mixed layer depth that has been found during the NABE process study (Chipman *et al.*, 1993). The lower thermocline in this model has been evaluated by adding 30 m to the depth of the upper thermocline (see figure 18). Above the upper thermocline, the turbulent vertical eddy diffusion coefficient is set to a value of $k_{up} = 1000$ cm^2 s^{-1}. Below the lower thermocline, turbulent diffusive mixing is set to a value of $k_{low} = 1$ cm^2 s^{-1}, which is about three times higher than the value given in Evans and Garçon (1997). Between both boundaries, the diffusion coefficient is interpolated using the cubic approximation presented Evans and Garçon (1997). To allow for shear collisions below the mixed layer, the rate of turbulent shear below the mixed layer in this model as been set to 1/100 of the mixed layer rate of turbulent shear (0.84 s^{1-}).

5.1.1 Mass balances

Phytoplankton takes up nutrients according to the equations described in the previous chapter. Phytoplankton mortality (λ_{PHY}) is a linear function of phytoplankton mass.

$$\frac{\mathrm{d\,NO3}}{\mathrm{d}\,t} = -\frac{\mathrm{NO3}}{k_{\mathrm{NO3}} + \mathrm{NO3}}\, J(z,t)\,\mathrm{PHY} + (\lambda_{\mathrm{ZOO}} + \kappa_{\mathrm{ZOO}}\,\mathrm{ZOO})\,\mathrm{ZOO} + \lambda_{\mathrm{PHY}}\,\mathrm{PHY} + \lambda_{\mathrm{DET}}\,\mathrm{DET} \tag{32}$$

$$\frac{\mathrm{d\,PHY}}{\mathrm{d}\,t} = \frac{\mathrm{NO3}}{k_{\mathrm{NO3}} + \mathrm{NO3}}\, J(z,t)\,\mathrm{PHY} - \lambda_{\mathrm{PHY}}\,\mathrm{PHY} - G_{\mathrm{PHY}} - \Psi \tag{33}$$

Phytoplankton is grazed by zooplankton (G_{PHY}). Zooplankton grazing follows a non-linear function (eq. 35). A fraction ($1 - \epsilon_{\mathrm{ZOO}}$) of zooplankton grazing is lost due to sloppy feeding and fecal pellets. Zooplankton excrete dissolved inorganic nitrogen at a constant rate, λ_{ZOO}. Mortality of zooplankton is simulated using a quadratic (density dependent) approach ($\kappa_{\mathrm{ZOO}}\,\mathrm{ZOO}^2$). The upper closure of the model (generally the zooplankton mortality term) is assumed to have a large influence on model behaviour (Steele and Henderson, 1992).

$$\frac{\mathrm{d\,ZOO}}{\mathrm{d}\,t} = \epsilon_{\mathrm{ZOO}}\, G_{\mathrm{PHY}} - (\lambda_{\mathrm{ZOO}} + \kappa_{\mathrm{ZOO}}\,\mathrm{ZOO})\,\mathrm{ZOO} \tag{34}$$

with

$$G_{\mathrm{PHY}} = \frac{\mu_{\mathrm{ZOO}}\,\mathrm{ZOO}\,\mathrm{PHY}\,\mathrm{PHY}}{k_{phy}\,k_{phy} + \mathrm{PHY}\,\mathrm{PHY}} \tag{35}$$

Detritus is produced by sloppy feeding and fecal pellet production of zooplankton, and is degraded by bacteria, which are not explicitely considered in this model (λ_{DET}). Detritus sinks at a constant settling velocity of w_{DET}.

$$\frac{\mathrm{d\,DET}}{\mathrm{d}\,t} = (1 - \epsilon_{\mathrm{ZOO}})\, G_{\mathrm{PHY}} - \lambda_{pel}\,\mathrm{DET} - w_{\mathrm{DET}}\,\frac{\mathrm{dDET}}{\mathrm{d}\,z} \tag{36}$$

5.2 Model Setup

Phytoplankton maximum growth rate is set to a value of 1.5 d^{-1}, a value which is close to the maximum growth rate of phytoplankton as estimated by Fasham and Evans (1995) for this region, using non-linear optimization techniques and the data set of the 1989 NABE process

Table 6: Parameters for standard model simulations at 47 °N 20°W.

Parameter	Symbol	Value	Unit
phytoplankton parameters			
maximum growth rate	μ_{PHY}	1.5	d^{-1}
half-sat. const. for NO3 uptake	k_{NO3}	0.50	mmol N m^{-3}
PHY-specific attenuation coefficient	k_c	0.03	mmol N^{-1} m^2
water attenuation coefficient	k_w	0.04	m^{-1}
initial slope of P-I curve	α	0.025	(d W m^{-2})$^{-1}$
mortality	λ_{PHY}	0.04	d^{-1}
zooplankton parameters			
maximum growth rate	μ_{ZOO}	1.0	d^{-1}
half-sat. const. for grazing on PHY	k_{PHY}	1.0	mmol N m^{-3}
assimilation efficiency	ϵ_{ZOO}	0.75	
excretion rate	λ_{ZOO}	0.1	d^{-1}
mortality rate	κ_{ZOO}	0.05	d^{-1} mmol N m^{-1} m^3
detritus parameters			
decay rate	λ_{DET}	0.04	d^{-1}
sinking speed	w_{DET}	10.0	m d^{-1}
aggregation parameters			
shear rate	*shear*	0.84	s^{-1}
sinking exponent	η	1.17	-
sinking factor	B	1.10	$\mathrm{cm}^{-0.17}$ d^{-1}
stickiness	*stick*	0.1	-
breakup probability	b	1	-
cell size	m	0.002	cm
N content exponent	ζ	2.28	-
N content coefficient	C	5.67	nmol N $\mathrm{cm}^{-2.28}$

study (see table 6). Phytoplankton half saturation constant for NO3 uptake is set to 0.5 mmol N m^{-3}, a value which lies within the range presented by Eppley *et al.* (1969), and is close to the value found by Fasham and Evans (1995). The parameters for light attenuation by water and phytoplankton nitrogen (as a proxy for Chl *a*) and for the initial slope of

the PI-curve have been set to the same values as in Fasham *et al.* (1990). Zooplankton parameters also have been set to similar values as in Fasham *et al.* (1990), which close to what has been estimated for the northeastern North Atlantic (Fasham and Evans, 1995). Quadratic zooplankton mortality has been set to a value of 0.05, although Evans (1998) estimated it to be close to zero. Detrital sinking speed has been set to 10 m d^{-1}. This is less than the sinking speed of large fecal pellets which may sink at 100 m d^{-1} (Noji, 1989); it represents a compromise among a variety of groups such as ciliates and copepods. The aggregation parameters have been set to the same values as given in the previous chapter. Three experiments have been performed with this model: The "Base" run, where phytoplankton aggregates at relatively low rates, scenario "Sticky" where aggregation is enhanced by doubling stickiness and finally scenario "Detritus". In this last scenario, phytoplankton does not aggregate, neither does it sink. Instead phytoplankton mortality leads to the formation of detritus, i.e. in this model in contrast to the other two scenarios detritus consists of fecal pellets as well as of dead phytoplankton cells. Phytoplankton mass and number concentration at the lower boundary of the model are set to zero, while nitrate is mixed into the deepest box with a boundary concentration of 18.3 mmol N m^{-3}. The upper boundary for the evaluation of the aggregation and sedimentation equations is 2 cm, for reasons mentioned in the previous section.

5.3 Results and discussion

In the following sections, three simulations for the northeastern North Atlantic are presented and discussed. The "Base Run" shows the results for a model simulation with a aggregation and a low (0.1) stickiness. In scenario "Sticky" the stickiness is doubled (0.2) to enhance aggregation. Scenario "Detritus" describes the results of a model simulation where no aggregation takes place, but where dead phytoplankton is shifted towards the detrital pool, where, together with fecal pellets produced by zooplankton, it then sinks with a constant sinking speed of 10 m d^{-1}. The model initial conditions are vertical profiles for nitrate (increasing steadily from 2.6 mmol N m^{-3} at the surface to 18.3 mmol N m^{-3} in the deepest layer) and phytoplankton, which during winter is assumed to be distributed homogeneously throughout the model water column at almost zero concentrations. The initial size distribution is very steep ($\epsilon = 8$) i.e. most of the phytoplankton is present as single cells. The results presented in this chapter show the tenth year of every simulation.

5.3.1 The Base Run

The annual distribution of nitrate for the upper 400 m for the base run is shown in figure 18. Nitrate accumulates due to strong mixing during the winter months, and reaches maximum surface values of more than 9 mmol N m^{-3} in February and March. When phytoplankton starts to grow in late April, nitrate declines rapidly to values below 1 mmol N m^{-3}, and increases again towards summer due to recycling by zooplankton. Nitrate concentration during summer is low, and increases again when it is entrained into due to mixed layer deepening in autumn.

Figure 19 shows the vertical distribution of phytoplankton for the upper 400 m (grey shades), together with the concentration of aggregates (thin contour lines) sinking at a minimum speed of 10 m d^{-1}, i.e. the sinking speed of DET. In spring phytoplankton in the upper 50–75 m increases up to a maximum of almost 6 mmol N m^{-3}. The spring bloom within a few days declines to values < 0.5 mmol N m^{-3}, and is immediately followed by an increase in zooplankton concentration, reaching values of more than 2.5 mmol N m^{-3} in the upper 50 m (figure 20). Parallel to the increase in phytoplankton mass there is an increase in the concentrations of aggregates which sink faster than 10 m d^{-1} (aggregates larger than about 200 μm, contour lines in figure 19). The increase in the concentration of large aggregates is due to the rapid aggregation that takes place especially in the upper layers, and

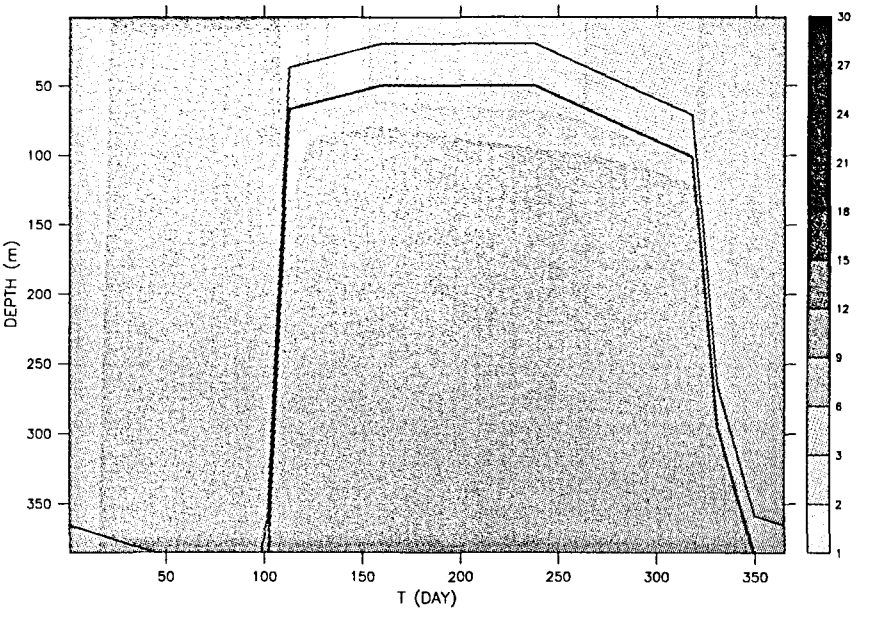

Figure 18: Nitrate and depth of upper and lower thermocline for the base model simulation at station NABE (upper 400 m). Depth of upper and lower thermocline is plotted by thin and thick line, respectively. Nitrate is contoured by a thin line, unit is mmol N m^{-3}.

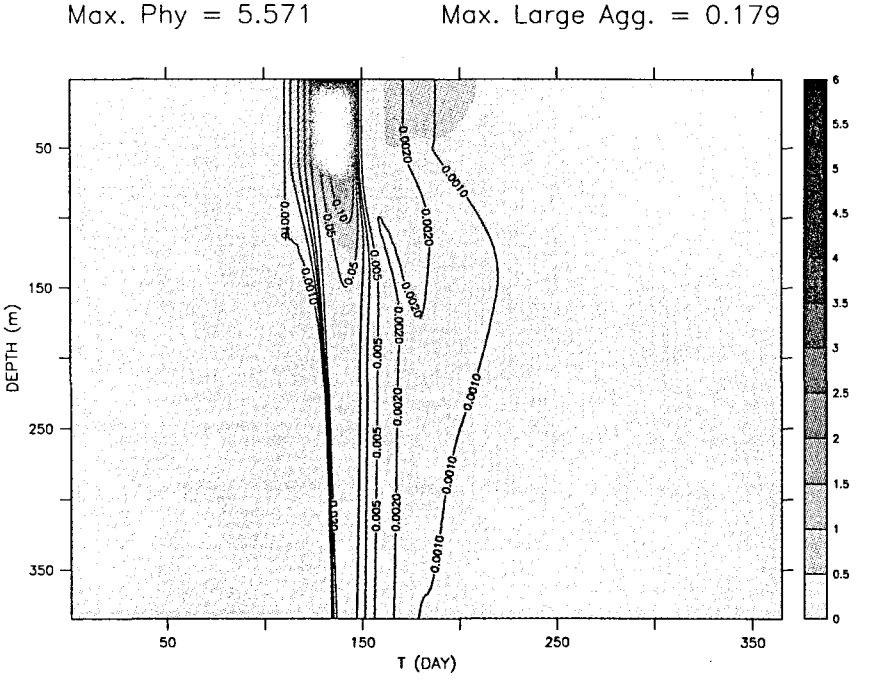

Figure 19: Mass of total phytoplankton and aggregates sinking faster than 10 m d^{-1} (minimum diameter $\approx$ 200 μm) for the base model simulation at station NABE (upper 400 m). Phytoplankton mass is shown by grey shades, mass of aggregates sinking faster than 10 m d^{-1} is shown by contour lines at approximately logarithmicp intervals. Unit is mmol N m^{-3}.

causes an increase in the average mass sinking speed, reaching highest values of more than 100 m d^{-1} at 400 m (no figure). During summer, phytoplankton concentration is below 1 mmol N m^{-3}. Phytoplankton aggregates are relatively small because the large aggregates that have formed during the spring bloom have settled out of the model water column, and the relatively low concentrations during summer do not promote mass aggregation of particles as takes place in spring.

Fecal pellet concentration, which of course is coupled to zooplankton abundance, is shown in figure 20. Immediately following the phytoplankton bloom, zooplankton starts to grow until

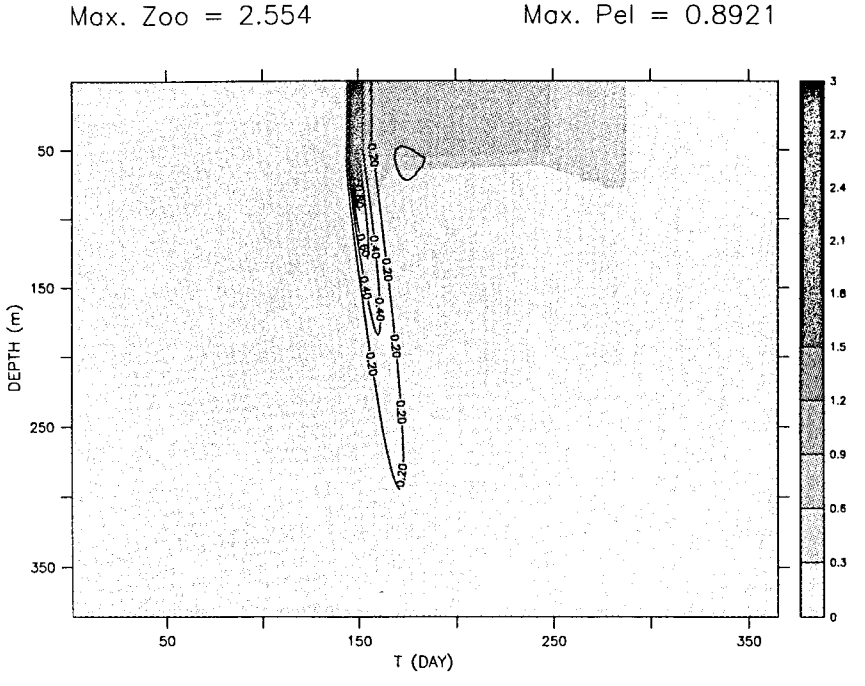

Figure 20: Zooplankton and fecal pellet concentration for the base model simulation at station NABE (upper 400 m). Zooplankton is shown by grey shades, fecal pellet concentration is contoured by a thin line, unit is mmol N m^{-3}.

it reaches a maximum of 2.5 mmol N m^{-3}. Zooplankton concentration during summer is almost the same as phytoplankton concentration, because zooplankton grazing then controls phytoplankton growth. Yet the largest increase of pellet concentrations to a maximum value of 0.8 mmol N m^{-3} can be found around day 140, when zooplankton graze large amounts of the phytoplankton bloom. Fecal pellets sink to deeper layers with a constant sinking speed of 10 m d^{-1}, so it takes about 40 days for the pellets to reach a depth of 400 m. Although maximum fecal pellet concentrations are higher than the concentration of large aggregates settling with a minimum speed of 10 m d^{-1}, the aggregates in total sink faster than the pellets, and thus reach a depth of 400 and 800 m before the pellets. Thus the

first peak of sedimentation in 400 and 800 m depth, which occurs around day 150, consists mainly of phytoplankton (figure 21). There is a steep increase in total shallow as well

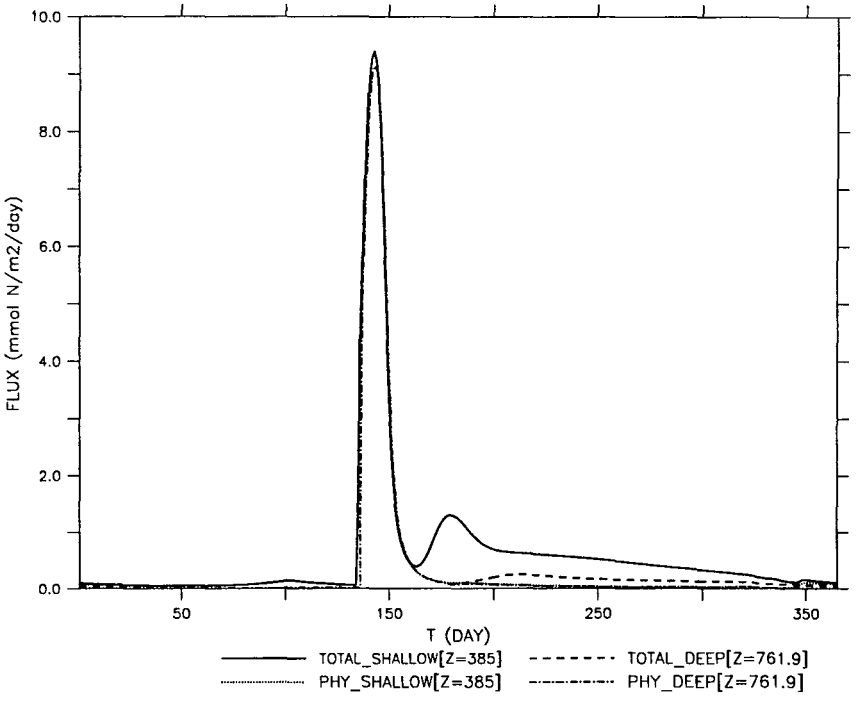

Figure 21: Sedimentation in 400 and 800 m for the base model simulation at station NABE. Total flux through 400 and 800 m is denoted by solid and broken lines, respectively. Phytoplankton flux through 400 and 800 m is denoted by dotted and broken line with dots (see also figure legend, and text for further explanations). Units are mmol N m^{-2} d^{-1}.

as deep flux shortly after the spring bloom, most of which can be attributed to settling phytoplankton. As soon as deep and shallow flux reach their maximum of almost 10 mmol N m^{-2} d^{-1} around day 140, they sharply decline again to low values around 0.5 mmol N m^{-2} d^{-1}, with a second hump in shallow flux of ca. 1 mmol N m^{-2} d^{-1} in early summer. This second increase constists of fecal pellets, which now have reached a depth of 400 m (see also figure 20). Little amount of this flux reaches greater depth, because pellets in this model sink too slowly, and are remineralized before they can settle out of the model water column. Thus, sedimentation stays low for the rest of the year, with little contribution of phytoplankton.

Total annual phytoplankton production integrated over the whole water column equals 2751 mmol N m^{-2}, which is about 218 g C m^{-2}. About 57% of this production is grazed by zooplankton. Integrated over one year, total shallow flux equals 228 mmol N m^{-2}, of which 62% is of phytoplankton. 63% of this total shallow flux reach a depth of 800 m,

comprising to 86% of phytoplankton, i.e. it is mainly phytoplankton which contributes to the deep flux, plus a small amount of fecal pellets (see also table 8 in chapter 7 at the end of this work).

5.3.2 Scenario "Sticky"

When doubling the stickiness, phytoplankton is assumed to aggregate much more efficiently, before it becomes subject to mortality or even zooplankton grazing. As shown in figure 22 this effect indeed takes place: phytoplankton in this model scenario only reaches a maximum concentration of less than 4 mmol N m^{-3} (which is a decrease of almost 30% of that of the base run), and the concentration of large aggregates is elevated.

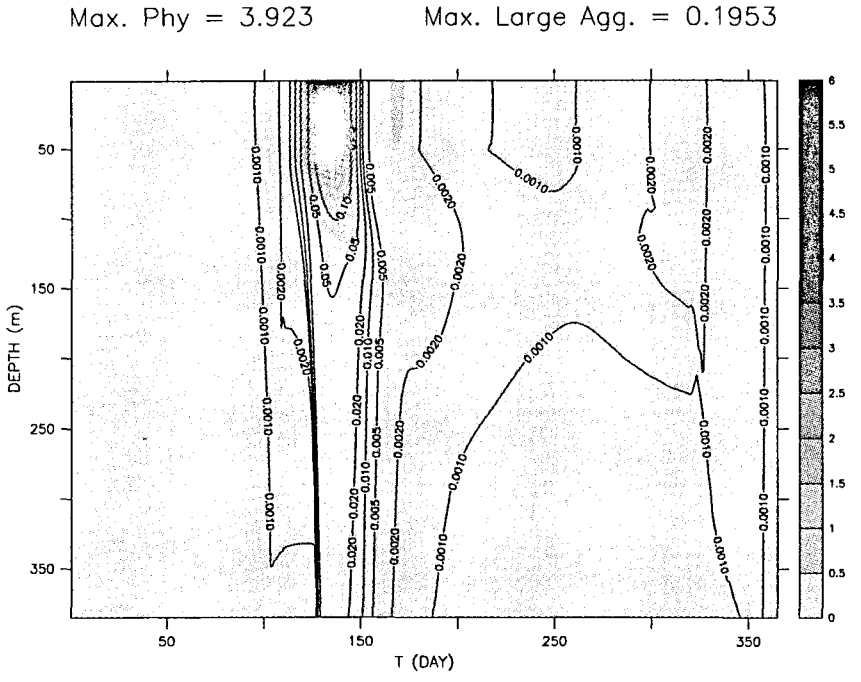

Figure 22: Mass of total phytoplankton and aggregates sinking faster than 10 m d^{-1} (minimum diameter $\approx$ 200 μm) for the "Sticky" scenario at station NABE (upper 400 m). For notations and units see figure 19.

Zooplankton maximum concentration is less than 50% that of the base run (no figure). Resulting from the increase in stickiness, shallow as well as deep flux are enhanced and to a larger extent consist of phytoplankton, reaching peak values of around 12 mmol N m^{-2} d^{-1} during the time of the phytoplankton spring bloom (see figure 23).

Integrated over depth and one year phytoplankton produces 2173 mmol N m^{-2}, of which 47% is grazed, i.e. not only the total mass grazed by zooplankton is reduced when com-

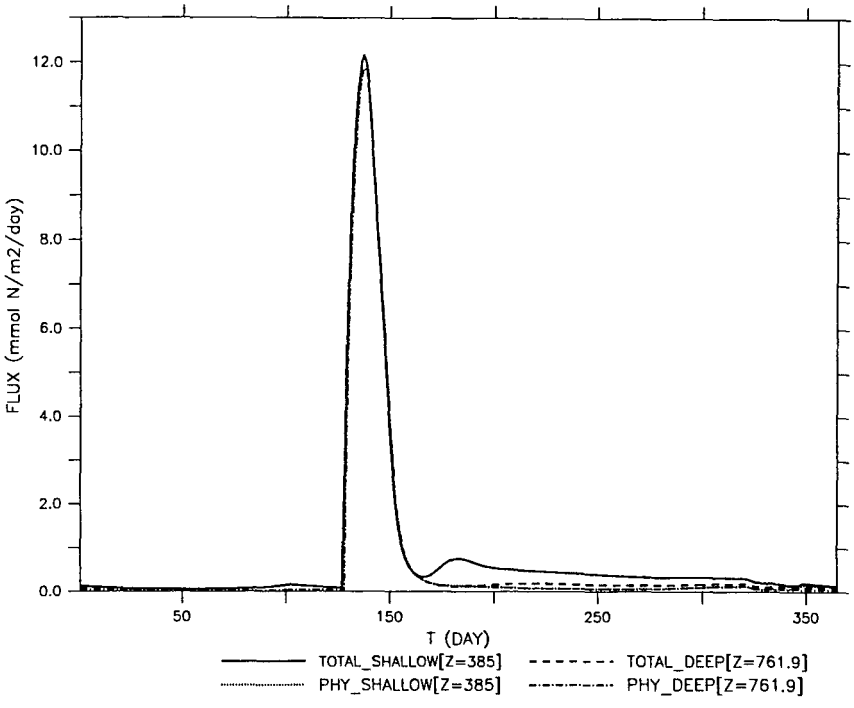

Figure 23: Sedimentation in 400 and 800 m for the base model simulation with increased stickiness at station NABE. For notations and units see figure 21.

pared with the base run, but also the influence of zooplankton grazing on phytoplankton development is diminished. Instead, shallow as well as deep flux are enhanced, the flux through 400 m being 296 mmol N m^{-2} (30% more than in the base run), and the deep flux 237 mmol N m^{-2}, which is more than 165% of that of the base run. In other words, more than 80% of the shallow flux reaches 800 m, and phytoplankton constitute almost all (97%) of the deep flux.

5.3.3 The "Detritus" Scenario

This model run has no aggregation, but a constant phytoplankton mortality which in this scenario does not produce nutrients, but together with fecal pellets makes up the detrital pool which sinks at a constant speed of 10 m d^{-1}. Figure 24 shows the development of phytoplankton, again for the upper 400 m of the model water column. (Of course, this time there are no phytoplankton aggregates.)

Phytoplankton as well as zooplankton (no figure) shows about the same patterns as in the base model simulation, with higher maximum concentrations of about 5.8 and 2.2 mmol N m^{-3} for phytoplankton and zooplankton, respectively. Integrated primary production is less than in the base run (2264 mmol N m^{-2} y^{-1}) – this is probably because phytoplank-

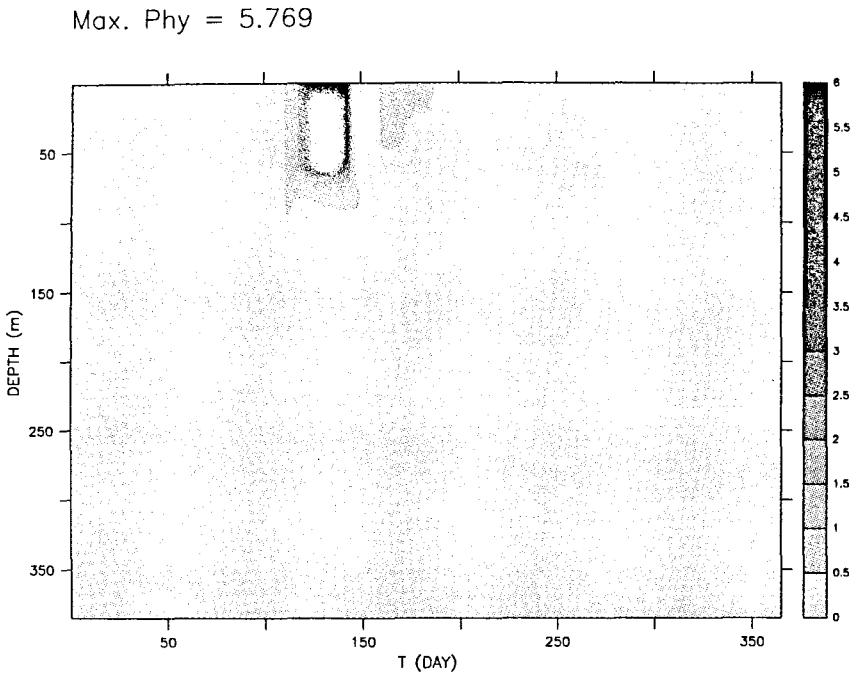

Figure 24: Mass of total phytoplankton for the "Detritus" scenario at station NABE (upper 400 m). Phytoplankton mass is shown by grey shades. Unit is mmol N m^{-3}.

ton mortality does not increase nutrients in this model, but produces additional detritus, which finally sinks out of the upper, well-lit layers (see also chapter 4 for the influence of phytoplankton mortality and recycled production). As a consequence, zooplankton grazing is only 1324 mmol N m^{-2} y^{-1}, but still it zooplankton grazes 58% of phytoplankton production, almost the same as in the base model simulation.

Sedimentation is shown in figure 25. In this simulation, of course there is only one type of settling material (detritus), and the contribution of (live) phytoplankton to sedimentation is zero.

This model shows a higher baseline of sedimentation, because here sinking speed of particulate matter does not depend on time, but is constant throughout the year. The peak sedimentation following the spring bloom is not as pronounced as in the previous two simulations, and lower, which is due to the low, constant sinking speed after the spring bloom. Little amount of this flux reaches greater depth. When integrating the model fluxes over one year, shallow sedimentation is enhanced (337 mmol N m^{-2}) in comparison to the aggregation models, which may be attributed to the somewhat higher non-bloom sedimentation in winter, early spring, late summer and autumn. Only 26% of this flux reach a depth of 800 m, which is only 63% of that of the base runs. Annual zooplankton grazing on phy-

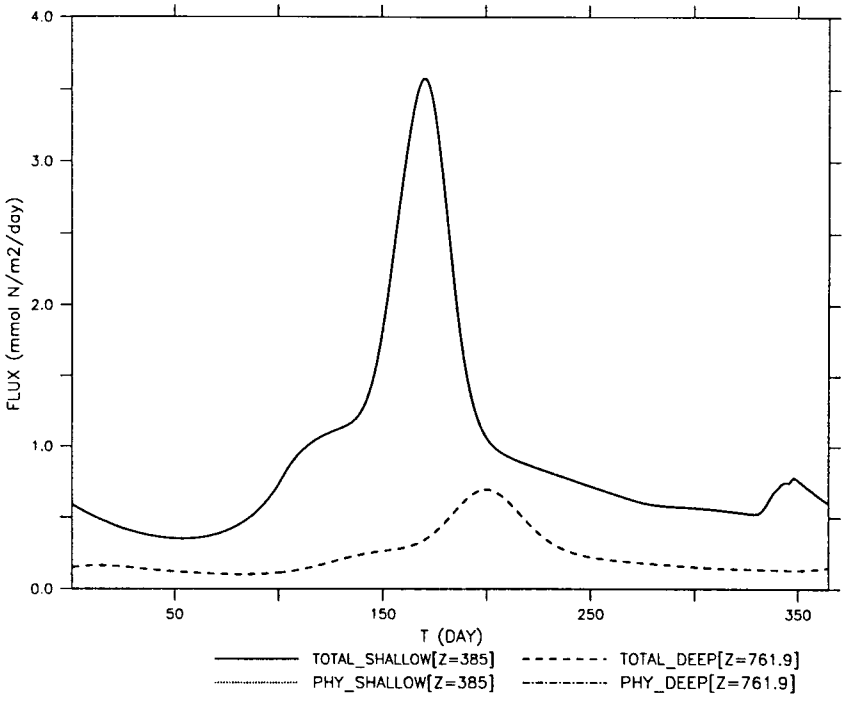

Figure 25: Sedimentation in 400 and 800 m for the model simulation with the detritus model at station NABE. For notations and units see figure 21. For further explanations see text.

toplankton is comparable to the relative grazing pressure in the base run. Using a model where phytoplankton mortality leads to the production of detritus sinking at a constant sinking speed in this region not only decreases sedimentation at greater depths, but may also lower other annual flows as annual primary production and zooplankton grazing.

5.4 Discussion

The so-called "BIOTRANS" or "NABE" site at 47°N 20°W has been extensively studied for many years. Koeve and Zeitzschel (in prep.) note that Chl *a* concentrations on this station may be as high as 4.5 mg Chl *a* m^{-3}, a value which agrees well with the results from the aggregation simulation, and are higher than what was found during the 1989 North Atlantic Bloom Experiment (Lochte *et al.*, 1993). Integrated primary production in the model simulations shows a sharp increase to a maximum value about 2.8 g C m^{-2} d^{-1} (no figure), which is about 50% higher than was been measured in 1989 (Lochte *et al.*, 1993). Mesozooplankton grazing on phytoplankton in April and May 1989 on this station was low (Dam *et al.*, 1993) and dominated by small zooplankton. Dam *et al.* estimated the proportion of primary production that has been removed by zooplankton grazing during

the spring bloom to be less than 3% per day. Based on respiratory demand of zooplankton, Lenz *et al.* (1993) estimated about 50% of the phytoplankton production to be grazed by mesozooplankton. The question whether micro- or mesozooplankton is the dominant grazer of phytoplankton at this site in spring, and how much of the phytoplankton production is being grazed by zooplankton cannot be answered within this work; still is clear that some proportion of phytoplankton escapes zooplankton grazing and settles below the euphotic zone to deeper waters (Lampitt, 1985; Billet *et al.*, 1983).

Figure 26 shows the annual cycles of nitrogen and biogenic silica (which can be seen as a proxy for diatoms and silicoflagellates) sedimentation in 500 m at station NABE (Fehner, in prep.). There is a spring peak in N sedimentation every year, with variations in its magnitude of about 100%. This peak in N-Flux is usually accompanied by a peak in biogenic silica sedimentation, so there is evidence for rapid diatom settlement to deeper layers, which may come either as intact cells, or as empty frustules or in fecal pellets.

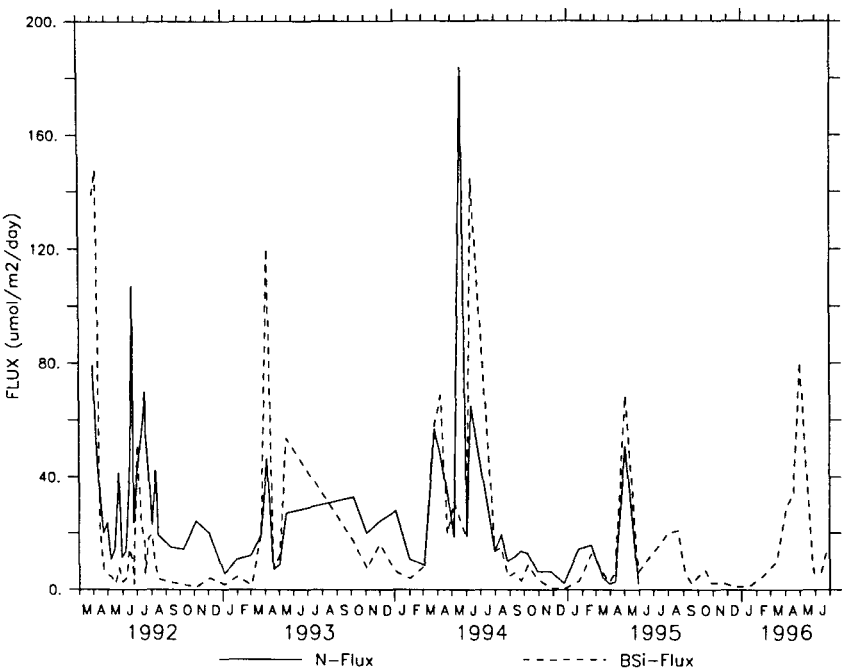

Figure 26: Sedimentation of particulate organic nitrogen (solid line, for 1992 – 1995 only) and biogenic silica (broken line) in 500 m for 1992 – 1996 at 47°N, 20°W. Data kindly provided by U. Fehner.

The peak N sedimentation in the data is several orders of magnitude less than the peak of the model simulations. Peak fluxes of the model simulation of almost 12 mmol N m^{-2} d^{-1} (scenario "Sticky") and even almost 4 mmol N m^{-2} d^{-1} in the detritus scenario greatly exceed the peaks of nitrogen sedimentation that can be found in the trap data. Nevertheless,

an about nine fold increase of sedimentation in spring, from 0.02 mmol N m^{-2} d^{-1} to about 0.18 mmol N m^{-2} d^{-1} at this side in 1994, has not been found with the detrital model, but is only given (and exceeded) by the aggregation model. Keeping in mind that that trap data at most give an average over a period of eight or more (e.g. Honjo, 1993, Fehner, in prep.) days for sedimentation, but the model presented here gives daily values for sedimentation, with a large variation from day to day, a more appropriate comparison of model and data would be a model flux that has been averaged over the sampling intervals of sediment traps. This type of comparison will be presented in the next chapter.

Data from sediment traps indicate that a large amount of the spring bloom sedimentation can be attributed to settling diatoms. In deeper moorings, where Honjo and Manganini (1993)found a high number of *Chaetoceros* shells and a high proportion of opal, as well as in shallow depths where Deckers (1991) found a high proportion of diatoms, dominated by *Thalassionema nitzschoides*, *Chaetoceros decipiens* and aggregates of *Nitzschia seriata* which accounted for more than 37% of the phytoplankton collected at 80 m. The latter two species are known as colony-forming species and have been found in aggregates (Alldredge and Gotschalk, 1989). The importance of diatoms for the sedimentation of the 1989 experiment has been confirmed by HPLC analyses (Meyerhöfer, 1994). These findings correspond with the 1989 data, when Honjo and Manganini (1993) found that the spring bloom penetrated to the ocean interior within a few weeks, with apparently accelerated settling speed at greater depths and that it accounted for 50% of annual mass flux at 48°N. Yet they also note that there was an apparent collection inefficiency with this trap, because coccoliths and coccospheres at 1000 m depth were sampled at lower rates than in the deeper traps. An annual nitrogen flux of 15.6 mmol N m^{-1} at a depth of 1000 m has been found by Honjo and Manganini (1993), which is far less than the results from model solutions presented here. Either the aggregation model overestimates export flux, or the trap data underestimate sedimentation. Deposition of large aggregates to the sea floor at this particular site has been reported by various authors (Billet *et al.*, 1983; Lampitt, 1985). Recent investigations have shown that most likely sediment traps do not catch large aggregates (Shaw *et al.*, 1998). As the aggregation model reproduces the sedimentation pattern following the spring bloom with almost immediate peak sedimentation at all depths, but most likely overestimates the extent of these peaks as well as the annual amount of sedimentation, perhaps more detailed investigation of processes that affect the mass of settling material, but not its size distribution and sinking speed, such as degradation and remineralization of organic matter

in deeper layers is necessary.

Scenario "Sticky" clearly shows that aggregation may decrease the time phytoplankton is available for zooplankton, and can have a large effect not only on sedimentation, but also for the upper ocean biogeochemistry itself. Still, the model stickiness with is quite low, as values e.g. of 0.5 and even more have been found in laboratory experiments for diatom aggregates (Kiørboe *et al.*, 1990; Alldredge and McGillivary, 1991; Engel, 1998). Thus aggregation not only governs the magnitude and the extent of sedimentation especially at greater depths, but also can have a large effect of the development of the pelagic community that follows the phytoplankton spring bloom. If mesozooplankton is considered in this model, it is likely that the maximum grazing rate of 1 d^{-1} is too high for this region. Lenz *et al.* (1993) estimated grazing rate of 0.165 - 0.561 d^{-1}. So presumably even if the aggregation model would be run with a lower grazing rate, phytoplankton concentrations would be protected from becoming unrealisticly high (because of the density-dependent losses of aggregation and sedimentation) at the time of the spring bloom, when there is neither nutrient-dependent nor sufficient grazing control of phytoplankton growth.

6 Simulations for the Arabian Sea

The importance of considering aggregation in a biogeochemical model of ocean biogeochemistry has been tested with simulations performed for two locations in the Arabian Sea, one located in the open ocean at 10°N 65°E, and one located close to the Oman coast, at about 17°N, 60°E. The same experiments as performed in the NABE simulation have been performed on these two stations in the Arabian Sea. The first location (hereafter called"S15") serves the purpose of checking the model outcome in an almost oligotrophic region, where phytoplankton is known to built a deep chlorophyll maximum almost throughout the year. Little sedimentation has been found on this site, with little variation throughout the year. The second location, hereafter named as "S04" in accordance with the notation used by the US JGOFS process study, has been chosen as an example for the region influenced by the Findlater Jet, and by lateral advection of upwelled waters. This region is known to show a strong biological response to the monsoonal forcing, and also exhibits a strong seasonal cycle of sedimentation with maxima of nitrogen and biogenic silica sedimentation (Honjo, unpubl.) There exists a comprehensive data set, constisting of six vertical profiles for nitrate, Chl *a*, primary production and other data measured during the US JGOFS process studies in 1995 (nitrate data by L. Codispoti, Chl *a* and primary production by R. Barber, as available through the US JGOFS data system `www1.whoi.edu/jgofs.html` June/August 1998, see also Morrison *et al.*, 1998). Together with the two profiles measured by the German JGOFS cruises in August 1995, alltogether there are eight days where model profiles can be compared with data. For the second region, additionally data for vertical flux from sediment traps have been included in the model comparison with data (data by S. Honjo as available through the US JGOFS data system `www1.whoi.edu/jgofs.html`, see also Lee *et al.*, 1998).

6.1 Hydrography and biology of the Arabian Sea

6.1.1 Hydrography

The Arabian Sea is a more or less triangular basin, with its largest zonal extent reaching about 3000 km, and a slightly smaller meridional extent. Its boundaries may be roughly defined in the south by the equator, in the east by the land masses of Africa and the Arabian Peninsula. To the north and northwest its boundaries are given by Pakistan

and the Indian subcontinent, while to the east they are given by the western edge of the Maldives and Lakshadweep to the west coast of India at about 18°N. Its bottom topography is characterized by the Carlsberg Ridge located in the southern part of the Arabian Sea and the Murray Ridge in the north off the Pakistani coast (see figure 27).

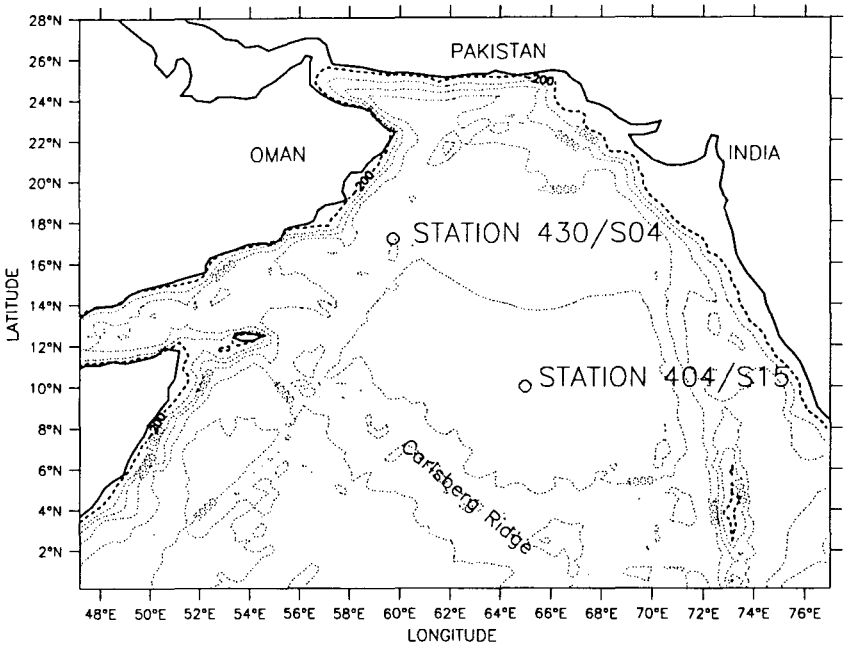

Figure 27: Bathymetry of the Arabian Sea and locations of two sample stations of the 1995 cruises. Bottom topography is shown by contours. The 200 m depth contour is drawn as thick broken line. The locations of two stations samples on leg M32/5 and on the US American cruises during 1995 have been marked by open circles.

In the middle of the Arabian Sea, depth shoals from 4000 m to 3000 m from 14°N to 21°N, respectively. The continental shelf, as given by the 200 m depth contour, is up to 350 km wide along the coast of India, but is narrow along the Arabian coast and less than 50 km wide at the entrance of the Red Sea (see figure 27). Because the Arabian Sea has a small size in relation to its coastal areas – about 25% of total area is occupied by coastal regimes – the influence of the coastal area on open ocean processes is expected to be high (Shetye *et al.*, 1994).

The annual cycle of physical and biogeochemical variables in the Arabian Sea is governed by the influence of two monsoons, the southwest monsoon (SWM) blowing during May – September, with maximum wind speeds of more than 16 m sec^{-1}, and the weaker northeast monsoon (NEM) during November – February. Winds are generally low during the inter-monsoon phases. The wind blowing parallel to the coast of the Arabian Peninsula leads to

coastal upwelling of cold, nutrient rich water along the coasts of Yemen and Oman, as well as along the Somali coast. During the SWM, high wind speeds are induced offshore the Arabian Peninsula due to the formation of the so called Findlater Jet (Findlater, 1969), flowing from the horn of Africa to northwest India. Updoming of the pycnocline from open sea divergence northwest of the jet axis, caused by the curl of wind stress on the sea surface, has been hypothesized to lead to an input of nutrient from deeper layers into the euphotic zone. Southeast to the jet axis, the gradient of the wind speed normal to its direction leads to downwelling, i.e. a deepening of the mixed layer. Mixed layer depths during that time in this region reach up to 100 m (Bauer *et al.*, 1993). The deeping of the mixed layer is accompanied by entrainment of nutrients due to mixing with deep water. Using numerical experiments McCreary *et al.* (1996) found that Ekman suction is important to the interior flow in the central and western part of the Arabian Sea. Coastal upwelling is absent during the NEM in the northern Arabian Sea. The effects of the periodic forcing due to the SWM and NEM are lower for the central and eastern parts of the Arabian Sea.

The surface irradiation increases during winter and spring towards summer solstice. During May cloud cover is at its minimum in the Arabian Sea, leading to a maximum of surface irradiation, with values of about 280 W m^{-2} (Brock *et al.*, 1994). During summer cloudiness increases until it reaches its maximum in August. Therefore, lowest irradiation can be found in August, with values down to 170 W m^{-2}. Figure 28 shows the annual cycle of cloudiness based on monthly mean values as given in the Esbensen Kushnir data set for two locations in the Arabian Sea, at 10°N 65°E and at 17°N, 60°E.

6.1.2 Biogeochemistry

The biological variables in the western Arabian Sea reflect the pattern exhibited by the physical forcing. Pigment concentration as given by satellite (NIMBUS-7 Coastal Zone Color Scanner) observations show low chlorophyll concentration during both intermonsoon phases. Markedly elevated concentration (about 2 mg m^{-3} compared to 0.5 mg m^{-3} or less during the intermonsoon phase) appear at the height of the SWM in August, after monsoonal forcing has injected nutrients into the euphotic zone for most parts of the western Arabian Sea (Banse, 1987). The increase in pigment concentration is largest for the region close to the Pakistani coast, as well as in the region west of 65°E and north of 15°N (panels 4c, 3b and 3a in figure 1, Banse 1994), and lowest for regions south of 15°N. Only in the northernmost parts of the Arabian Sea, on the Pakistani shelf, can an increase in pigment

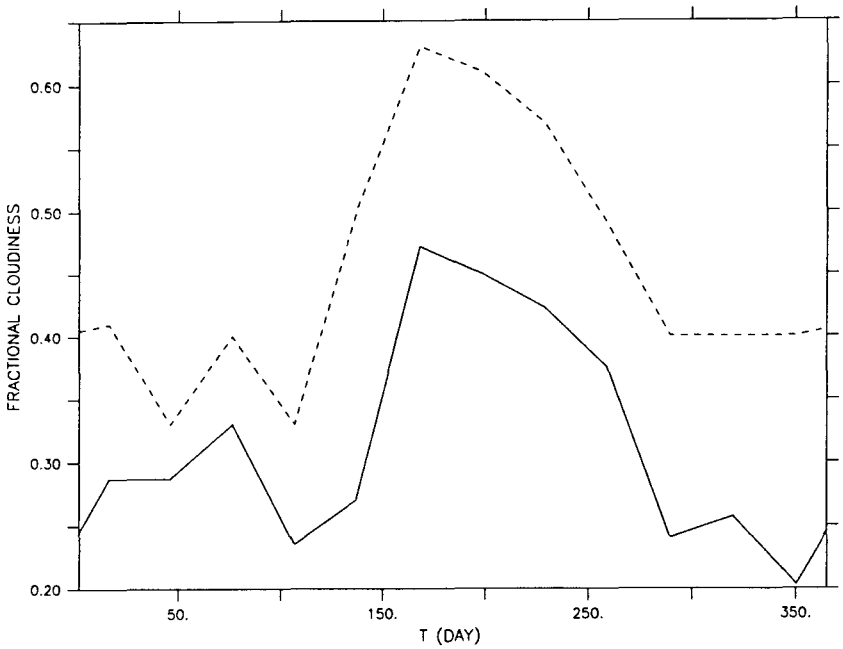

Figure 28: Cloudiness climatological means for two locations in the Arabian Sea, 10°N 65°E and 17°N 60°E. Cloudiness is given in fractions.

concentration be found during the NEM.

The vertical distribution of phytoplankton standing stock is discussed in detail by Banse (1994). Especially during the intermonsoon phases, when the mixed layer is shallow, surface nutrients are low and irradiation is high large parts of the Arabian Sea attain the "typical tropical structure" (TTS)p with low chorophyll concentration in the mixed layer and a Deep Chlorophyll Maximum (DCM) accompanied by high nutrient concentration. In this case, phytoplankton in the DCM have sufficient light and nutrients for a positive net photosynthetic rate. Brock et al. (1993) suggest that a DCM will be present throughout almost the entire Arabian Sea before and afterwards the SWM. In contradiction, Banse (1994) notes that this is not likely to be the case, as the seasonal thermocline in spring may subdivide a mixed layer which was already nutrient depleted, and therefore, the phytoplankton below the pycnocline experiences low nutrients as well as low light. With eroding pycnocline and nutrient injection into the mixed layer, the DCM vanishes below and northwest of the Findlater Jet during the SWM.

It is assumed that copepods play an important role in the Arabian Sea upwelling especially during the SWM, whereas in oligotrophic waters microzooplankton commonly dominate the food web. Smith *et al.* (1991) in a comparison of zooplankton dry weight biomass collected by net hauls with other upwelling areas showed that zooplankton has the largest

stocks off Ras Hafun, i.e. at the coast of Somalia, with biomasses of 8.1 g DW m^{-2} in August, whereas low (meso)zooplankton biomass has been found in the vicinity of 10°N (ca. 1 g DW m^{-2}, Smith *et al.*, 1991). They also note that there is little variation in zooplankton biomass during the year. This has been confirmed by Wishner and Gowing (unpubl.) during the 1995 study. Given the relatively low primary production during the intermonsoon phases, zooplankton persist at remarkably high concentration during these times, for yet unknown reasons (SCOR, 1995). A single species, *Calanoides carinatus* has been found to make up 40% of the zooplankton biomass during the SWM in the upper layer (Smith, 1982; Smith, 1984).

Particle sedimentation in the Arabian Sea especially in the western parts shows a high seasonality, which is related to the monsoon seasons. More than 50% of annual particle fluxes appear during the SWM as indicated by opal and biogenic carbonate fluxes (Haake *et al.*, 1993), with a temporal decoupling suggesting a seasonal succession of coccolithophorid and diatom species in the surface layers of this region. Still, even during the intermonsoon periods shallow sedimentation with 0.4 - 1 g C m^{-2} d^{-1} has been found to be relatively high (Passow *et al.*, 1993; Pollehne *et al.*, 1993b). The study of Pollehne *et al.* (1993a) even revealed that most of the sedimented material originated from the DCM.

6.1.3 The JGOFS Process Study 1995 – Cruise METEOR 32/5

The Joint Global Ocean Flux Study (JGOFS) as a core project of the International Global Biosphere Program (IGBP) is aimed towards the investigation of the time–varying flows of carbon and associated elements in the ocean, and their exchange with the atmosphere, the sea floor and continental boundaries (SCOR, 1992). As a part of the JGOFS program, the Arabian Sea Process Study focuses on the quantification of carbon flows in the Arabian Sea, to determine the role the Arabian Sea plays in the global carbon cycle and to investigate the biogeochemical response to seasonally varying forcing (SCOR, 1995). During 1995 and 1997, extensive investigations especially in the western part of the Arabian Sea were carried out under the auspices of JGOFS, with participation of many countries. Two cruises carried out by German JGOFS with focus on biogeochemical cycling have taken place in 1995, one during the intermonsoon phase (M32/3), and one during the SWM (M32/5). During these cruises, sampling took place mostly with respect to the spatial distribution of biogeochemical variables and flows. In 1997, another cruise (SO120) was dedicated to the investigation of the temporal development of the biological processes in freshly upwelled

water off the Oman coast during the SWM. For this purpose, a drifter was set out close to the coast and followed for 14 days. Only the results from the first study will be used for this 1-dimensional modeling exercise. For this purpose, a grid model will be presented, that combines aggregation with further biological processes, as described in the previous chapter. For validation of this model the 1995 data of the german cruise M32/5 during the SWM plus the data of the six US JGOFS cruises TTN043 (January), TTN045 (March/April), TTN049 (July), TTN050 (August/September), TTN053 (November) and finally TTN054 (December) 1995 will be used. Because during the SWM the largest gradients in the biological variables can be expected, in the following sections, some of the results of the cruise M32/5 (SWM 1995) will be presented in detail. The data of other cruises will be presented and discussed together with the corresponding model simulations.

The cruise consisted of three sections, leading from the equator along 65°E up to 14.5°N (in the following text named T1), then northeastward towards the Oman coast at Ras al Madraka (T2) and back to 62°E 16°N (T3). Figure 29 shows the nitrate profile for T1 for the upper 200 m. Throughout the entire euphotic zone nitrate is exhausted to less than 3 mmol m^{-3} – in fact, nitrate in the upper layer was below detection limit. The corresponding Chl *a* profile shows very low values, which are slightly increasing to the north, from < 0.2 mg m^{-3} to about 0.5 mg m^{-3} (figure 30).

Phytoplankton consisted mainly of small dinoflagellates (41% of phytoplankton carbon by Utermöhl counting), and some diatoms and flagellates (both about 25% of phytoplankton carbon). The zooplankton community mainly consisted of ciliates, but little mesozooplankton could be found (Zeller, pers. comm.). Integrated primary production by means of the ^{14}C-method yielded 1 g C m^{-2} d^{-1}. Despite of the SWM, station S15 (denoted as "Station 404" in figures 29 and 30) showed the features of a typical oligotrophic region, so it has been chosen as one of three sites for model simulation.

On the second transect towards the Oman coast, the cruise went from the oligotrophic region into the area influenced by the Findlater Jet and then into coastal upwelling. Figure 31 shows the nitrate distribution for the upper 200 m, where the pattern has changed dramatically in comparison to T1. Nitrate was still low at the surface at 65°E but started to increase towards 62°E until it reached a maximum of about 8 mmol N m^{-3} at 61.25°E, a very high value for the open ocean. It decreased to values < 2 mmol N m^{-3} until it raised up to more than 17 mmol N m^{-3} in the coastal upwelling. The offshore increase in nutrient concentration can be attributed to the advection of cold, nutrient rich water from coastal

upwelling, most probably in form of a filament (Morrison *et al.*, 1998). Evidently it has been crossed by the ship cruise leading to a decrease in temperature at 62°E (Waniek, pers. comm.) and an increase in nutrient concentration. Chl *a* values as calculated from fluorescence increased from values around 0.4 mg Chl *a* m^{-3} at 65°E to more than 1.4 mg Chl *a* m^{-3} in the filament (figure 32). The increase of Chl *a* in the coastal upwelling zone is quite low, when compared to e.g. CZCS data, which even report values up to 8 mg m^{-3} for that time (Brock *et al.*, 1993).

Station S04 (denoted as "Station 430" in figures 31 and 32) at 17°N 60°E has been sampled two times, first on T2 on August 1, and a second time on T3 6 days later. Both stations showed quite uniform profiles of low Chl *a* and other standing stock variables. About 30% of phytoplankton carbon consisted of diatoms (results from Utemöhl countings, data by v. Bröckel, unpubl.), mainly of the species *Rhizosolenia sp.*. On the first sampling date (1. August) about 45% of phytoplankton carbon could be attributed to dinoflagellate species mainly of the genus *Ceratium*, while of the second sampling profile about 42% of phytoplankton carbon were diverse flagellates, with a large amount of the colony-forming prymnesiophyte *Phaeocystis sp.*. Integrated primary production was very high with 2.0 and 2.5 g C m^{-2} d^{-1} for the station samples on 1 and 7 August, respectively. Because this station has been sampled many times, and even data for sediment traps are available for several depths (Honjo, unpubl.), it has been chosen as a second site for model experiments with the 1-dimensional model.

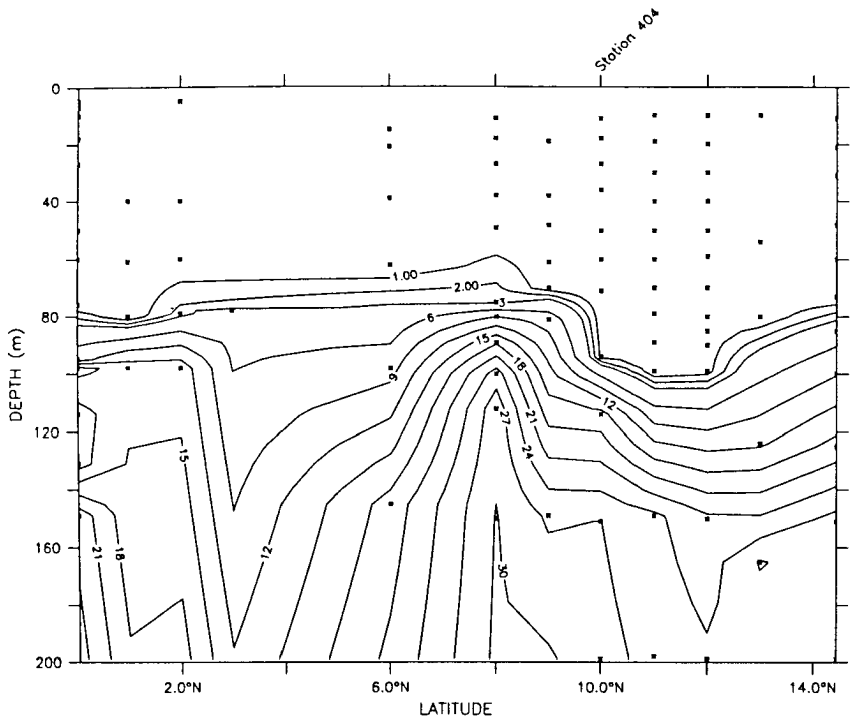

Figure 29: Vertical distribution of nitrate along 65°E for the upper 200 m (cruise M32/5, section T1). Sample locations have been marked by dots. Unit is mmol N m^{-3}.

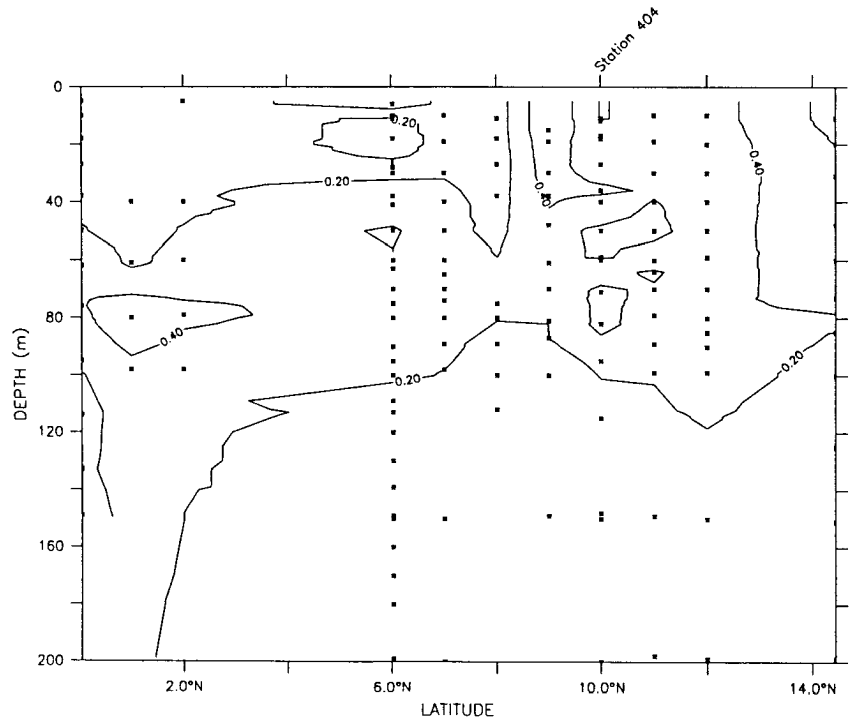

Figure 30: Vertical distribution of Chl *a* measured by fluorometric method along 65°E for the upper 200 m (cruise M32/5, section T1). Sample locations have been marked by dots. Unit is concCHL.

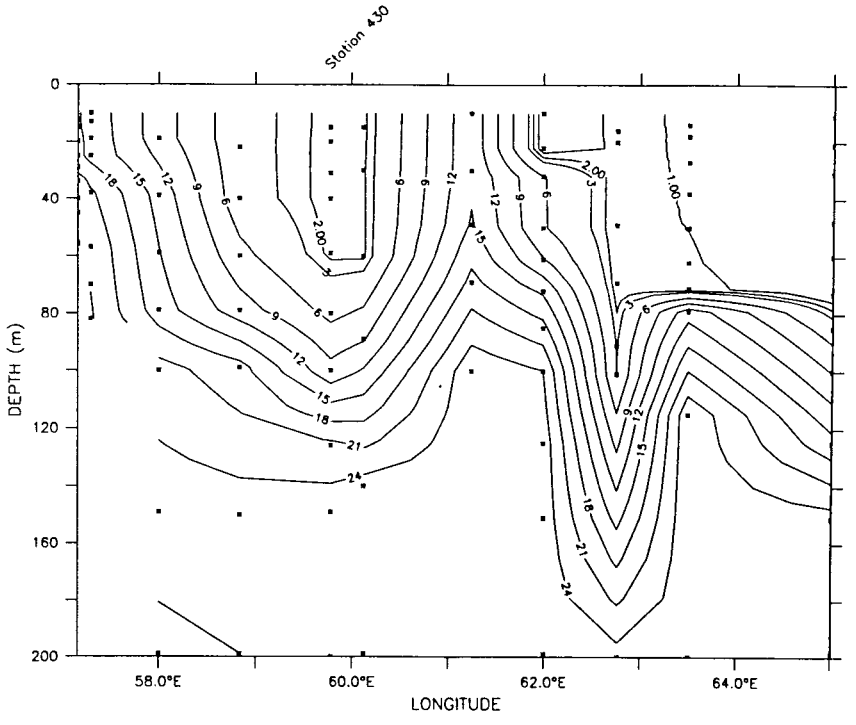

Figure 31: Vertical distribution of nitrate from 14°N, 65°E towards Ras al Madraka, Oman, for the upper 200 m (cruise M32/5, section T2). Data have been plotted vs. longitude. Sample locations have been marked by dots. Unit is mmol N m^{-3}

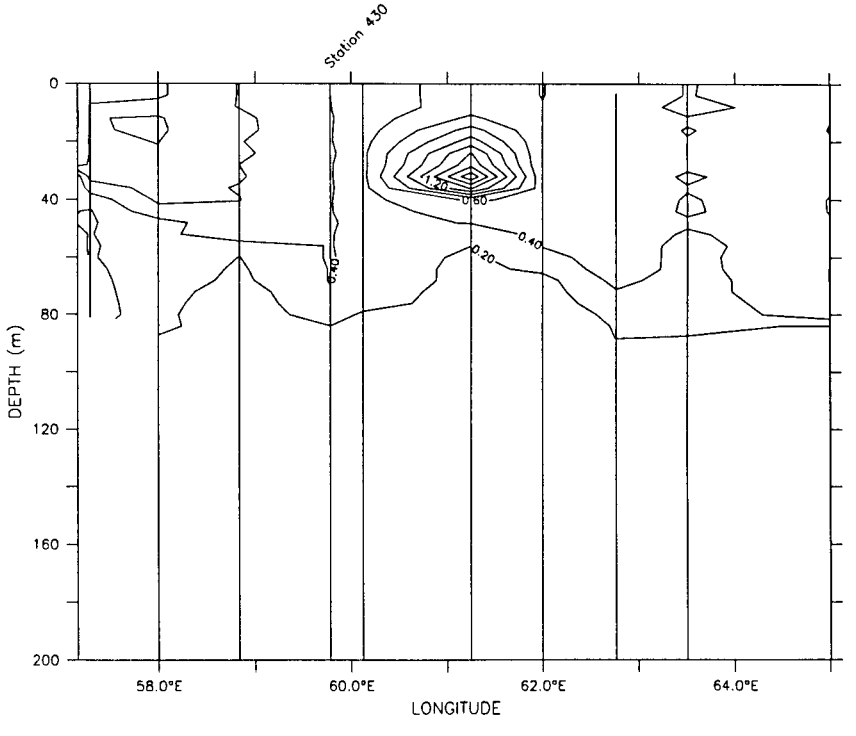

Figure 32: Vertical distribution of Chl *a* calculated from fluorescence from 14°N, 65°E towards Ras al Madraka, Oman, for the upper 200 m (cruise M32/5, section T2). Sample locations have been marked by lines. Unit is mg Chl *a* m^{-3}.

6.2 Model setup

The model setup is similar to that of the Northeastern North Atlantic in chapter 5. Alterations made to the model concern the physical forcing as given by light and mixed layer cycle. Light again is calculated according to Brock (1981) for the specific region (10°and 17°N for S15 and S04, respectively). Light is reduced by cloudiness following Reed (1976), which has been interpolated from monthly means for the specific region as given by the Esbensen-Kushnir climatological data set (as available through `ferret.wrc.noaa.gov/fbin/climate_server`,see figure 28). Diffusive exchange between the different layers is calculated according to Evans and Garçon (1997) using profiles for upper and lower boundary of the thermocline. Thermocline depth has been calculated from monthly mean temperature profiles as presented in the World Ocean Atlas (WOA, as available through `ferret.wrc.noaa.gov/fbin/climate_server`) using the criterion $\Delta T = 0.1°C$ and $\Delta T = 0.5°C$ for the location of the top and bottom thermocline, respectively. Mixed layer cycles for both stations according to this criterion, together with the mixed layer depths calculated by Codispoti (unpubl.) for 1995 cruises for five days, using a criterion of a .03kg m^{-3} change in density, are shown in figures 33 and 34 for stations S04 and S15, respectively. The WOA mixed layer depths match the depths that have been found in 1995 fairly well, although for S04 the climatology does not mix as deep as has been found in 1995. There is a large variation in estimated mixed layer depth during the day.

Station S15 exhibits a deepening of the mixed layer to about 80 m, which can be attributed to downwelling and/or erosion of the mixed layer due to the monsoonal forcing. The mixed layer depths in December and January as found in 1995 are slightly underestimated by the WOA data set. Nevertheless, the overall pattern is matched quite well by the WOA data.

The biological parameters are the same as in the previous chapter – the only alteration that is made is a rise in maximum phytoplankton growth rate μ_{PHY}, which in the simulations for the Arabian Sea has been set to a value of 2.5 d^{-1} due to higher temperature and to account for the very high rates of productivity that have been found in the Arabian Sea (v. Bröckel, unpubl; Barber, unpubl.) and even high carbon-specific growth rates (Barber, unpubl.). Again, in addition to the base run, experiments have been performed with the model for the different locations (increase in stickiness; simulation with a detrital model). The parameter values will be given in the respective description of the experiment.

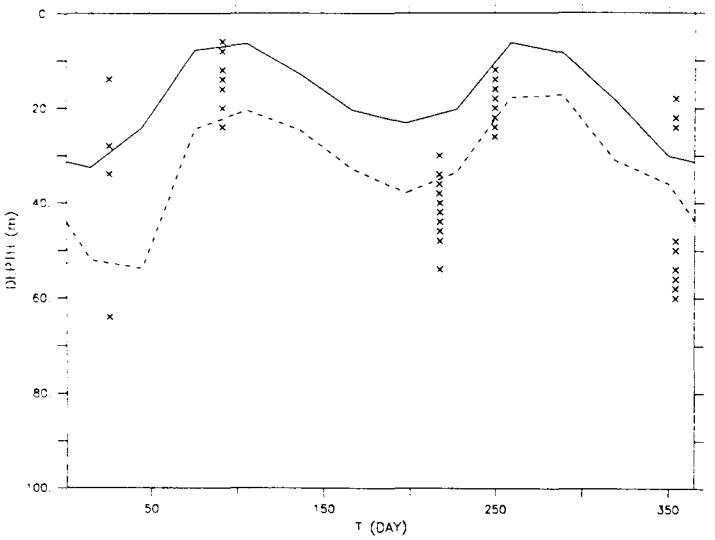

Figure 33: Annual mixed layer cycle climatology for S04, 17°N 60°E. Mixed layer depth calculated by L. Codispoti (unpubl.) for several CTD casts per day is shown by crosses.

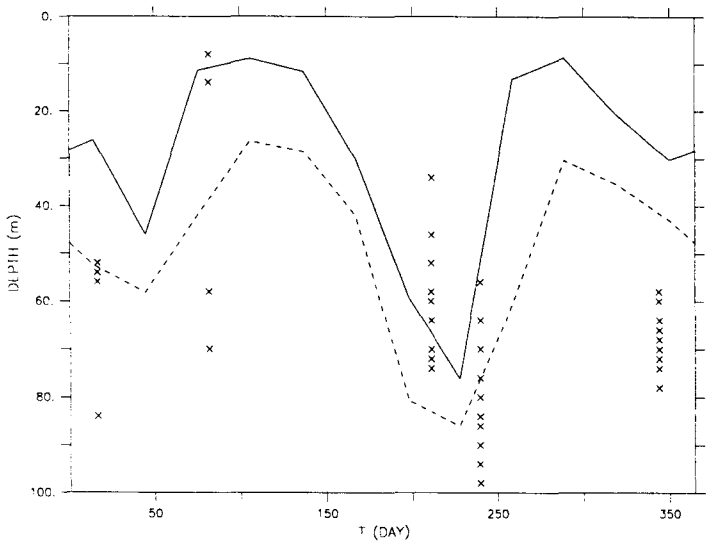

Figure 34: Annual mixed layer cycle climatology for S15, 10°N 65°E. Mixed layer depth calculated by L. Codispoti (unpubl.) for several CTD casts per day is shown by crosses.

The initial profiles for phytoplankton and nitrate have been taken from the profiles measured in January 1995 on the cruises of the American JGOFS process studies at the corresponding sites. All model results for station S15 presented in the next section show the results of the tenth year of simulation, i.e. the model has almost reached its equilibrium cycle. The same procedure has been used for the model simulations at station S04 relatively close to the Oman coast. Nevertheless, it will be shown that on this station a so-called

"climatological" (or "equilibrium") cycle of course cannot simulate the lateral influence of nutrient rich water coming from the coastal upwelling. In addition to the "base" run performed with this model and using a nine year spinup, three other simulations (base, increased stickiness and detrital model) have been performed, where in the tenth year of every simulation nutrients are entrained into the model during the time of the SWM by re-setting nutrient values to observed values. These model runs are then taken for comparison with the simulations performed for the other oceanic regions.

6.3 Simulations for Station S15 (10°N 65°E)

6.3.1 The Base Run

Figure 35 shows the annual cycle of nitrate, contoured vs. depth and time after a nine year spinup. Nitrate concentration is uniform over the year, with a low (< 1 mmol N m^{-3})

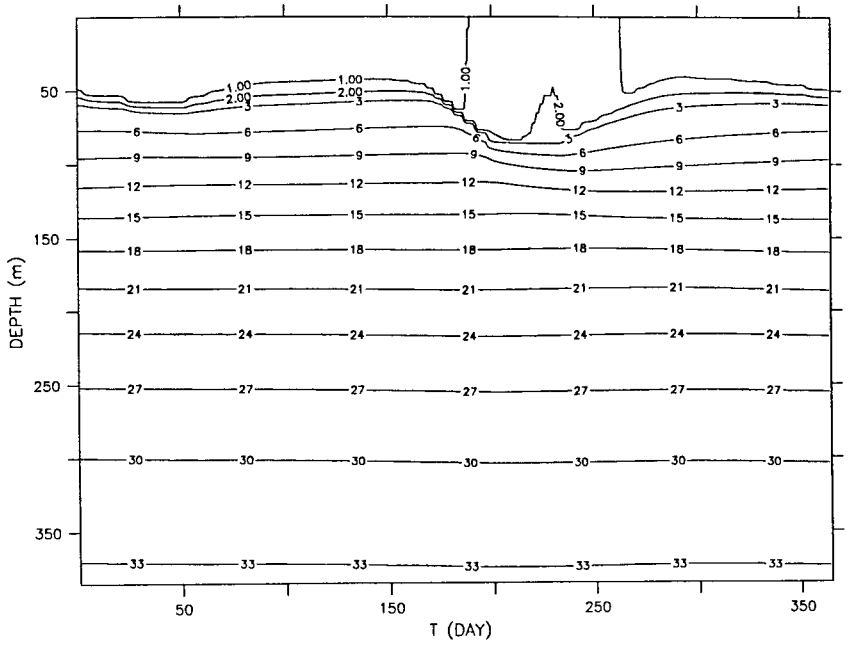

Figure 35: Nitrate for the base model at station S15 (upper 400 m). Nitrate is contoured by a thin line, units are mmol N m^{-3}.

concentration in the upper layers. When the mixed layer deepens in summer (and, to a lesser extent, in winter), the nitracline also deepens and nitrate is entrained into the mixed layer and nitrate values become as high as 1 mmol N m^{-3}.

Phytoplankton immediately assimilate these new nutrients. This leads to a small phytoplankton bloom (figure 36) with phytoplankton concentration increasing from 0.4 mmol N m^{-3} in early summer to more than 0.5 mmol N m^{-3}.

Prior to this bloom, during the spring intermonsoon phase, a DCM is established, which vanishes when phytoplankton increases in the mixed layer in June/July. Phytoplankton concentration and/or aggregation parameters are too low to allow the formation of large aggregates, so their concentration for the whole year is below 0.001 mmol N m^{-3} (and not shown in figure 36). The concentration of phytoplankton is more or less constant throughout the year, and even less than zooplankton concentration, which varies between 0.3 and 0.7 mmol N m^{-3} (figure 37). As there is little variation in phytoplankton concentration, sinking

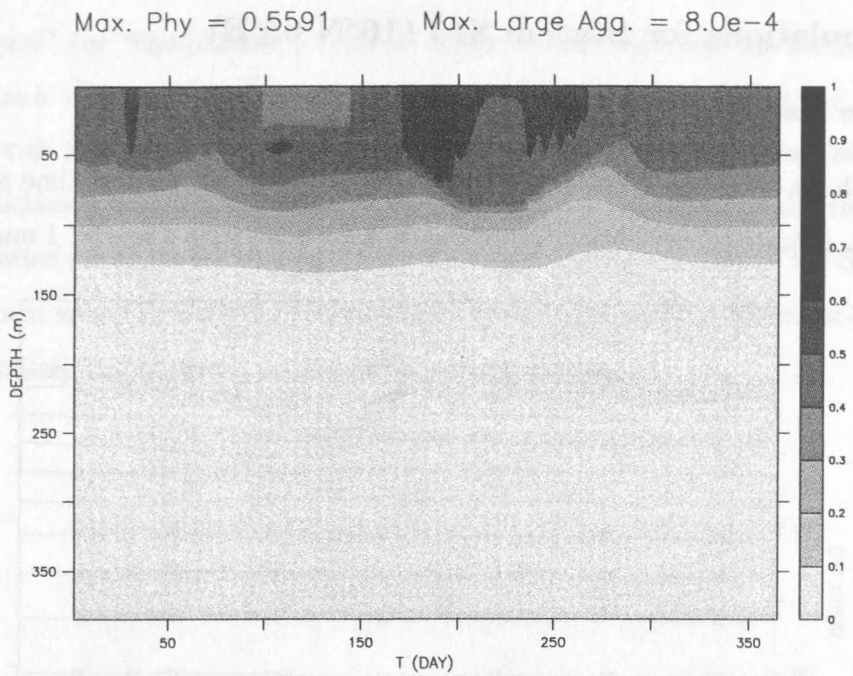

Figure 36: Mass of total phytoplankton for the base model simulation at station S15 (upper 400 m). Phytoplankton mass is shown by grey shades. Unit is mmol N m^{-3}.

speed stays quite constant throughout the year, with low values in the upper layers (< 10 m d^{-1}) and little variation at a depth of 400 m, where mass sinking speed only varies between 20 and 100 m d^{-1} (no figure). Similar to the other compartments, pellets too show little variation with depth and time, but mostly have relatively low values around 0–0.2 mmol N m^{-3} (figure 37).

The little variation in phytoplankton standing stock, phytoplankton mass sinking speed and fecal pellet standing stock, leads to little variations in shallow (400 m) and deep (800 m) flux, which is plotted in figure 38. The maxima in shallow and deep flux (0.8 and 0.2 mmol N m^{-2} d^{-1}) occur after the mixed layer deepening in summer, and consist mainly of fecal pellets. A lower and less pronounced peak can be detected in spring, following the mixed layer deepening during that time. Phytoplankton, once it has settled through 400 m almost immediately reaches 800 m - this is the reason why both lines for shallow and deep phytoplankton flux match almost exactly.

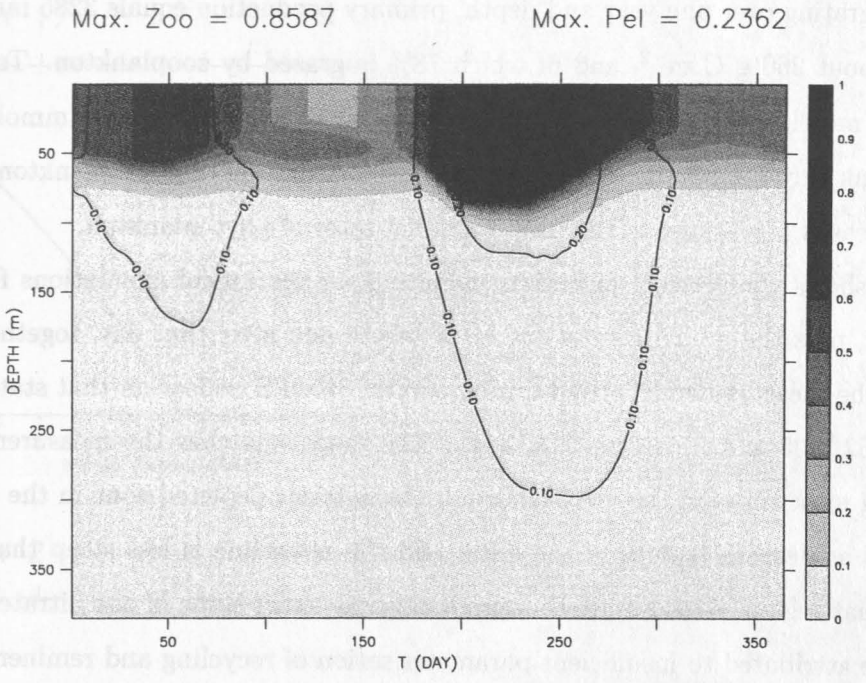

Figure 37: Zooplankton and fecal pellet concentration for the base model simulation at station S15 (upper 400 m). Zooplankton is shown by grey shades, fecal pellet concentration is contoured by a thin line, unit is mmol N m^{-3}.

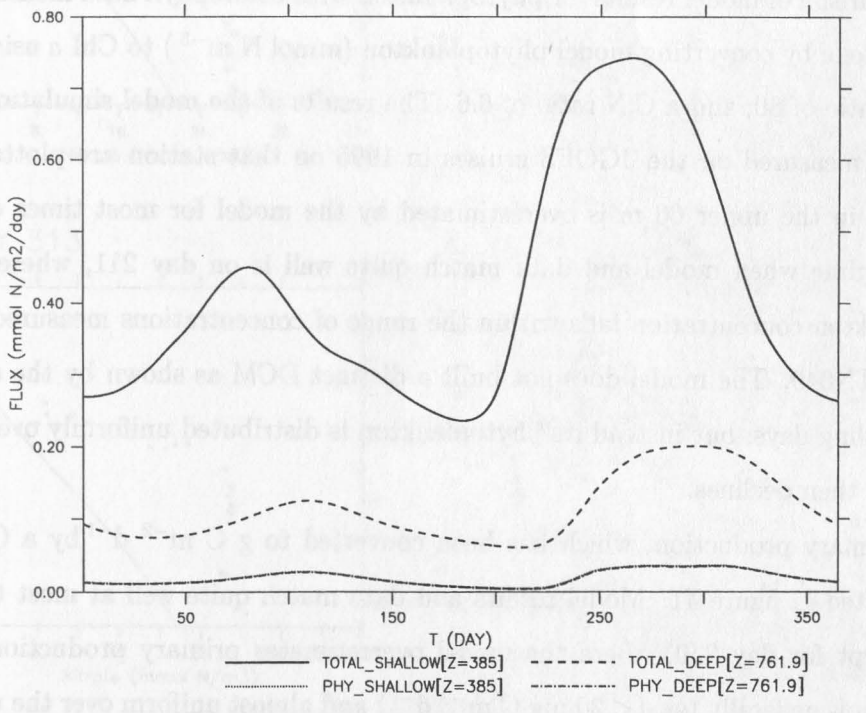

Figure 38: Sedimentation in 400 and 800 m for the base model simulation at station S15. Total flux through 400 and 800 m is denoted by solid and broken lines, respectively. Phytoplankton flux through 400 and 800 m is denoted by dotted and broken line with dots (see also figure legend, and text for further explanations). Units are mmol N m^{-2} d^{-1}.

When integrating over one year and depth, primary production equals 3285 mmol N m^{-2}, which is about 260 g C m^{-2}, and of which 78% is grazed by zooplankton. Total shallow flux is 153 mmol N m^{-2}, with little phytoplankton (5%). Only 27% (42 mmol N m^{-2}) of this flux sink through 800 m. In this depth, the contribution of phytoplankton to vertical flux is increased (16%) due to the higher sinking rates of phytoplankton.

Figure 39 shows the vertical profiles of nitrate from the model simulations for six days of the year, plus the model results one week before and after that day, together with the results of the measurements carried during several JGOFS cruises on that station in 1995 (days 17, 82, 205 and 211, 240, 313, 344). The model matches the measurements quite well during most times of the year, although the nutrient depleted zone in the model does not extend as deep as it does in the data, and the nutricline is less steep than has been found in that region. This failure in reproducing the exact slope of the nitrate profile can perhaps be attributed to insufficient parameterisation of recycling and remineralization of the different nitrogen components of the biological system, or to an insufficient mixing scheme or coefficient.

The comparison of model results for phytoplankton with chlorophyll data measured in 1995 has been done by converting model phytoplankton (mmol N m^{-3}) to Chl *a* using a carbon to Chl *a* ratio of 80, and a C:N ratio of 6.6. The results of the model simulations together with data measured on the JGOFS cruises in 1995 on that station are plotted in figure 40. Chl *a* in the upper 60 m is overestimated by the model for most times of the year. The only time when model and data match quite well is on day 211, where the model phytoplankton concentration falls within the range of concentrations measured on M32/5 and on TTN049. The model does not built a distinct DCM as shown by the data on the corresponding days, but instead its phytoplankton is distributed uniformly over the upper 70 m, and then declines.

Model primary production, which has been converted to g C m^{-2} d^{-1} by a C:N ratio of 6.6 is plotted in figure 41. Model results and data match quite well at most times of the year, except for day 240, where the model overestimates primary production. Primary production is generally low (< 20 mg C m^{-3} d^{-1}) and almost uniform over the upper 60 m, except when the mixed layer deepens in summer, where nitrate is entrained and enhances primary production especially in the upper well-lit layers.

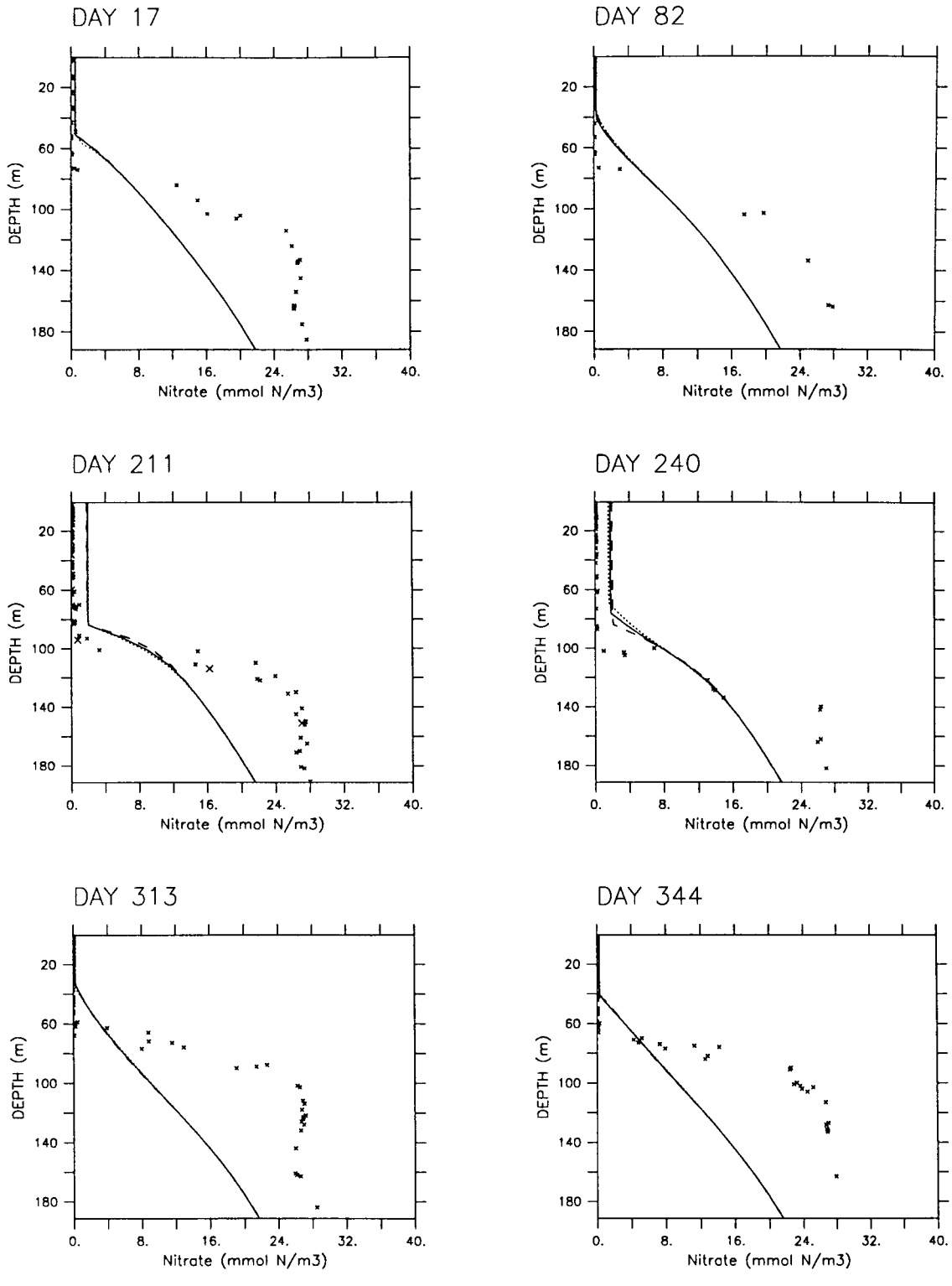

Figure 39: Vertical profiles for nitrate for the base model simulation at station S15 (upper 200 m), plus local measurements. Model profiles are displayed by a line for days 17, 82, 211, 240, 313 and 344, and profiles for seven days before and after the corresponding day are displayed by broken and dotted lines, respectively. Measurements made on the US JGOFS cruises (L. Codispoti) are displayed by crosses. Measurements made on METEOR M32/5 are denoted by large crosses (day 205, shown in mid left panel). Unit is mmol N m^{-3}.

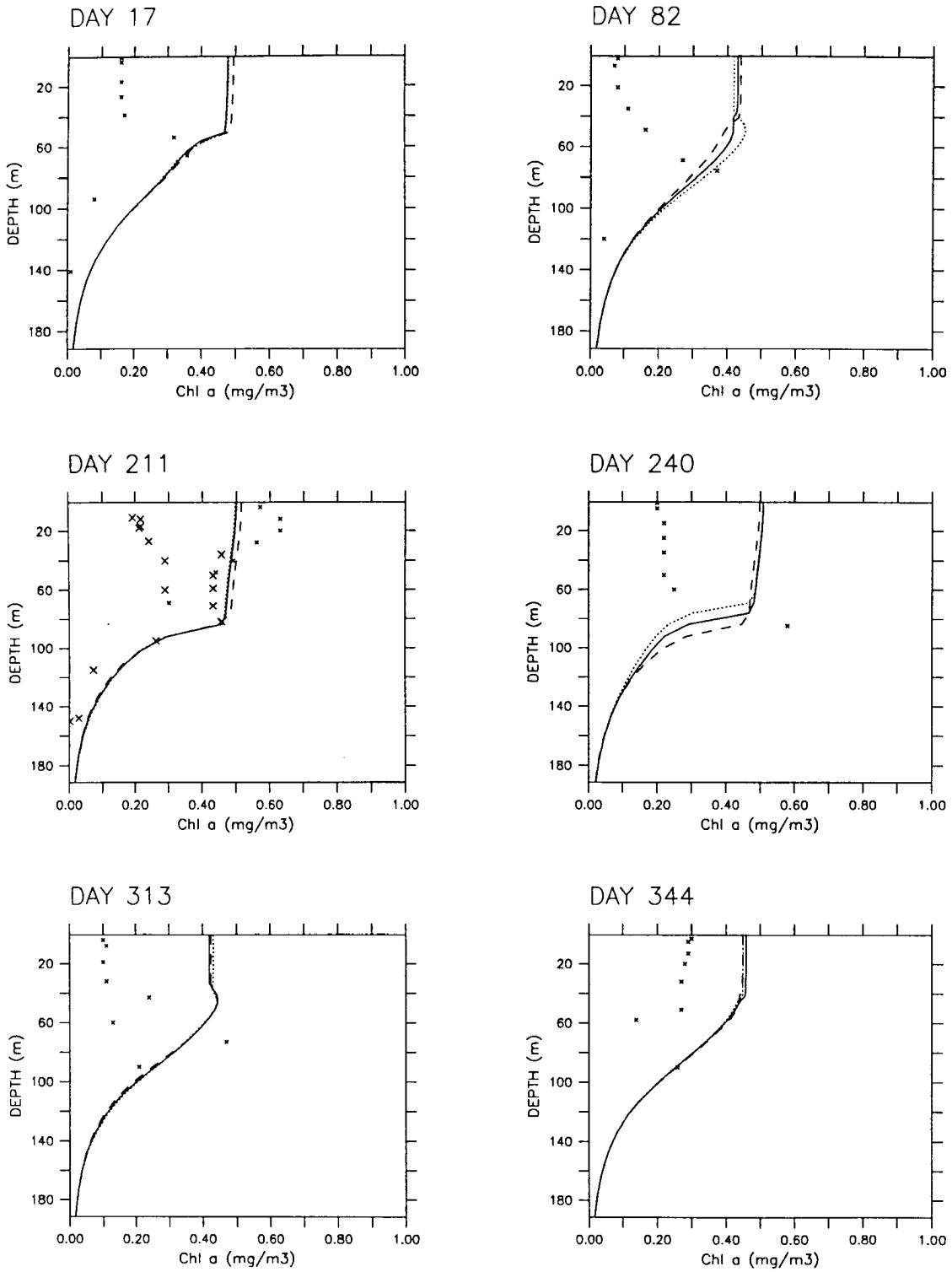

Figure 40: Vertical profiles for Chl *a* for the base model simulation at station S15 (upper 200 m), plus local measurements. Model profiles are displayed by a line for days 26, 92, 218, 250, 319 and 354, and profiles for seven days before and after the corresponding day are displayed by broken and dotted lines, respectively. Measurements made on the US JGOFS cruises (R. Barber) are displayed by crosses. Measurements made on METEOR M32/5 are denoted by large crosses (day 213, shown in mid left panel). Unit is mg Chl *a* m^{-3}.

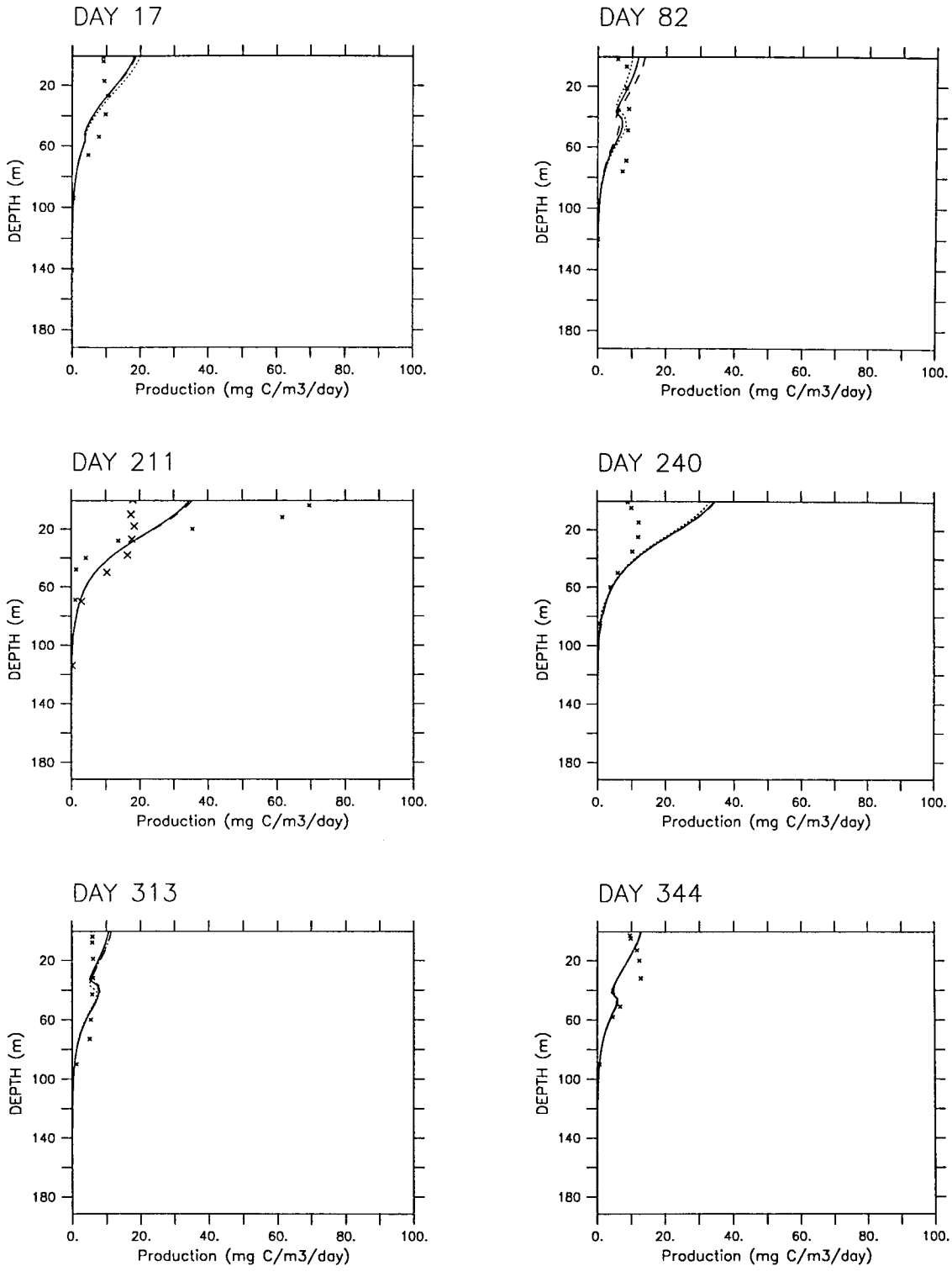

Figure 41: Vertical profiles for primary production for the base model simulation at station S15 E, plus local measurements. Model profiles are displayed by a line for days 26, 92, 218, 250, 319 and 354, and profiles for seven days before and after the corresponding day are displayed by broken and dotted lines, respectively. Measurements made on the US JGOFS cruises (R. Barber) are displayed by crosses. Measurements made on METEOR M32/5 are denoted by large crosses (day 213, shown in mid left panel). Units are g C m^{-2} d^{-1}.

6.3.2 Scenario "Sticky"

Doubling the stickiness of phytoplankton has almost no effect on the concentration of phytoplankton: the overall pattern of the annual cycle for this compartment, as presented in figure 42 is almost the same as in the base run, as well as the maximum concentration of about 0.6 mmol N m^{-3}. Due to the increased stickiness of the algae is this scenario, large aggregates reach a concentration of more than 0.006 mmol N m^{-3}, while maximum zooplankton in this scenario with 0.8 mmol N m^{-3} are about the same as in the previous one (no figure).

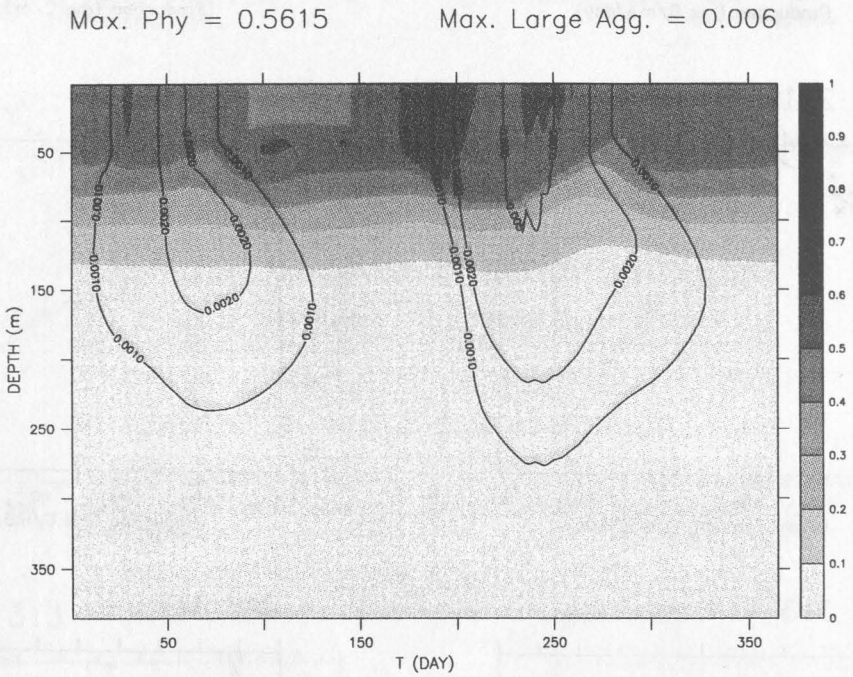

Figure 42: Mass of total phytoplankton and aggregates sinking faster than 10 m d^{-1} (minimum diameter $\approx$ 200 μm) for the "Sticky" scenario at station S15 (upper 400 m). Phytoplankton mass is shown by grey shades, mass of aggregates sinking faster than 10 m d^{-1} is shown by contour lines on semilogarithmic intervals. Unit is mmol N m^{-3}.

Consequently, a larger difference between the runs can be found in the annual cycle of average mass sinking speed, showing a higher temporal variation, with an increase to more than 400 m d^{-1} at 400 m depth. This is of some importance for the sedimentation as presented in figure 43. Although the maximum flux is only slightly increased (ca. 0.9 mmol N m^{-2} d^{-1} in the shallow, 0.3 in the deep depth), the phytoplankton in this simulation makes up more than 50% of the peak flux. Almost all of the phytoplankton settling through 400 m finally sink out of the bottom of the model water column (both lines for shallow and

deep phytoplankton flux match almost exactly).

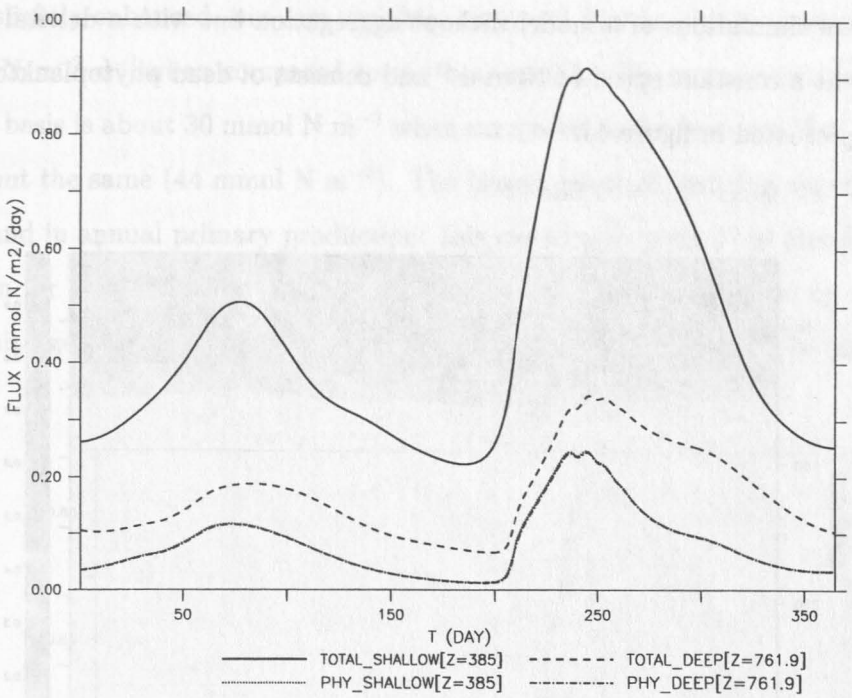

Figure 43: Sedimentation in 400 and 800 m for the model simulation with increased stickiness at station S15. For notations and units see figure 38.

Annual primary production is less than it is in the base run (3098 mmol N m^{-2}), but almost the same fraction as in the base run is grazed (76%). Shallow flux in this model is only slightly enhanced (165 mmol N m^{-2}), but phytoplankton contributes a larger amount to this flux (19%). The largest effect of changing phytoplankton stickiness is on deep flux, which is increased by more than half of that of the base run (62 mmol N m^{-2}), with phytoplankton contribution being three times as high as in the base run (49%, see also table 8 in the last chapter for comparison with other simulations). The comparison of model results with data shows almost the same pattern as in the base run, so the results are not presented here. The model overestimates chlorophyll for most times of the year, but shows a very good reproduction of the vertical profiles of primary production. The little variation between both the base run and the "Sticky" scenario can be attributed to the small role aggregation plays at a site with very low phytoplankton densities during the year.

6.3.3 The "Detritus" Scenario

The results of simulations of a model without aggregation but with a detrital model pool which sinks at a constant speed of 10 m d^{-1} and consists of dead phytoplankton and fecal pellets are presented in figure 44.

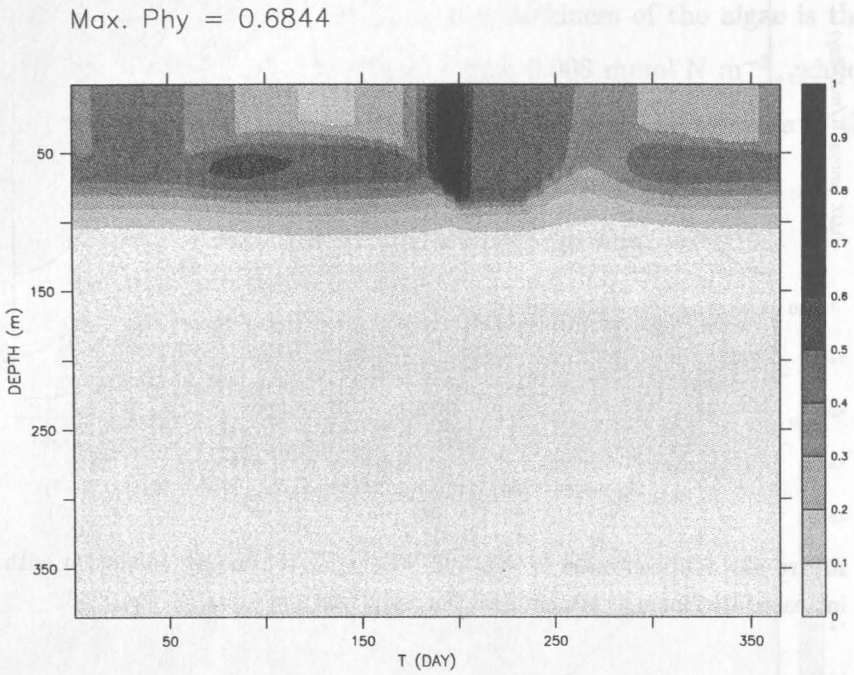

Figure 44: Mass of total phytoplankton for the "Detritus" scenario at station S15 (upper 400 m). Phytoplankton mass is shown by grey shades. Unit is mmol N m^{-3}.

In the spring intermonsoon in this model the DCM is more pronounced, and there is also a more distinct surface bloom following the mixed layer deepening in summer, reaching a phytoplankton concentration of 0.7 mmol N m^{-3}. In this model the zooplankton annual cycle is less pronounced that in the base run, with lower a maximum concentration ($<$ 0.5 mmol N m^{-3}). The reason for this behaviour of the model can be found in the loss from phytoplankton to the detrital pool, which in this model is assumed to be unpalatable for zooplankton. In the base run, aggregation played little role and phytoplankton had a comparatively long residence time in the mixed layer, where zooplankton could graze on it. In the detrital model, phytoplankton is lost to zooplankton grazing once it has died and entered the detrital pool. Further, phytoplankton mortality increases the detrital pool, and this mass is finally lost to the system, with a constant sinking speed throughout the year. As has been shown in the base model simulation phytoplankton mass sinking speed in the upper layers are always below 10 m d^{-1}, so having a detrital sinking speed of 10 m

d^{-1} enhances at least shallow flux (figure 45). Thus shallow flux during the intermonsoon period is slightly enhanced, but less variable, and peak flux as well is increased by about 0.2 mmol N m^{-2} d^{-1} when compared to the base model. The increase in shallow flux on an annual basis is about 30 mmol N m^{-2} when compared to the base run, but annual deep flux is about the same (44 mmol N m^{-2}). The largest effect of omitting aggregation at all can be found in annual primary production: this model only gives 1310 mmol N m^{-2} y^{-1}. The reason for this decrease in annual production can also be explained by the different pathway nitrogen takes in this model (see above), which also explaines the higher shallow flux.

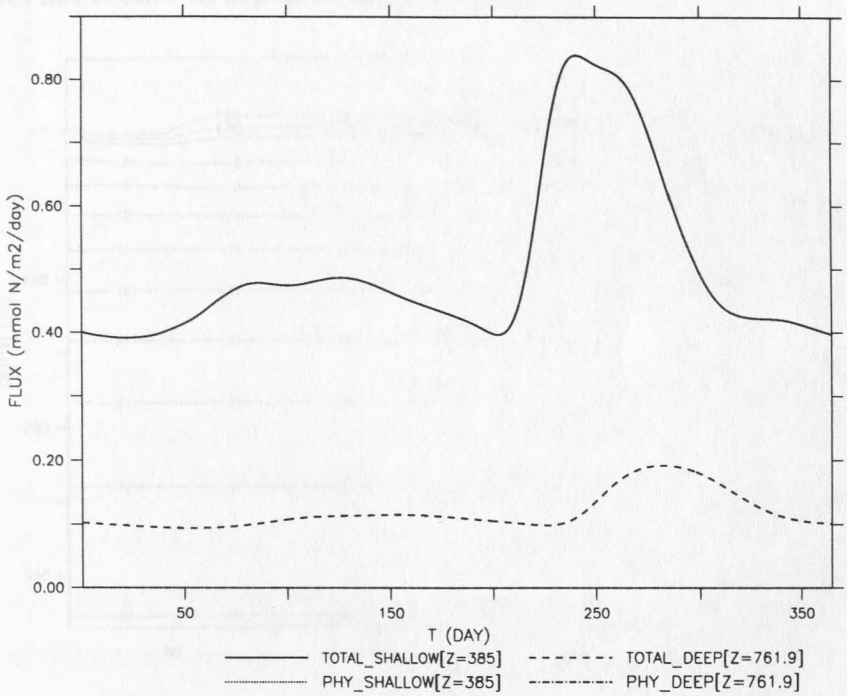

Figure 45: Sedimentation in 400 and 800 m for the model simulation with the detritus model at 10°N, 65°E. For notations and units see figure 38. For further explanations see text.

The comparison of model phytoplankton and Chl *a* as measured during various cruises in 1995 (no figure) shows that although this model, like the base model, has a tendency to overestimate Chl *a* concentrations, it is in better agreement with the data, and even shows a DCM at a depth of about 60 m. Unfortunately, the detritus model fails to reproduce the vertical profiles of primary production. Except for day 240, the model primary production is much less than what has been found in nature. Model results on day 211 match the results of the measurement of M32/5, 6 days earlier – but the model primary production never increases to values as have been found on TTN049. Maximum phytosynthesis produced by

the model is 24 mg C m^{-3} d^{-1}.

6.4 Simulations for Station S04 (17°N 60°E)

6.4.1 The base run with climatological forcing

Figure 46 shows the annual cycle of nitrate, contoured vs. depth and time for the tenth year of simulation. When the mixed layer deepens in in late winter and spring due to the NEM forcing (max. depth 54 m on day 45), little nitrate is mixed from deeper layers into the surface, up to maximum values of < 1 mmol N m^{-3} in at 1 m depth. There is almost no increase in surface nitrate concentration during the SWM because mixing depth according to the criteria that have been described in the the model setup is even less during that time, and does not extend to depths as deep as in winter.

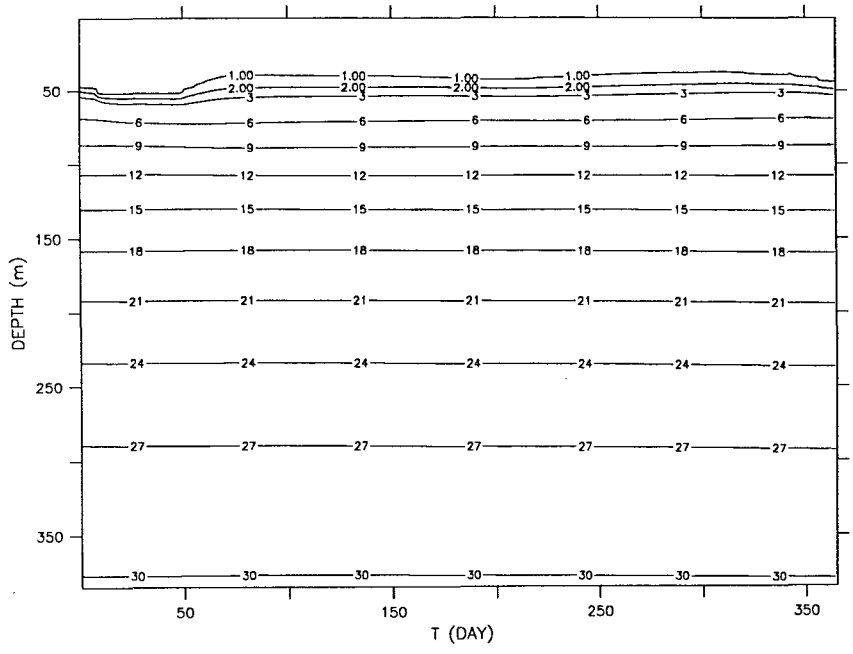

Figure 46: Nitrate for the base model at station S04 (upper 400 m). Nitrate is contoured by a thin line, unit is mmol N m^{-3}.

Phytoplankton respond to the deeper mixing during the NEM with only slightly elevated concentration up to a maximum of 0.5 mmol N m^{-3} on day 19 (figure 47). During the intermonsoon phase in the first half of the year, a deep chlorophyll maximum (DCM) is built below the thermocline, where nitrate allows phytoplankton growth at greater depths despite its low concentration in the mixed layer. When the mixed layer deepens slightly in July due to the SWM forcing, the small nutrient increase in the surface waters is followed by only slightly elevated phytoplankton concentration in the mixed layer. Still a DCM persists and lasts during the second intermonsoon phase until the mixed layer starts to deepen again

in winter. Phytoplankton concentration even during the NEM, but especially during the SWM, is far too low to allow for rapid aggregation and formation of large aggregates. Sinking speed is almost constant throughout the annual cycle, with a moderate increase of sinking rates following the NEM.

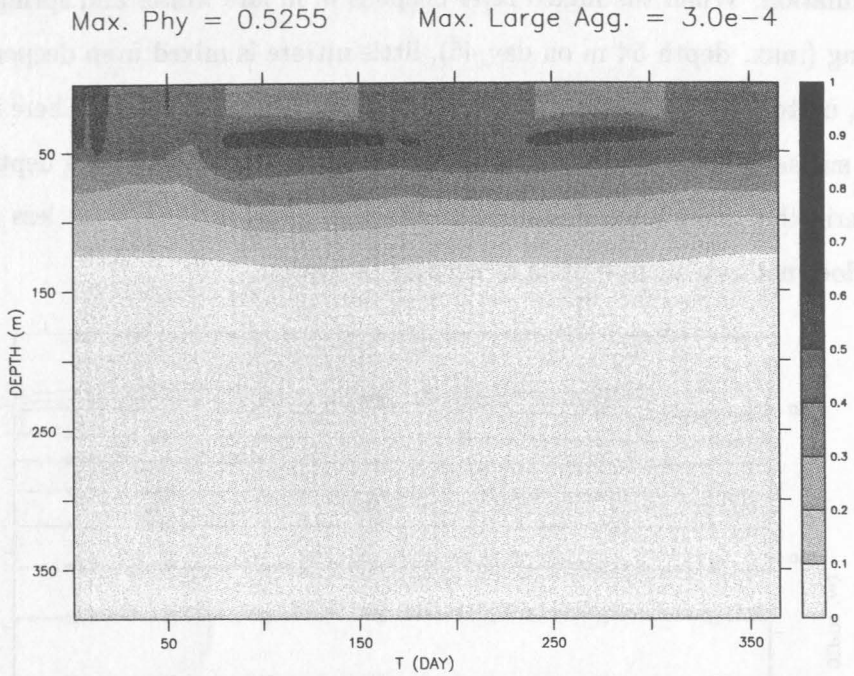

Figure 47: Mass of total phytoplankton for the base model simulation at station S04 (upper 400 m). Phytoplankton mass is shown by grey shades. Unit is mmol N m^{-3}.

Due to the small variations in either phytoplankton and zooplankton, of course flux at 400 and 800 m depth in the model simulation is low, with a maximum of about 0.5 mmol N m^{-2} d^{-1} occuring after the NEM (figure 48). Almost all of the flux can be attributed to fecal pellets, and about 30% of the shallow flux settles through 800 m. Yet all of the phytoplankton reaching the 400 m depth horizon finally settles out of the model domain.

Figure 49 shows the vertical profiles of nitrate from the model simulations for six days, plus the model results one week before and after that day, of the year together with the measurements carried during several JGOFS cruises on that station in 1995. The model matches the measurements quite well during the NEM and intermonsoon seasons (days 26, 92, 319, 354) but strongly underestimates the high nutrient concentration especially during the SWM (days 218, 213, 219 and 250). Model phytoplankton, which is computed in units of nitrogen, has been converted to Chl *a* by using a carbon to Chl *a* ratio of 80, and a C:N ratio of 6.6. The results of the model simulations together with data measured on the

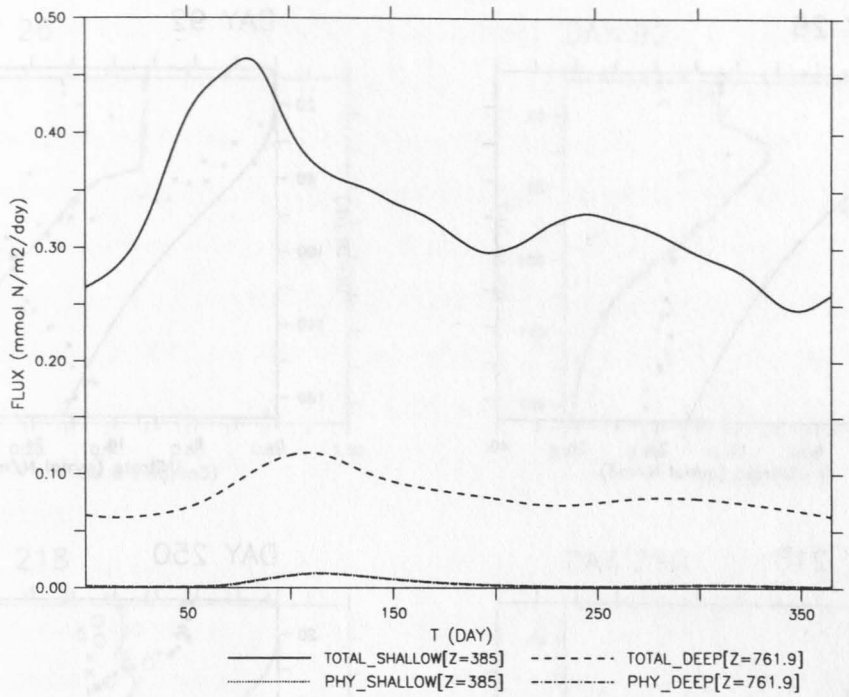

Figure 48: Sedimentation in 400 and 800 m for the base model simulation at station S04. Total flux through 400 and 800 m is denoted by solid and broken lines, respectively. Phytoplankton flux through 400 and 800 m is denoted by dotted and broken line with dots (see text for further explanations). Unit is mmol N m^{-2} d^{-1}.

JGOFS cruises in 1995 on that station are plotted in figure 50. Chl *a* data are reproduced by the model very well on most times of the year, with an underestimate for days 92 and 250. The DCM on day 92 produced by the model is not as pronounced as has been found in the data. On day 250, maximum Chl *a* in the model is only half of the value that has been found by fluorometric measurements. The decline of Chl *a* in the model with depth is not as pronounced as has been found in the measurements. Model primary production, converted to g C m^{-2} d^{-1} by a C:N ratio of 6.6, is plotted in figure 51.

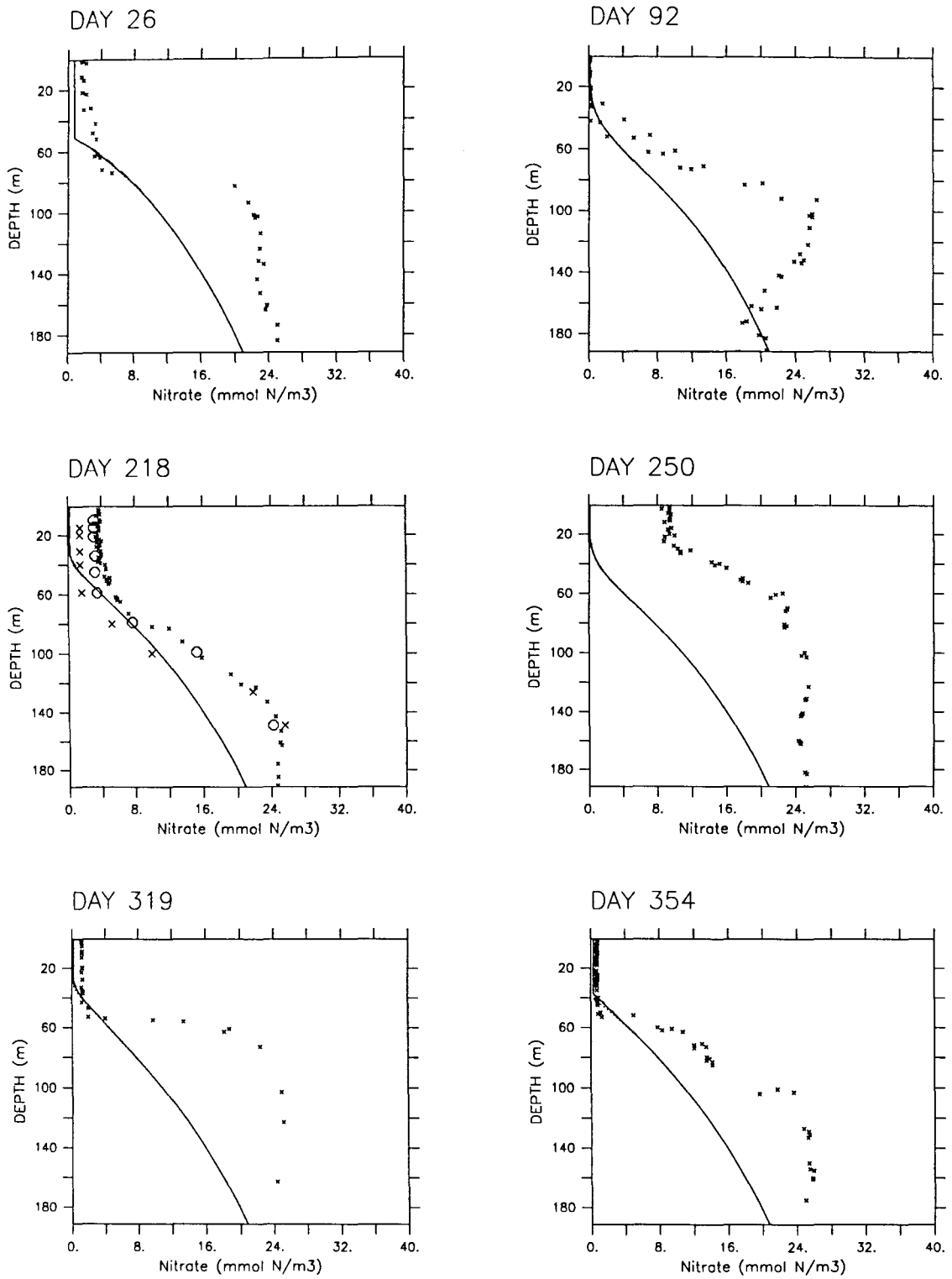

Figure 49: Vertical profiles for nitrate for the base model simulation at station S04 (upper 200 m), plus local measurements. Model profiles are displayed by a line for days 26, 92, 218, 250, 319, and profiles for seven days before and after the corresponding day are displayed by broken and dotted lines, respectively. Measurements made on the US JGOFS cruises (L. Codispotiy) are displayed by crosses. Measurements made during METEOR M32/5 are denoted by large crosses and by large circles (day 213 and 219, respectively, shown in mid left panel). Unit is mmol N m^{-3}.

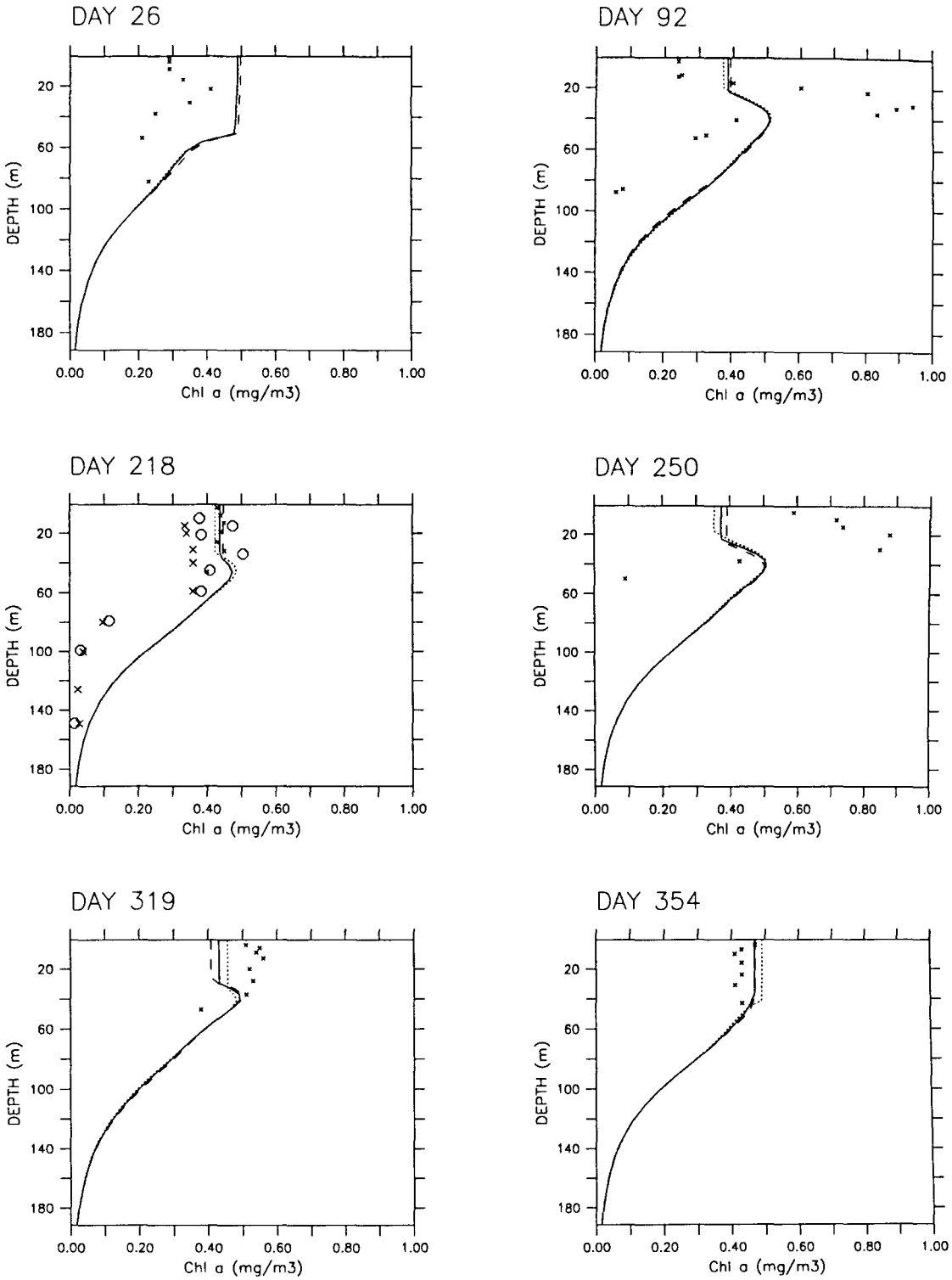

Figure 50: Vertical profiles for Chl *a* for the base model simulation at station S04, plus local measurements. Model profiles are displayed by a line for days 26, 92, 218, 250, 319 and 354, while profiles for seven days before and after the corresponding day are displayed by broken and a dotted lines, respectively. Measurements made on the US JGOFS cruises (R. Barber) are displayed by crosses. Measurements made during METEOR M32/5 are denoted by large crosses and by large circles (day 213 and 219, respectively, shown in mid left panel). Unit is mg Chl *a* m^{-3}.

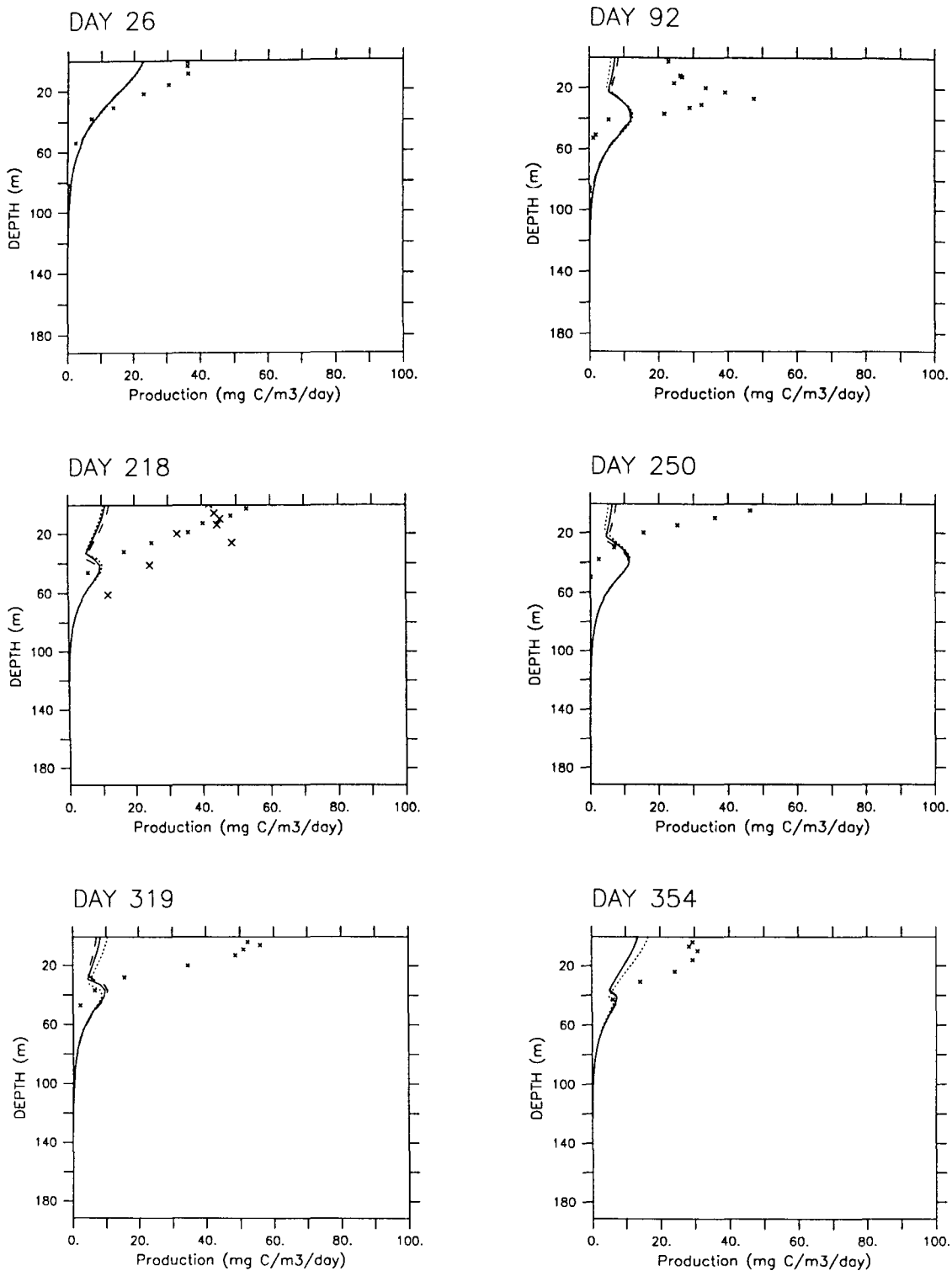

Figure 51: Vertical profiles for primary production for the base model simulation at station S04 (upper 200 m), plus local measurements. Model profiles are displayed by a line for days 26, 92, 218, 250, 319 and 354, and profiles for seven days before and after the corresponding day are displayed by broken and dotted lines, respectively. Measurements made on the US JGOFS cruises (R. Barber) are displayed by crosses. Measurements made during METEOR M32/5 are denoted by large crosses (day 213, shown in mid left panel). Unit is g C m^{-2} d^{-1}.

The model exhibits no good reproduction of primary production as measured by means of labeled ^{14}C uptake on different cruises, with a strong underestimation especially in the upper layers. This can be attributed to the nutrient depletion in the model mixed layer, which is unlikely to occur in reality at least during both monsoonal phases. Integrated primary production over the tenth year of the simulation is 2734 mmol N m^{-2}, which is about 217 g C m^{-2}. Of this, 75% is eaten by model zooplankton, and 10 and 2% of this sinks through 400 and 800 m, respectively. The percentage of phytoplankton of total sedimentation is only 1 and 5% for both depths, which is the lowest contribution of phytoplankton to sedimentation which has been achieved so far in the aggregation runs presented in this work.

The results from the base run exhibit a good agreement with data for the intermonsoonal phases, and underestimation of surface nitrate during the SWM and an overestimate for the NEM. Despite the fact that nitrate during these two seasons is not reproduced well by the model, nevertheless the phytoplankton concentrations both in the model and in the data agree quite well. What is more astonishing is the fact that although model and data give quite low phytoplankton concentrations especially during the SWM, the high opal and also PON of the trap data during the SWM indicate that there must have been a phytoplankton bloom in the upper layers before. Questions that need to be addressed are:

1. What controls the nitrate supply to the upper layers?

2. Where or when is the phytoplankton bloom that is necessary to explain these high fluxes of nitrogen and biogenic silica to the ocean interior?

There are at least four explanations for the problem addressed in the first question: 1.) Either the mixing and the mixed layer cycle of the model has been parameterized badly. Barkmann (pers. comm) has tested different parameterizations for mixing in a vertically resolved model run at 47°N 20°W and found that the mixing algorithm, which has been proposed by Evans and Garçon (1997), and is used in this model, agreed well with what he found when using a "turbulent closure" model with vertical profiles of diffusion coefficients provided by a three dimensional model output (Oschlies, unpubl.). Because the model thermocline as given by the World Oceanographic Atlas using the criteria for evaluation of the thermocline depth as given in the model description agrees quite well with what has been calculated by Lou Codispoti for the 1995 cruises, it seems unlikely that it is this

parameterization which leads to insufficient nutrient supply. 2.) The second explanation might be given by an insufficient mixing rate below the thermocline. Still the upper nutrient concentration is unlikely to be affected by an even higher deep mixing rate, as this would even more increase the surface nitrate values during the NEM, where the model matches the nitrate quite well. 3.) Another reason for the large discrepancy between model results and data can be seen in the model neglecting the phenomenon of the so-called open ocean upwelling. This type of upwelling, which occurs during the SWM due to negative wind stress curl on the ocean surface has been hypothesized by Brock (1992) for this specific region. Nevertheless, there has been little evidence for open ocean upweling to occur in 1995 (Waniek, pes. comm; Morrison *et al.*, in press.) 4.) The high nutrient concentrations in August and September 1995 were attributed to the influence of water masses formed by coastal upwelling and advected southeastwards (Morrison *et al.*, 1998; Banse, 1987). This would lead to an increase in nutrient concentration, which cannot be accounted for in a 1-dimensional model, but would need to take advantage for example of the output of a 3-dimensional model of ocean circulation. This type of modeling is beyond the scope of this work. Instead, as a way of simulating the response of phytoplankton to the input of nutrients during the SWM, a model run has been performed in which in the tenth year of the base model simulation a nitrate intrusion on day 218 is simulated by assimilating the nitrate profile of the US JGOFS cruise TT050 for this particular station into the model by using the maximum of the interpolated empirical nitrate value and the model nitrate on this day.

6.4.2 The base run with nitrate intrusion

When simulating a nitrate intrusion on day 218 by assimilating the nitrate profile measured on cruise TTN050, total nitrate input for the mixed layer for this day (depth of lower thermocline is 35 m) equals 121 mmol N, and 1020 mmol N for the whole water column. The development of phytoplankton for the upper 100 m is shown in figure 52.

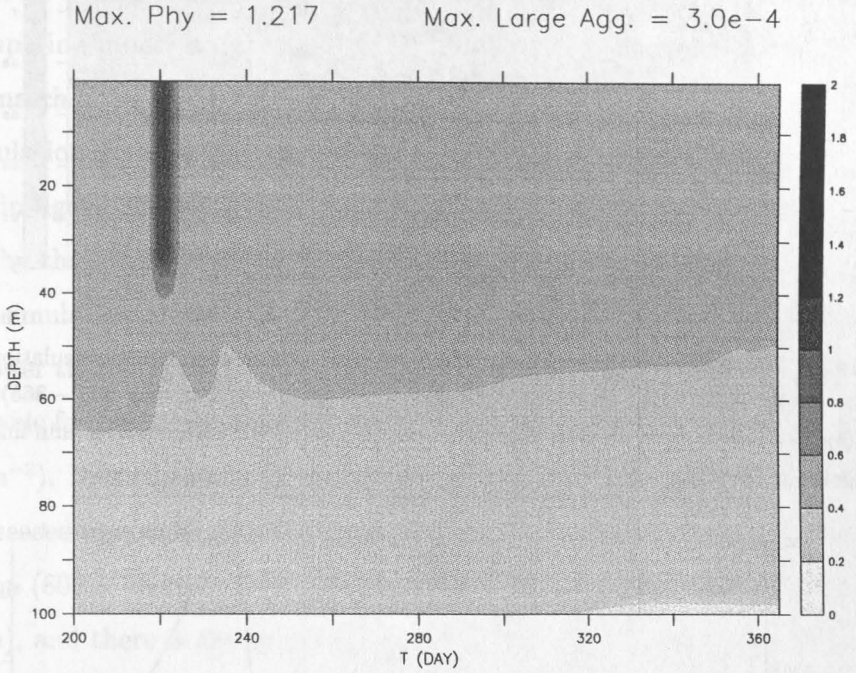

Figure 52: Mass of total phytoplankton for the base model simulation with nitrate profile assimilation on day 218 at station S04 (upper 100 m, day 200 – 365). Phytoplankton mass is shown by grey shades. Unit is mmol N m^{-3}.

Following the intrusion on day 218, phytoplankton starts to grow in the upper 40 m, until it reaches a maximum concentration of 1.2 mmol N m^{-3}. This increase in phytoplankton is immediately followed by an increase in zooplankton concentration. There is a very low concentration of large aggregates (less than 0.001 mmol N m^{-3}), because model zooplankton graze heavily on phytoplankton, and zooplankton reach even a higher maximum concentration than phytoplankton (< 1.7 mmol N m^{-3}, figure 53). Phytoplankton do not reach sufficient concentration for aggregation to play an important role.

As a consequence, both shallow and deep flux only increase slightly following the phytoplankton bloom, and most of the flux in both depths can be attributed to pellet sedimentation (figure 54).

When comparing the simulated nitrate profiles for six days with the observed nitrate profile,

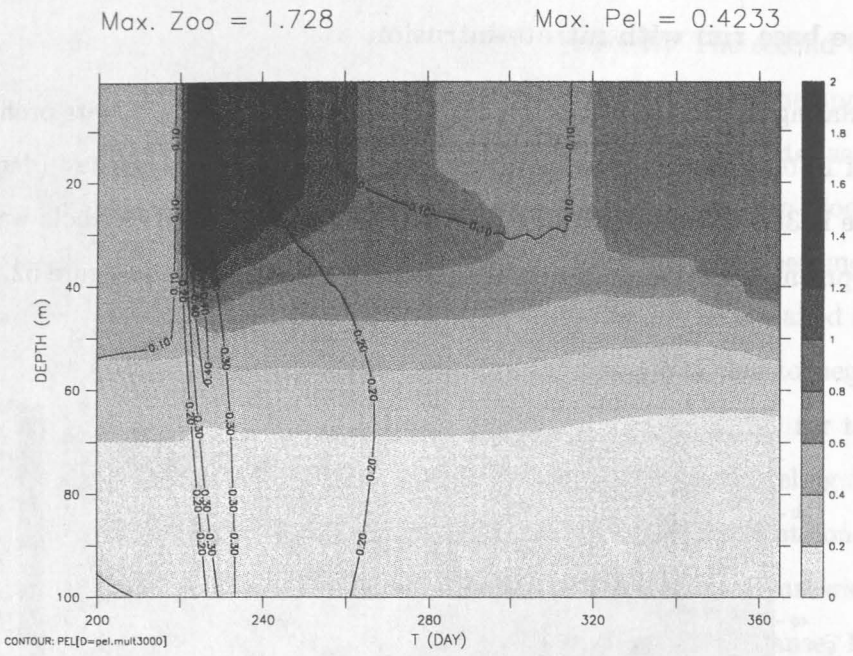

Figure 53: Zooplankton and fecal pellet concentration for the base model simulation with nitrate profile assimilation on day 218 at station S04 (upper 100 m, day 200 – 365). Zooplankton is shown by grey shades, fecal pellet concentration is contoured by a thin line, unit is mmol N m^{-3}.

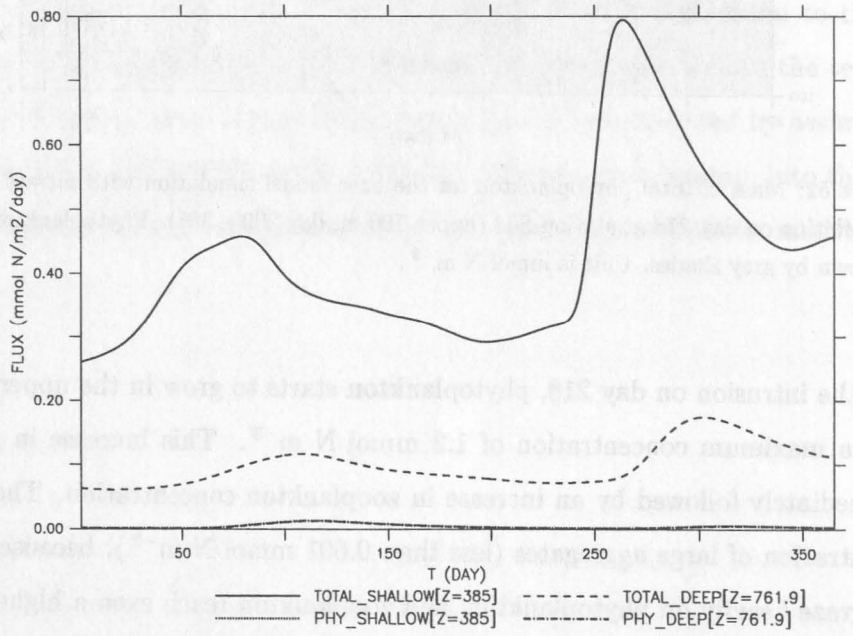

Figure 54: Sedimentation in 400 and 800 m for the base model simulation at station S04 with nitrate profile assimilation on day 218. For notations and unit see figure 48.

clearly it can be seen that due to the phytoplankton bloom following the nitrate intrusion, all of the nitrate that has been entrained is used by the model phytoplankton (figure 55). Model nitrate shows lower concentrations on day 250 than observed – most likely the observed high nitrate concentrations in the mixed layer can probably be attributed to further advection of nutrient rich water water from coastal areas, which is not implemented into the model for this time.

When comparing model phytoplankton with the observed data for Chl *a*, model results and data match quite well on most days of the year, although the DCM on day 92 in the model simulation is not as pronounced as in 1995 data (figure 56).

As shown in figure 57, the primary production in the first half of the year is still underestimated by the model, but for the time period following the nitrate profile assimilation the model simulation shows a good fit to the data. On day 250, primary production in the model is lower than observed. Integrated over one year, of course due to the increase in nitrate available for phytoplankton the primary production is larger than in the previous run (275 g C m^{-2}). Nevertheless, this increase in primary production does not enhance export due to increased aggregation; mostly the production by phytoplankton is being grazed by zooplankton (80%). Shallow flux is only slightly enhanced (12 g C m^{-2}, or 4% of primary production), and there is almost no change in deep flux (3 g C m^{-2}, or 1% of annual primary production). The contribution of phytoplankton to shallow flux is the same as in the previous run (1%), and its contribution to deep flux is even less (4%). This model type using this parameterization at this station strongly promotes zooplankton. Surplus nitrate is completely taken up by phytoplankton, but shortly after the onset of the SWM bloom the phytoplankton in this model is grazed by zooplankton, and its production is almost completely shifted to the zooplankton compartment. In this model, phytoplankton growth and aggregation cannot escape zooplankton grazing during the SWM.

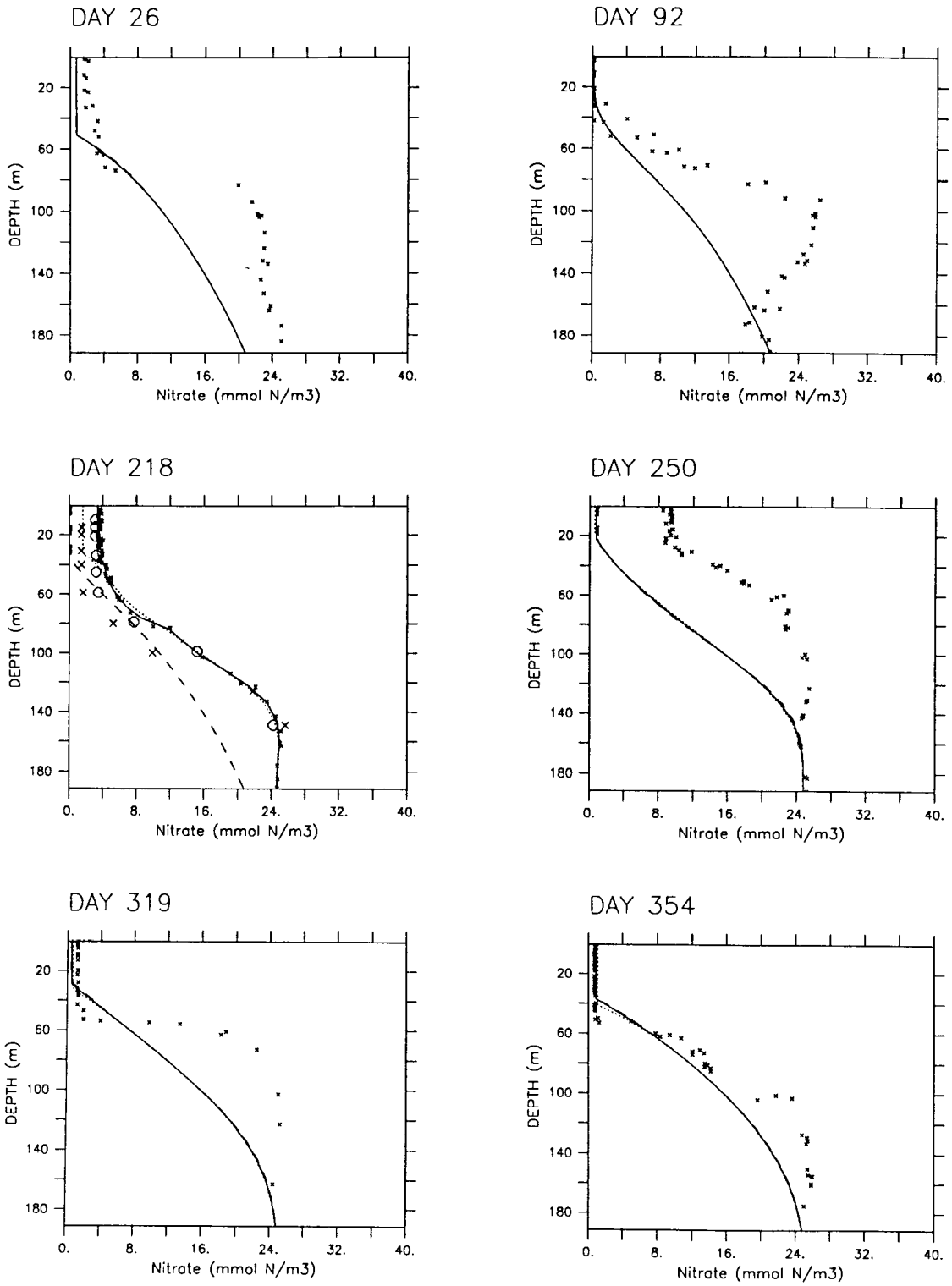

Figure 55: Vertical profiles for nitrate for the base model simulation with nitrate profile assimilation on day 218, at station S04 (upper 200 m), plus local measurements. For notations and unit see figure 49

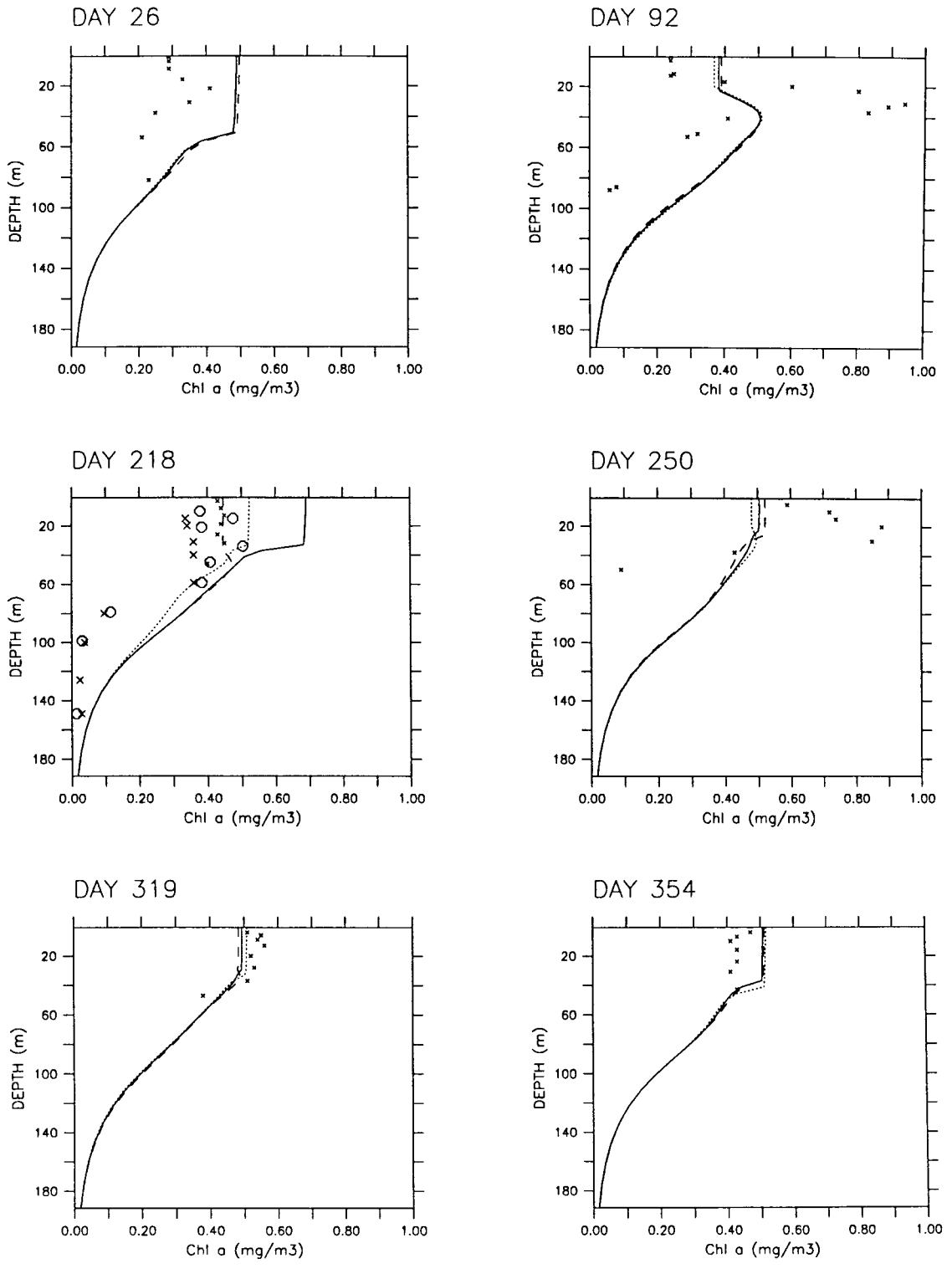

Figure 56: Vertical profiles for Chl *a* for the base model simulation with nitrate profile assimilation on day 218 at station S04 (upper 200 m), plus local measurements. For notations and unit see figure 50.

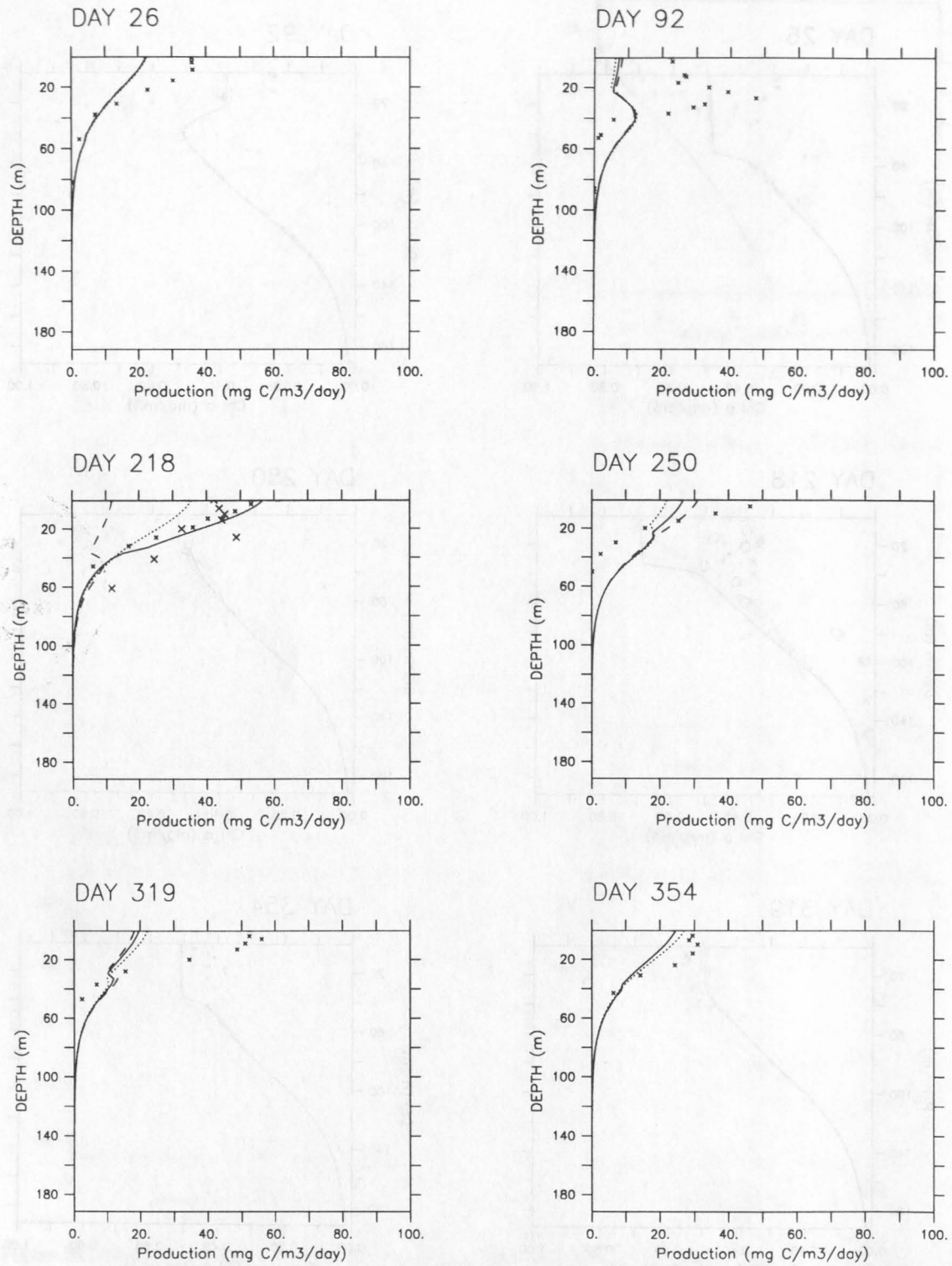

Figure 57: Vertical profiles for primary production for the base model simulation with nitrate profile assimilation on day 218 at station S04 (upper 200 m), plus local measurements. For notations and unit see figure 51.

6.4.3 Scenario "Sticky"

Due to the grazing pressure of zooplankton in the previous simulation, to see whether phytoplankton may escape zooplankton grazing in this scenario the stickiness has been increased to 0.5. Following the nitrate intrusion on day 218, this time the phytoplankton bloom only reaches a maximum concentration of 1.4 mmol N m^{-3}, but there are large aggregates (sinking faster than fecal pellets) during the time of the bloom (figure 58). These aggregates rapidly sink out and have reached a depth of 100 m a few days after the nitrate intrusion.

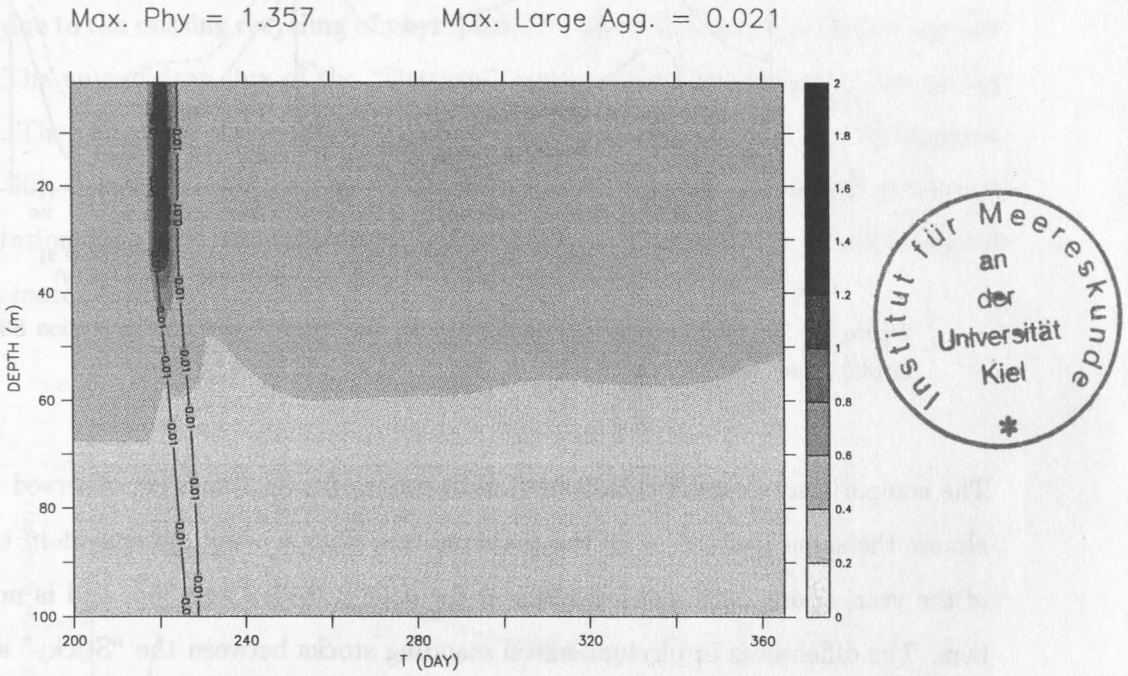

Figure 58: Mass of total phytoplankton and aggregates sinking faster than 10 m d^{-1} (minimum diameter $\approx$ 200 μm) for the "Sticky" scenario at station S04 with nitrate profile assimilation on day 218 (upper 100 m, day 200–365). Phytoplankton mass is shown by grey shades, mass of aggregates sinking faster than 10 m d^{-1} is shown by contour lines on semilogarithmic intervals. Unit is mmol N m^{-3}.

The pattern of zooplankton and fecal pellets are very similar to the results of the base model simulation after the nitrate intrusion. Maximum zooplankton concentration is about 1.7 mmol N m^{-3}, and maximum pellet concentration 0.4 mmol N m^{-3}, so the results are not shown here. The enhancement of aggregation is of course reflected in the sedimentation. Only a few days after the nitrate profile assimilation, sedimentation shows a distinct peak in both depths of 400 and 800 m, which consists almost excusively of phytoplankton (figure 59). After this peak, flux to a large extent consists of fecal pellets, which produce a second

peak in sedimentation at 400 m. Most of the fecal pellets degrade while settling through the water, so little of this peak reaches 800 m

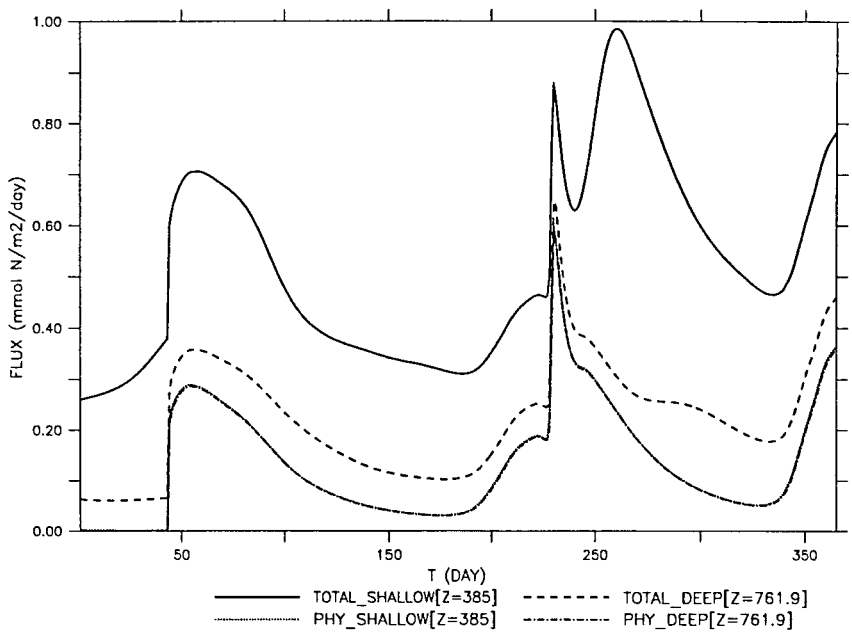

Figure 59: Sedimentation in 400 and 800 m for the "Sticky" scenario at station S04 with nitrate profile assimilation on day 218. For notations and units see figure 48.

The comparison of model chlorophyll and primary production with observed values show almost the same pattern as in the previous run, with a weak agreement in the first half of the year, and a quite good agreement for days 250, 319 and 354, and is not presented here. The differences in phytoplankton standing stocks between the "Sticky" scenario and the base model simulation occur mainly on days when no data are available, so no decision can be made which model fits the data better.

6.4.4 The "Detritus" scenario

Finally, another simulation has been performed in which again the phytoplankton mortality leads to the formation of detritus, which the sinks at a constant speed of 10 m d^{-1}. The development of the blooms and zooplankton over time are rather similar in their shape and timing, so no plots are shown here. Instead, table 7 combines the outcome of the simulations for all three scenarios. In the "Detritus" scenario, phytoplankton reach a much higher concentration of 2.1 mmol N m^{-3}, and its maximum is immediately followed by maximum zooplankton (almost 2 mmol N m^{-3}) and fecal pellets. Production in this model is lowered, due to the missing recycling of phytoplankton as implemented in the aggregation scenarios. The annual deep flux of the "Detritus" scenario is higher than the base model simulation. The reason for this result can be found in the annual pattern of sedimentation (see figure 60), because during non-bloom periods this model produces a higher baseline of sedimentation than the base simulation, in which the time dependence of sinking speed produces a more pronounced cycle.

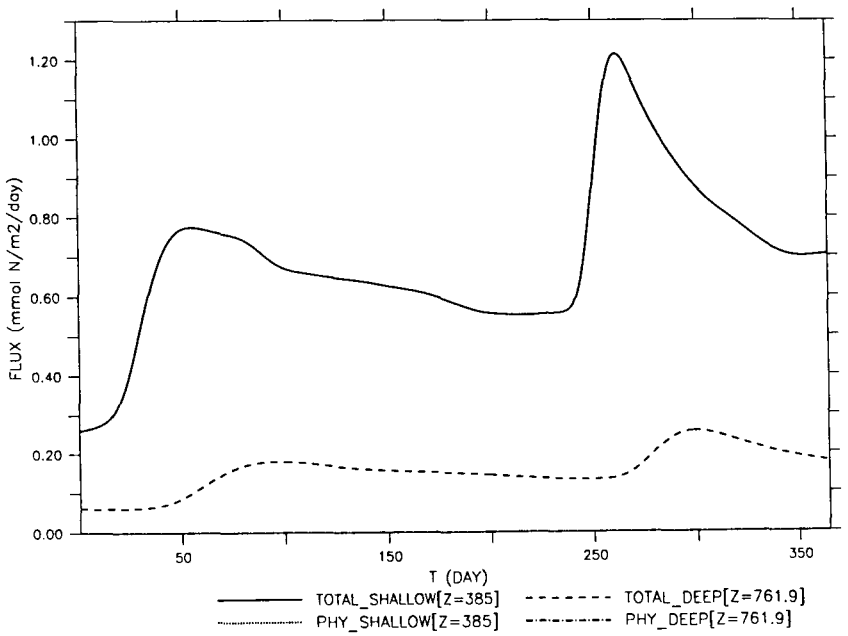

Figure 60: Sedimentation in 400 and 800 m for the "Detritus" scenario at station S04 with nitrate profile assimilation on day 218. For notations and units see figure 48.

6.4.5 Model and observed sedimentation at station S04

The "Sticky" model is able to reproduce a very distinct peak of sedimentation at both depths of 400 and 800 m immediately after the phytoplankton bloom. This peak to a large

Table 7: Annual primary production (PP) (integrated over depth), grazing (integrated over depth, given as percent of primary production), sedimentation through 800 m (F800) and max. phytoplankton, zooplankton and fecal pellets/detritus (max. PHY, max. ZOO and max. DET, respectively) for different simulations at station S04.

scenario	PP gC m^{-2}	Grazing % of PP	F800 g C m^{-2}	max. PHY mmol N m^{-3}	max ZOO mmol N m^{-3}	max DET mmol N m^{-3}
base	276	80	2.9	1.27	1.73	0.42
sticky	262	77	6.4	1.36	1.70	0.43
detritus	213	79	4.5	2.12	1.93	0.69

amount consists of phytoplankton, whereas in the model with low aggregation the peak either does not occur at all (climatological run) or is less pronounced and later (base run with nutrient intrusion). In chapter 5 it has been mentioned, that trap data give mostly averages over a week or even longer time period. This may have a tendency to flatten individual peaks. There is no way to re-examine the trap data with respect to the peaks that may have occured during their opening interval, so the model flux for the three runs have been averaged over the same interval as the opening times of the trap J3 at the same location, at about 800 m depth during 1995 deployed, sampled and measured by S. Honjo (in press). Figure 61 shows these manipulated model fluxes for the three model simulations with nitrate intrusion (base simulation, A, "Sticky" scenario B, and "Detritus" scenario, C). The base model and the detritus scenario after averaging over the trap sampling intervals do not show any peaks of sedimentation, and their flux pattern does not coincide with the observed fluxes. Having a constant detrital sinking speed or low aggregation as simulated by setting the stickiness to a low value, most of the matter that is exported by sedimentation comes in the form of fecal pellets. The time lag between phytoplankton bloom and peak sedimentation is too large when compared with the observed flux. Only the model scenario with a stickiness of 0.25 shows a peak during summer monsoon, which mainly consists of phytoplankton. Summarizing, at this site a rather high stickiness is necessary to simulate the flux pattern.

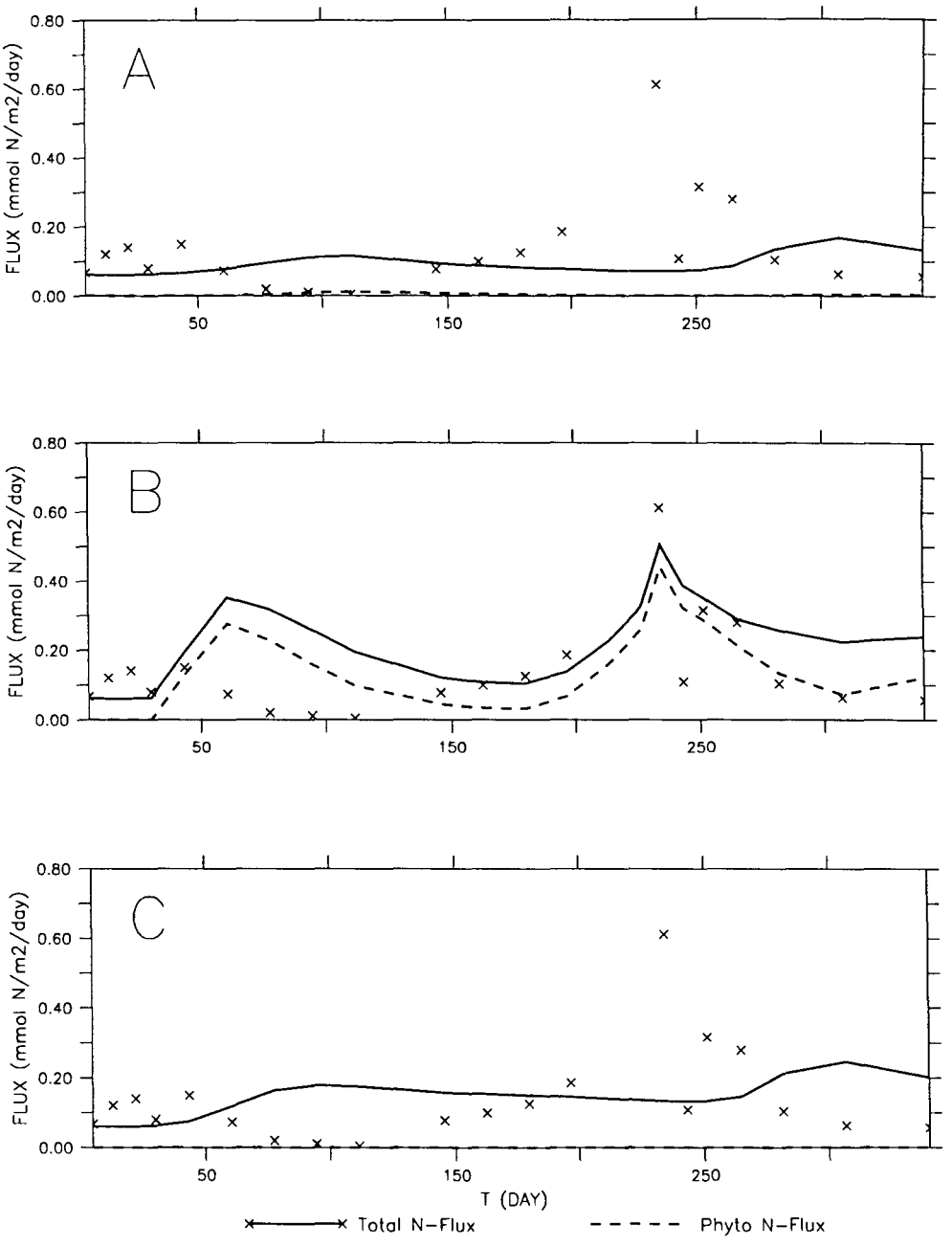

Figure 61: Phytoplankton and total sedimentation at 800 m for different model scenarios, together with local measurements of sedimentation on station S04 (S. Honjo, unpubl.). Panel A: base model simulation. Panel B: "Sticky" scenario. Panel C: "Detritus" scenario. Model results have been averaged over trap sampling intervals. Units are mmol N m^{-2} d^{-1}.

6.5 Comparison and discussion

The oligotrophic site in the central Arabian Sea Low values of Chl *a* concentrations (0.1 - 0.3 mg Chl *a* m^{-3}) with little variation over the year have been measured on cruises carried out by the International Indian Ocean Expedition (IIOE) in the mid 60's (ATLANTIS cruises 8 and 15 in August/ September 1963 and February/March 1965, respectively, Krey and Babenerd, 1976 .) Primary productivity on this site during May/July 1964 was about 0.3 g C m^{-2} d^{-1}, but also showed little variation throughout the year (Krey and Babenerd, 1976). Jochem *et al.* (1993) 1987 found a typical oligotrophic system in the open Arabian Sea, with a high turnover of nutrients in the surface layer, and a lower turnover in the subsurface maximum of chlorophyll. Annual primary production on this site was rather high in the model for the aggregation scenarios (260 and 245 g C m^{-2} y^{-1} for the base and sticky scenario, respectively) but lower for the detrital scenario (104 g C m^{-2} y^{-1}). The former value agrees with the annual primary production of 1995 as shown in figure 41, when integrating over depth and year, which gives about 230 g C m^{-2} y^{-1}, but it is much higher than the estimated annual primary production of 25 – 73 g C m^{-2} y^{-1} as presented by Krey (1973) for the open Indian Ocean.

This oligotrophic system showed little sedimentation. Pollehne *et al.* (1993b) using scanning electron microscopy found that a large amount of sedimentation on this station in May could be attributed to copepod fecal pellets, which contained diatom and coccolithophorid shells. The autotrophic organisms grew mainly in the DCM at about 50 m depth (max. Chl *a* about 1 mg Chl *a* m^{-3}), so the DCM was the main source of sedimentation via fecal pellet sedimentation, whereas in the mixed layer a recycling system of small phytoplankton was found. This finding corresponds with the results of section 6.3, where sedimentation happend mainly via fecal pellets. Sedimentation in 100 m caught with a drifting sediment trap was about 0.07 mmol N m^{-2} d^{-1}, which is less than the results of the model simulations for this site. The model for the oligotrophic site exports between 3 and 5 g C m^{-2} y^{-1} at 800 m, which is only slightly higher than the annual flux rates of 1.1 - 2.6 g C m^{-2} $^{-1}$ that have been found by Haake *et al.* (1993) for the years of 1986, 1987 and 1988 on a station at 14.5°N 64.8°E at about 3000 m depth.

The results of the model simulations are in good agreement with the data of the 1995 study, as well as with older results. At 10°N 65°E, phytoplankton growth is mainly controlled by the availability of nutrients that are mixed into the surface layers by mixed layer deepening

during both monsoon seasons. The model primary production and associated flows further depend on the model type that is used for this area: simulating phytoplankton mortality that immediately produces nutrients for phytoplankton growth greatly enhances primary production (base runs and scenario "Sticky"). As phytoplankton are controlled by nutrient supply (bottom-up) and never bloom with high concentrations, aggregation on this site is of minor importance to deep flux.

The site in the western Arabian Sea The results of the International Indian Ocean Expedition (IIOE) show a large spatial and temporal variability in Chl *a* and primary production values northwest of the Findlater Jet axis (Krey and Babenerd, 1976). Generally, primary production values and Chl *a* are higher in this area than in the central part of the Arabian Sea, with values around 0.3–0.5 mg Chl *a* m^{-3} averaged over the period from May to October, and lower (0.2 mg Chl *a* m^{-3}) during the rest of the year. The vertical pigment distribution was relatively uniform in August 1963 (ATLANTIS II, cruise 8, Krey and Babenerd, 1973), with values around 0.5 mg Chl *a* m^{-3}, which is very low when compared with CZCS data as for example, presented by Brock *et al.* (1991) for the year 1979, giving values as high as 5.0 mg Chl *a* m^{-3} for regions near the Oman coast. The latter findings are higher than the model output, when simulating a nutrient intrusion in August – when the model is run with a climatological forcing when comparing the model with the CZCS data it strongly underestimates the pigment concentrations. This model only on one day simulates an intrusion of nitrate into the mixed layer, but it is likely that larger amounts of nutrients are advected from the coastal upwelling (Morrison *et al.*, 1998). A more detailed investigation and modelling of the lateral processes on this site is necessary to examine the goodness of fit of the model to the data. The relatively good match of the model to the 1995 data may be misleading – the station has only been visited on eight days in a year, with a low temporal resolution especially during times of high production. It may be possible that there were far higher phytoplankton concentrations between the days of observation. For example, during the 1997 drift experiment the Chl *a* concentration in the coastal upwelling have been found to be as high as 4 mg Chl *a* m^{-3}, with a large amount of diatoms as indicated by biogenic silicate and Utermöhl countings. This bloom declined within a few days to values less than 1 mg Chl *a* m^{-3}. Due to the lack of observed data for this region, which shows a high spatial and temporal variability, a more adequate comparison would probably be the comparison of the output of an eddy-resolving three dimensional model

of ocean circulation and biogeochemistry with satellite ocean colour data, as for example provided by the SeaWiFS satellite which has been launched in 1997.

Integrated primary production for the whole year according to the data presented by Krey and Babenerd is always larger than 0.5 g C m^{-2} d^{-1} in this region, showing little variation throughout the year and giving a minimum annual integrated flux of at least 160 g C m^{-2}. Krey (1973) for the coastal upwelling gives a value of 124 g C m^{-2} y^{-1}. The model results are somewhat higher (213 - 276 g C m^{-2}), but reproduce the very high daily production rates that have been measured on various cruises (3.2 - 4.0 g C m^{-2} d^{-1} following the nitrate intrusion in the different model scenarios). When integrating the results of the 1995 primary production measurements on station S04 over depth and time, which gives about about 380 g C m^{-2} y^{-1}. The model lies within the range of these data, especially when considering that the model is likely to underestimate the nitrate concentrations that occur during SWM at this site (see above).

Little is known about the grazing pressure of zooplankton, especially mesozooplankton, on phytoplankton in this region. Burkill *et al.* (1993b) in September the nortwestern Arabian Sea found a large grazing pressure of microzooplankton on phytoplankton, especially *Synechococcus*. It is unclear whether copepods prefer aggregates for their diet. Schnack (1983) in the northwest African upwelling found that the copepod *Calanoindes carinatus* which also commonly occurs in the Arabian Sea, does not graze on phytoplankton aggregates of the genus *Thalassiosira parthenia*. Other autors have found grazing of copepods on phytoplankton aggregates (Bochdansky and Herndl, 1992a; Hansen, 1992; Lampitt *et al.*, 1993b). The high zooplankton biomasses that persist throughout the entire year in the Arabian Sea, and its ability to graze upon natural assemblages of diatoms e.g. off the Somali coast (Smith, 1982) suggest that its grazing pressure on phytoplankton in general must be strong.

Sedimentation in the western Arabian Sea has been found to be strictly coupled to the monsoonal forcing, i.e. to a decrease in surface water temperature after onset of the SWM (Haake *et al.*, 1993). The increase in organic carbon flux was first accompanied by an increase of carbonate, and about one month later, by an increase in biogenic silica sedimentation at 3000 m depth. Between 22 and 42 mmol N m^{-2} y^{-1} sedimented in the years from 1986-1990. This is about as much as the model sedimentation at 800 m depth, which lies between 38 and 81 mmol N m^{-2} y^{-1} for the simulations with low and high aggregation, respectively. Without setting the aggregation parameters to unrealistic high values (Engel,

1998; Alldredge and McGillivary, 1991), high aggregation produces the characteristic sedimentation signal at greater depths, which is often accompanied by high opal sedimentation. Nevertheless, mesozooplankton as large organisms can produce large, rapidly settling pellets (Noji, 1989), with sinking velocities of tens to hundreds of meters per day, so another method of increasing model sedimentation could theoretically be seen in increasing the pellet sinking speed in the model. This has not been done in this representation, because this would result in an increase in sedimentation even for the intermonsoon periods, which is not supported by the data.

It has been mentioned before that the model with the climatological forcing fails to reproduce the annual cycle of nitrate and other compartments. This region is likely to be influenced by lateral processes (Banse, 1987; McCreary *et al.*, 1996; Young and Kindle, 1994; Keen *et al.*, 1997; Morrison *et al.*, 1998). The simulation of nitrate supply used here should only serve as a first step towards a parameterization of the processes in this area. More detailed analysis and a more elaborate formulation for the processes that affect nutrient (as well and phyto- and zooplankton) concentrations in this region are necessary.

7 Discussion

7.1 The influence of aggregation in different oceanic regimes

Rapid mass sedimentation of intact phytoplankton cells following surface blooms, without mediation by zooplankton grazing and production of fast settling pellets has been reported for a variety of coastal (Peinert *et al.*, 1982; Smetacek, 1980) and open ocean regions (Billet *et al.*, 1983; Lampitt, 1985). Some of these studies suggest that marine aggregates containing phytoplankton cells play an important role for this mass transfer to the sea floor. On the other hand, zooplankton fecal pellets, which can sink at a speed of several tens to hundreds of meters per day (Noji, 1989), can be an important source of sedimentation to the ocen interior (Noji, 1991). Chapters 5 and 6 set out to distinguish the contribution of both of these processes, sedimentation mediated by phytoplankton aggregates and by fecal pellets, for three locations in the open ocean.

The results from the grid model with constant physical forcing showed that mainly bloom events are affected by aggregation and are sensitive to alterations in its parameters. When simulating aggregation a bloom a distinct peak of sedimentation occurs. Constant physical surroundings, as given by post-bloom oligotrophic periods are of little importance to total sedimentation on a time scale of 90 days. These results have been confirmed by model simulations that have been performed at different locations in the ocean, one situated in the northeastern North Atlantic, one in the western Arabian Sea, and one in the central Arabian Sea. The former two represent sites where phytoplankton at some times of the year find sufficient nutrients to bloom; the latter one represents an oligotrophic environment with little seasonality in its annual cycle of biogeochemical variables. Table 8 summarizes the results for model simulations for these oceanic regions, with respect to the quality and quantity of annual mean flows.

North Atlantic Aggregation plays an important role in the northeastern Nort Atlantic. It increases particle sinking speed and so a large amount of the spring bloom production is exported to depths below 800 m (5-11% of annual production). When simulating aggregation, most of the organic matter that sinks through the model bottom comes in the form of phytoplankton aggregates. The contribution of phytoplankton to total flux increases with depth, because phytoplankton aggregates have higher sinking speeds and thus are less affected by degradation than slower sinking fecal pellets. In both aggregation simulations,

Table 8: Annual primary production (PP) (integrated over depth), grazing (integrated over depth, given as percent of primary production) and sedimentation in 400 and 800 m for different simulations at three different locations: North Atlantic (47°N 20°W), western Arabian Sea (17°N 60°E) and central Arabian Sea (10°N 65°E).

Location scenario	PP g C m^{-2}	Grazing % of PP	Flux (400m) g C m^{-2}	% PHY	Flux (800m) g C m^{-2}	% PHY
North Atlantic 47°N 20°W						
base	218	57	18	62	11	86
sticky	172	47	23	81	19	94
detritus	179	58	27	-	7	-
Central Arabian Sea 10°N 65°E						
base	260	78	12	5	3	16
sticky	245	76	13	19	5	49
detritus	104	58	14	-	3	-
Western Arabian Sea 17°N 60°E						
base/climat	217	75	10	1	2	5
base	276	80	12	1	3	4
sticky	262	77	15	26	6	60
detritus	213	79	20	-	5	-

more than one half of the flux through 400 m reaches depths of 800 m and is lost from the system, but only 25% is lost in the model with a constant sinking speed. This result reveals the importance of aggregation for model simulations in this region - the nature as well as the quantity of sedimentation strongly depend on the model and the parameters that are used.

Simulating aggregation in the northeastern North Atlantic also decreases the duration of the spring bloom, and the time phytoplankton is available to zooplankton. Thus, aggregation has an effect on zooplankton grazing, which can be seen in the reduction of total and relative zooplankton grazing when increasing phytoplankton stickiness. Between 47% (high stickiness) and 58% (no aggregation) is grazed by zooplankton.

The model with low stickiness shows the highest annual primary production, which is even higher than the model that lacks aggregation at all. In the aggregation model, mortality of phytoplankton fuels the nitrate pool, whereas phytoplankton in the detrital model is lost

for further uptake by phytoplankton once it has died and has sunken out of the upper, well-lit layers as detritus.

Central Arabian Sea On the other hand, when the model is run at an oligotrophic site in the central Arabian Sea, where low phytoplankton concentrations can be found almost throughout the entire year, changes in the pattern of sedimentation are low. A large amount of annual phytoplankton production (which is even higher than in the northeastern North Atlantic) is grazed by model zooplankton (58 – 78% of phytoplankton production). The percentage as well as the absolute amount of phytoplankton production being grazed is lowest in the model lacking aggregation, the explanation of which has been given in the previous paragraph. As zooplankton in the base model in the upper 50 m is always > 0.3 mmol N m^{-3} in the aggregation runs throughout the whole year, but almost zero in the simulations for the North Atlantic for most times of the year, this model shows a high amount of recycling in the mixed layer due to grazing and excretion by zooplankton, which explains the rather high annual primary production when compared to the North Atlantic simulations. This coincides with the data: whereas in the North Atlantic zooplankton grazing pressure has been found to be of low importance to the decline of the phytoplankton spring bloom (Dam *et al.*, 1993), in the western Arabian Sea it has been hypothesized that mesozooplankton grazing on phytoplankton is the dominant pathway of carbon transformation during both Monsoon seasons (Smith *et al.*, 1998). Further offshore in the central Arabian Sea, where low biomasses of mesozooplankton have been found, most likely microzooplankton play a role in controlling the phytoplankton (Smith *et al.*, 1998; Landry *et al.*, 1998).

Due to the low aggregation, and the constant sinking speed of fecal pellets, seasonal changes in the sedimentation pattern at this site are low. The flux through 400 m is almost equal for all three simulations (12–14% of primary production), but the contribution of the different constituents (phytoplankton or pellets) varies considerably with the model, being low in the model with low or no aggregation, and highest in the model with high stickiness. Again the amount of phytoplankton in sinking matter increases with depth, being highest in the model with high stickiness where phytoplankton constitutes about half of the total sedimentation. Flux through 800 m is low (3-5 gC m^{-2}), which is about 1-3% of annual primary production, and due to the low influence of aggregation even highest for the model without aggregation.

When comparing the model run at a station in the **western Arabian Sea** with climatological forcing with the model runs where an intrusion of nitrate is simulated it can be seen, that the model with climatological forcing according to WOA produces the the lowest sedimentation flux in both depth horizons (10 and 2 gC m^{-2}, respectively), as well as the lowest grazing pressure on phytoplankton (75% of annual primary production). When resetting the nitrate profile measured data from August 1995, the resulting increase in primary production is almost balanced by an increase in zooplankton grazing, leading to little or no a small increase in in deep flux (1 and 3 gC m^{-2} in the climatological and intrusion model, respectively). This increase in deep flux is mainly due to increase in fecal pellet flux: in the intrusion model, phytoplankton only constitute 4% of the deep flux, but 5% in the climatological model. After a five fold increase in phytoplankton stickiness the deep flux and the contribution of phytoplankton increases, but also the grazing pressure. The latter effect has a strong impact on model behaviour.

Summarizing the results, it is clear that aggregation and its parametrization may play an important role in regions where (1) zooplankton grazing pressure is sufficiently low when phytoplankton starts to bloom and so (2) phytoplankton reach sufficient concentrations to trigger aggregation.

7.2 Implications for biogeochemical models

Theoretical ecology distinguishes between so-called "bottom-up"systems, in which the components of the system are controlled by the availability of their substrate, and "top-down" systems, where predators or grazers control the biological system. Following the analysis presented above, the central Arabian Sea may be classified as a " bottom-up" system, and self-regulation of phytoplankton (which is not considered in this concept at all) is unlikely to play a role in this region. On the opposite, the western Arabian Sea can be seen as a "top-down" system, where zooplankton grazing plays a large role for the development of the system when nutrients are entrained during the SWM. A third situation can probably been found during spring time in the northeastern North Atlantic, where phytoplankton at first are neither nutrient nor grazing limited but can grow almost at their maximum growth rate. In this system, self regulation of phytoplankton density may be of importance, as for example has been shown in chapter 5.

To account for a density-dependent control of phytoplankton biomass during bloom seasons,

some models use a density dependent loss term for phytoplankton mortality, for example for the Bermuda time series station (Hurtt and Armstrong, 1996; Gin *et al.*, 1998), or the northeastern North Atlantic (Oschlies, pers. comm.). Hurtt and Armstrong refer to aggregation when they assign a phytoplankton mortality depending on the square of the phytoplankton mass. As aggregation depends on the number concentration rather than on mass concentration, and as aggregation theory predicts these two measures can be decoupled, as aggregation conserved mass, but reduces numbers, the approach presented here seems to be a more realistic one.

As has been stated in the chapters before, the sinking speed of particles in the oceanic environment may vary over some orders of magnitudes (Smayda, 1970; Bienfang, 1981; Noji, 1989; Alldredge and Gotschalk, 1988). The variation in sinking speed, and sinking flux, can be due to different species compositions in the water column, to their nutritional status (Waite and Thompson, 1992; Waite *et al.*, 1992a; Waite *et al.*, 1992b) or, as for example presented in this work, due to aggregation of phytoplankton.

This variation can be of importance for the organisms living on the ocean floor, because it determines the amount and quality of food that supplies benthic organisms. It also determines how much, and how fast carbon, that has been fixed in the upper layers of the ocean, is being transported to the ocean interior. This may be of some importance for the global carbon cycle: if, for example, carbon is incorporated into particles in the coastal upwelling along the Arabian coast with its narrow shelf (see section 6.1 of chapter 6), and these waters are transported offshore via eddies and filaments, where surface current velocities may be around 0.5 m s^{-1} (Keen *et al.*, 1997, Dengler, unpubl. data), the rate at which these carbon rich particles sink determines where they will be deposited. If the particles sink fast enough, they will be deposited on the shelf and their carbon becomes available for surface production very soon. On the other hand, slow sinking particles might be transported further offshore, if they don't degrade before they reach the deep sea floor. This type of process can be of importance to three dimensional models (Young and Kindle, 1994; Keen *et al.*, 1997) that are concerned with sinking and deposition of organic matter. A more detailed analysis of the sinking speed in relation to the times scales of oceanic transport, or even the implementation of the aggregation equations presented here into a 3-dimensional model of ocean circulation and biogeochemistry is necessary to examine the effects of aggregation on carbon export to the ocean floor for this specific region.

7.3 Outlook: Model and reality

There exist a variety of processes which can modify the particle size structure, but are not considered in this model.

For example, zooplankton may cause breakage of aggregates when feeding on them. Although there is evidence of mesozooplankton feeding on marine aggregates, little is known about the nature of this feeding, whether zooplankton only extract mass out of the aggregates (i.e. bite off pieces), or whether there is selective feeding on certain size classes of aggregates, whether these aggregates are swallowed as a whole, or whether the aggregates are destroyed by zooplankton grazing and break apart.

As mentioned in chapter 5, although the aggregation model produces a realistic pattern of sedimentation, it overestimates the total flux that has been measured by sediment traps. One reason for this may be found in the inappropriate parameterization of the degradation and remineralization of marine aggregates. More work, and empirical evidence is needed to resolve the question whether aggreggates become heavier while sinking, because they scavenge heavy particles such as abiotic material or become colonized by zooplankton and bacteria, whether they dissolve, and become less dense and slower sinking, or whether they break up to small particles again. Breakup of aggregates in the mixed layer due to the forces exerted by turbulent shear has been discussed by many authors (McCave, 1984; Riebesell, 1991; Ruiz and Izquierdo, 1997), and work considering this process is in progress.

The model presented here involves the aggregation of living phytoplankton cells only. Considering the enrichment of fecal pellets or other organisms in aggregates, which has been found in reality (see chapter 2), would entail the modeling of more size-classes, which not only cover different size ranges, but also are of different physiological and ecological characteristics. Aggregates are partly dead organic matter, partly they are viable and photosynthesize. This model is restricted to one specific part of the pelagic ecosystem, namely phytoplankton, so it probably omits many important features. This is certainly a lack in the model structure. In reality, collision and aggregation takes place between all kinds of particles. Further, phytoplankton in aggregates may die, without being recycled to nutrients immediately, but their shells (in the case of diatoms), may remain in the aggregate. A further step in this modeling approach therefore has to be the parameterization of biological processes of aggregates, i.e. phytoplankton mortality and colonization by and scavenging of other organisms. The solution of the aggregation equations prior to model run time has

the disadvantage that this model has to consider the whole size range from some lower bound to infinity. The introduction of more sizeclasses with finite upper bounds would likely require many more, and more complicated equations, and more time to compute the model.

Another probably very important pathway of aggregate formation in the marine environment has been proposed by Passow *et al.* (1994). Passow *et al.* (1994) proposed that marine aggregates might originate from TEP (transparent exopolymer particles), which again might be formed via the aggregation of dissolved organic carbon (DOC) and colloidal particles excreted by phytoplankton. This step would involve the formation of particles from dissolved material not via biological processes, as it is the case in phytoplankton primary production and bacterial production, but via physical processes. In a model of this type, phytoplankton would additionally restrict their growth due to the exudation of DOC, which can form the primary matrix of marine aggregates and also increases their stickiness (Dam and Drapeau, 1995; Engel, 1998). Little is known about the qualitative nature of DOC. The model presented here is based on nitrogen, so the first thing that has to be known is the ratio at which phytoplankton excrete DOC and dissolved organic nitrogen (DON) and the minimum size of these particles. The validation of a model of this type would require measurements over a very large size range of particles, measured by various methods. For reasons mentioned in the second chapter, the methods that are applied until now for the measurement of the particle size spectrum have cannot be applied for the whole size spectrum. Hopefully, as modeling and measurement of the aggregates (in laboratory as well as in natural systems) is improved, a model that considers all of the important processes that govern the sinking of particles, and that helps us to understand their relationship and relative importance may one day become available.

8 Summary/Zusammenfassung

Summary

This work presents a model of phytoplankton aggregation, where the aggregation equations have been solved on a continuous size spectrum of phytoplankton, and implemented into 0-dimensional and 1-dimensional nitrogen based models of ocean biogeochemistry. The model only needs one additional variable (aggregate numbers) beside phytoplankton mass, and is of low computational cost. By simulating a changing size distribution, or a changing average aggregate size, the model computes the sinking speed of phytoplankton as a dependent variable. The results are compared with previous size-discrete models, as well as with measured data for different oceanic sites. The contribution of phytoplankton sedimentation in comparison to fecal pellet sedimentation is evaluated for different oceanic regions. The sensitivity of the model to alterations in its parameters and structure is investigated.

The **0-dimensional model** of phytoplankton aggregation on a continuous size spectrum for a mixed layer depth of 25 m reproduces the the development of the phytoplankton bloom very well, when compared with size-discrete models of phytoplankton aggregation. Increasing one of the parameters relevant for aggregation (stickiness or phytoplankton cell size) increases the amount of sedimentation, and the size and sinking speed of particles that sink out of the mixed layer. The largest effect is given by simulating colony formation. The qualitative nature of the experiments agrees well with the results of former, size discrete models, but the effects are small when compared with a model of non-aggregating phytoplankton.

The **1-dimensional model** in general shows the same results as the 0-dimensional model. Considering the sedimentation in 400 m, the largest effect of changing one of the relevant parameters is again given when simulating colony formation. Most of the model export can be attributed to the mixed layer phytoplankton bloom. Phytoplankton that grows beneath the mixed layer is only subject to aggregation due to differential settlement, which in this model setup is several orders of magnitude lower than aggregation due to shear, which takes place mainly in the mixed layer. Thus, the Deep Chlorophyll Maximum contributes little to sedimentation, except for the scenario with colony formation, where changes in sinking speed additionally happen due to the growth of phytoplankton. Aggregation promotes the

formation of a Deep Chlorophyll Maximum, because it reduces phytoplankton concentration in the upper layers, and together with the effect of self-shading of phytoplankton the sub-mixed layer phytoplankton has more light to grow. Again, the effects of changing one of the aggregation parameters are small when compared to model simulations with non-aggregating species.

The 1-dimensional NPZD model has been run for a site in the **Northeastern North Atlantic**, with a deep mixed layer and low concentrations of phytoplankton and zooplankton during winter. Aggregation enhances the peak as well as the annual amount of sedimentation especially at greater depths, compared to a model with a constant detrital sinking speed. The model reduces the amount of the spring bloom, that is left for post-bloom zooplankton grazing. The production of large aggregates is enhanced by increased stickiness. Most of the shallow and deep sedimentation after the spring bloom in the aggregation model can be attributed to phytoplankton. Fecal pellets, which in this model only sink at a constant sinking speed of 10 m d^{-1} only contribute to less than 15 % of the deep flux. Although the model probably overestimates the sedimentation as measured by sediment traps, aggregation is likely to play an important role not only for sedimentation of organic matter on this site, but also for the development of the biological system of the upper layers after the phytoplankton spring bloom.

The 1-dimensional NPZD model when run for a site in the **Central Arabian Sea**, with little variation of mixed layer depth during the year, shows little sensitivity to the introduction of aggregation or changes in phytoplankton stickiness. Phytoplankton never reach high concentrations, and so aggregation at this site seems to be of minor importance. Sedimentation in the model simulations mostly consists of fecal pellets. The model shows a good fit to the data.

The 1-dimensional NPZD model has been run for a site in the **Western Arabian Sea**, which is likely to be affected by lateral advection of nutrients during the Southwest Monsoon. The model forcing by a mixed layer climatology has been found to be insufficient, so a nitrate profile that has been measured in August 1995 has been assimilated to the model. The model then shows a large influence of aggregation on timing and amount of the sedimentation peak following the phytoplankton bloom after nutrient input during the Southwest Monsoon. While giving a quite good fit to the data (nitrate, Chl *a* and primary

production) the model with high stickiness at the same time reproduces the peak of sedimentation very well, when model results are averaged over trap sampling intervalls. This peak could not be reproduced by a model with low stickiness, or without aggregation at all. The sensitivity of the model to aggregation on this site is lower than in the simulations for the Northeastern North Atlantic. This lower sensitivity can be attributed to the high grazing pressure, that in this model type on this station is exerted by zooplankton.

Summarizing, aggregation when simulated with a biogeochemical model and a continuous size spectrum of phytoplankton is of large importance for sedimentation especially on stations where phytoplankton growth is unlimited by nutrients or by zooplankton grazing, as it is the case in the northeastern North Atlantic, or eventually in the Arabian Sea during the Southwest Monsoon. The model is efficient enough (in terms of time it takes to compute the equations) to be incorporated into highly resolved vertical models of ocean biogeochemistry, or perhaps into 3-dimensional models of ocean circulation, as it does not disturb the reproduction of annual cycles in the biological variables in regions where aggregation is of minor importance, while at the same time it simulates aggregation and rapid mass sedimentation in regions where this process may be necessary to consider.

Zusammenfassung

In dieser Arbeit wird ein Modell für Phytoplanktonaggregation präsentiert, in dem die Aggregationsgleichungen und die Sedimentation auf einem kontinuierlichen Größenspektrum des Phytoplanktons gelöst, und in 0- und 1-dimensionale Modelle für die biogeochemischen Kreisläufe des Ozeans implementiert wurden. Das Modell benötigt neben der Gleichung für die Phytoplanktonmasse lediglich eine zusätzliche Variable (Anzahl der Aggregate), und somit wenig zusätzliche Rechenzeit. Da in dem Modell die Größenverteilung des Phytoplanktons bzw. dessen durchschnittlicher Durchmesser zu jedem Zeitschritt neu berechnet wird, berechnet das Modell auch die Sinkgeschwindigkeit des Phytoplanktons als abhängige Variable zu jedem Zeitschritt neu.
Die Ergebnisse des Modells werden mit den Ergebnissen anderer, größenklassendiskreter Aggregationsmodelle verglichen, sowie mit gemessenen Daten für verschiedene ozeanische Seegebiete. Für die einzelnen Regionen wurde der Anteil der Phytoplanktosedimentation im Vergleich zu der Sedimentation von Zooplanktonkotballen berechnet. In Experimenten wurde die Empfindlichkeit des Modells in Bezug auf Änderungen in seinen Parametern oder seiner Modellstruktur getestet.

Das **0-dimensionale Modell** für Phytoplanktonaggregation, das mit einer konstanten Tiefe der durchmischten Schicht von 25 m gerechnet wurde, gibt die Entwicklung der Phytoplanktonblüte und -größenverteilung im Vergleich mit größenklassendiskreten Modellen sehr gut wieder. Eine Erhöhung der für die Aggregation relevanten Parameter, wie die Klebrigkeit der Phytoplanktonaggregate oder der Zelldurchmesser des Phytoplanktons führen zu einer Erhöhung der Sedimentation aus der Deckschicht, sowie zu einer Erhöhung der Größe und damit der Sinkgeschwindigkeit des sedimentierenden Materials. Der größte Effekt wird jedoch erzielt, wenn die Bildung von Kolonien simuliert wird. Die Ergebnisse der Experimente stimmen in ihrer Qualität gut mit den Ergebnissen der Experimente mit größenklassendiskreten Modellen überein, die Effekte sind jedoch gering im Vergleich mit einem Modell, das nicht Aggregation, sondern Detritus mit einer konstanten Sinkgeschwindigkeit simuliert.

Das **1-dimensionale Modell** für Phytoplanktonaggregation, aufgelöst bis zu einer Tiefe von 400 m, zeigt mit einer bei 25 m konstanten Deckschicht die gleichen Ergebnisse wie das 0-dimensionale Modell. Der größte Effekt von Änderungen der Parameter in Bezug

auf Sedimentation in 400 m wird wiederum durch die Simulation von Koloniebildung erzielt. Das Phytoplankton der Deckschicht stellt den größten Anteil der Sedimentation in dieser Tiefe, da das Phytoplankton unterhalb der Deckschicht lediglich aufgrund von unterschiedlichen Sinkgeschwindigkeiten aggregiert, dessen Kollisionswahrscheinlichkeit in diesem Modell mehrere Größenordnungen geringer ist als die Kollisionen aufgrund turbulenter Scherkräfte in der Deckschicht. Daher kann das sogenannte tiefe Chlorophyllmaximum nicht als eine Quelle der Sedimentation angesehen werden. Eine Ausnahme bildet das Experiment mit Koloniebildung, in dem die Zunahme der Größe der Aggregate nicht an Aggregation, und damit physikalische Prozesse gebunden ist, sondern zusätzlich an biologische Prozesse (Phytoplanktonwachstum). Aggregation fördert die Ausbildung eines tiefen Chlorophyllmaximums, da die Konzentration des Phytoplanktons in der Deckschicht herabgesetzt wird, und somit die Selbstbeschattung des Phytoplanktons. Das Phytoplankton in tieferen Schichten bekommt somit mehr Licht zur Phytosynthese . Auch in diesem Modell sind die Auswirkungen von Änderungen der Parameter gering im Vergleich mit den Auswirkungen, die ein Weglassen der Aggregation in einem Modell mit konstant sinkendem Detritus hat.

Es wurden Simulationen mit dem 1-dimensionalen NPZD Modell für den **Nordöstlichen Nordatlantik** durchgeführt. In diesem Seegebiet, in dem während der tiefen winterlichen Durchmischung geringe Phytoplankton- und Zooplanktonkonzentrationen in der Deckschicht vorgefunden werden, führt die Simulation von Aggregation im Vergleich zu einem Modell ohne Aggregation zu einer Erhöhung des Sedimentationssignals nach der Frühjahrsblüte. Darüberhinaus reduziert Aggregation den Anteil des Phytoplanktons, der nach der Früjahrsblüte dem Zooplankton zum Fraß zur Verfügung steht, und verringert damit die maximale Zooplanktonkonzentration. Der größte Teil der Sedimentation in größeren Tiefen (400 und 800 m) besteht aus Phytoplankton. Nur ein kleiner Teil der Sedimentation ist Zooplanktonkotballen, die mit 10 m Tag^{-1} sinken, zuzuschreiben (weniger als 15%). Obwohl das Modell die Maxima der Sedimentation sowie die jährliche Sedimentation überschätzt, ist es sehr wahrscheinlich das Aggregation in dieser Region eine wichtige Rolle nicht nur für die Sedimentation spielt, sondern auch für die der Frühjahrsblüte folgende Entwicklung des pelagischen biologischen Systems.

In Simulationen mit dem 1-dimensionalen NPZD Modell für die **Zentrale Arabische See**,

die im Verlauf des Jahres nur geringe Variationen in der tiefe der durchmischten Schicht zeigt, zeigte sich ein geringer Einfluß der Aggregation, und eine geringe Empfindlichkeit des Modells in Bezug auf Variationen der Aggregationsparameter. Dieser geringe Einfluß der Aggregation kann auf die relativ niedrigen Phytoplanktonkonzentrationen zurückgeführt werden, die in diesem Seegebiet vorzufinden sind und auch simuliert werden. Der größte Teil der Sedimentation erfolgt in Form von Zooplanktonkotballen. Das Modell zeigt gute Übereinstimmung mit den 1995 gemessenen Daten (Nitrat, Chl *a*, Primärproduktion).

Weiterhin wurden Simulationen mit dem Modell in der **Westlichen Arabischen See** durchgeführt, auf einer Station, die wahrscheinlich durch laterale Advektion von Nährstoffen aus dem Küstenauftrieb beeinflußt wird. Da der Antrieb des Modells über eine Klimatologie der Tiefe der durchmischten Schicht diesen Prozeß nicht ausreichte um einen entsprechenden Nährstoffeintrag zu simulieren, wurde Nitratdaten aus einer Messung im August 1995 in das Modell assimiliert. Dieses Modell zeigt dann einen hohen Einfluß der Aggregation in Bezug auf Ausmaß und Zeitpunkt des Sedimentationssignals nach dem Nährstoffeintrag während des Südwestmonsuns. Während alle Experimente die 1995 gemessenen Daten (Nitrat, Chl *a*, Primärproduktion) relativ gut wiederegeben, zeigt nur das Modell mit hoher Klebrigkeit eine gute Anpassung in seinem Sedimentationssignal an die Sinkstoffallendaten aus dieser Zeit (Modellergebnisse gemittelt über die Fallenfangintervalle) . Der etwas niedrigere Einfluß der Aggregation in dieser Region kann auf den hohen Fraßdruck des Zooplanktons in diesem Modell zurückgefürt werden werden.

Zusammenfassend läßt sich feststellen, daß die Simulation von Aggregation in einem Modell für die biogeochemischen Prozesse des Ozeans insbesondere in Regionen, in denen das Phytoplanktonwachstum nicht oder nur gering durch Nährstoffmangel und/oder Zooplankton limitiert ist, von Bedeutung ist. Dieses ist z.B. im nordöstlichen Nordatlantik oder in der westlichen Arabischen See zur Zeit des Südwestmonsuns der Fall. Das Modell ist effizient genug, um in vertikal hoch aufgelöste Modelle der marinen pelagischen Biologie eingebaut zu werden, eventuell auch in 3-dimensionale Modell der ozeanischen Zirkulation. In letzteren könnte es sowohl in oligotrophen Regionen, in denen die Aggregation von untergeordneter Bedeutung ist, die jährlichen Zyklen der biogeochemischen Bestandteile wiedergeben, als auch Regionen simulieren, in denen Aggregation eine Rolle spielen kann.

References

Alldredge, A.L. and Gotschalk, C. (1988). In situ settling behaviour of marine snow. *Limnol. Oceanogr.*, **33**(3), 339–351.

Alldredge, A.L. and Gotschalk, C. (1989). Direct observations of the mass flocculation of diatom blooms: characteristics, settling velocities and formation of diatom aggregates. *Deep-Sea Res.*, **36**(2), 159–171.

Alldredge, A.L. and Gotschalk, C. (1990). The relative contribution of marine snow of different origins to biological processes in coastal waters. *Cont. Shelf Res.*, **10**(1), 41–58.

Alldredge, A.L. and McGillivary, P. (1991). The attachment probabilities of marine snow and their implications for particle coagulation in the ocean. *Deep-Sea Res.*, **38**(4), 431–443.

Alldredge, A.L. and Silver, M.W. (1988). Characteristics, dynamics and significance of marine snow. *Progress in Oceanography*, **20**(41–82).

Alldredge, A.L., Gotschalk, C., Passow, U. and Riebesell, U. (1995). Mass aggregation of diatom blooms: Insights from a mesocosm study. *Deep-Sea Res. II*, **42**(1), 9–27.

Banse, K. (1987). Seasonality of phytoplankton chlorophyll in the central and northern Arabian Sea. *Deep-Sea Res.*, **34**, 713–723.

Banse, K. (1994). On the coupling of hydrography, phytoplankton, zooplankton, and settling organic particles offshore in the Arabian Sea. *Proc. Indian Acad. Sci. (Earth Planet. Sci.)*, **103**(2), 125–161.

Bauer, S., Hitchcock, G.L. and D.B.Olson (1993). Response of the Arabian Sea surface layer to monsoon forcing. *Pages 659–672 of:* Desai, B.N. (ed), *Oceanography of the Indian Ocean.* Balkema.

Beaulieu, S.E. and Smith Jr., K.L. (1998). Phytodetritus entering the benthic boundary layer and aggregated on the sea floor in the abyssal NE Pacific: macro- and microscopic composition. *Deep-Sea Res. II*, **45**, 781–815.

Bienfang, P.K. (1981). Sinking rates of heterogenous phytoplankton populations. *J. Plank. Res.*, **3**(2), 235–253.

Billet, D.S.M., Lampitt, R.S., Rice, A.L. and Mantoura, R.F.C. (1983). Seasonal sedimentation of phytoplankton to the deep-sea benthos. *Nature*, **302**, 520–522.

Bochdansky, A.B. and Herndl, G.H. (1992a). Ecology of amorphous aggregations (marine snow) in the Northern Adriatic Sea. III. Zooplankton interactions with marine snow. *Mar. Ecol. Progr. Ser.*, **87**, 135–146.

Bochdansky, A.L. and Herndl, G.J. (1992b). Ecology of amorphous aggregations (marine snow) in the Northern Adriatic Sea. V. Role of fecal pellets in marine snow. *Mar. Ecol. Progr. Ser.*, **89**, 297–303.

Brock, J., Sathyendranath, S. and Platt, T. (1994). A model study of seasonal mixed-layer production in the Arabian Sea. *Proc. Indian Acad. Sci. (Earth Planet. Sci.)*, **103**(2), 65–78.

Brock, J.C., McClain, C.R., Luther, M.E. and Hay, W.W. (1991). The phytoplankton bloom in the northwestern Arabian Sea during the southwest monsoon of 1979. *J. Geophys. Res.*, **96**(C11), 20623–20642.

Brock, J.C., McClain, C.R. and Hay, W.W. (1992). A southwest monsoon hydrographic climatology for the northwestern Arabian Sea. *J. Geophys. Res.*, **97**(C6), 9455–9465.

Brock, J.S., Sathyendranath, S. and Platt, T. (1993). Modeling the seasonality of subsurface light and primary production in the Arabian Sea. *Mar. Ecol. Progr. Ser.*, **3**, 209–221.

Brock, T.D. (1981). Calculating solar radiation for ecological studies. *Ecol. Model.*, **14**, 1–19.

Brown, P. N., Byrne, G. D. and Hindmarsh, A. C. (1989). VODE: A Variable Coefficient ODE Solver. *SIAM J. Sci. Stat. Comput.*, **10**, 1038 - 1051.

Burkill, P.H., Mantoura, R.F.C. and Owens, N.J.P. (1993a). Biogeochemical cycling in the northwestern Indian Ocean: a brief overview. *Deep-Sea Res. II*, **40**(3), 643–649.

Burkill, P.H., Leakey, R.J.G., Owens, N.J.P. and Mantoura, R.F.C. (1993b). *Synechococcus* and its importance to the microbial foodweb of the northwestern Indian Ocean. *Deep-Sea Res. II*, **40**(3), 773–782.

Chipman, D.W., Marra, J. and Takahashi, T. (1993). Primary production at 47°N 20°W in the North Atlantic Ocean: a comparison between the ^{14}C incubation method and the mixed layer carbon budget. *Deep-Sea Res. II*, **40**(1/2), 151–169.

Dam, H.G. and Drapeau, D.T. (1995). Coagulation efficiency, organic–matter glues and the dynamics of particles during a phytoplankton bloom in a mesocosm study. *Deep-Sea Res. II*, **42**(1), 111–123.

Dam, H.G., Miller, C.A. and Jonasdottir, S.H. (1993). The trophic role of mesozooplankton at 47°N, 20°W during the North Atlantic Bloom Experiment. *Deep-Sea Res. II*, **40**(1/2), 197–212.

Deckers, M. (1991). *Artenzusammensetzung, Biomasse und Sedimentation des Phytoplanktons von zwei Driftexperimenten im Nordostatlantik im Mai/Juni 1989.* M.Phil. thesis, Institut für Meereskunde, Kiel.

Ducklow, H.W. and Harris, R.P. (1993). Introduction to the JGOFS North Atlantic Bloom Experiment. *Deep-Sea Res. II*, **40**(1/2), 1–8.

Engel, A. (1998). *Bildung, Zusammensetzung und Sinkgeschwindigkeiten mariner Aggregate.* Ber. Institut für Meereskunde, Kiel 300. Christian–Albrechts–Universität zu Kiel, 145 pp.

Eppley, R.W., Rogers, J.N. and McCarthy, J.J. (1969). Half-saturation constants for uptake of nitrate and ammonium by marine phytoplankton. *Limnol. Oceanogr.*, **14**, 912–920.

Evans, G.T. (1998). The role of local models and data sets in the Joint Global Ocean Flux Study. *Deep-Sea Res.*, submitted.

Evans, G.T. and Garçon, V. (1997). *One-dimensional models of water column biogeochemistry.* JGOFS Report 23. Bergen, Norway, 85 pp.

Evans, G.T. and Parslow, J.S. (1985). A model of annual plankton cycles. *Biol. Oceanogr.*, **3**, 327–347.

Fasham, M.J.R. and Evans, G.T. (1995). The use of optimization techniques to model marine ecosystem dynamics at the JGOFS Station at 47° N, 20° W. *Phil. Trans. Roy. Soc. Lond. B*, **348**, 203–209.

Fasham, M.J.R., Ducklow, H.W. and McKelvie, S.M. (1990). A nitrogen-based model of plankton dynamics for the oceanic mixed layer. *J. Mar. Res.*, **48**, 591–639.

Findlater, J. (1969). A major low-level air current near the Indian Ocean during the northern summer. *Quarterly Journal of Research of the Meteorological Society*, **95**, 362–380.

Fowler, S.W. and Knauer, G.A. (1986). Role of large particles in the transport of elements and organic compounds through the oceanic water column. *Prog. Oceanog.*, **16**, 147–194.

Gelbard, F., Tambour, Y. and Seinfeld, J.H. (1980). Sectional representations for simulating aerosol dynamics. *Journal of Colloid and Interface Science*, **76**(2), 541–556.

Gin, K.Y.H, Guo, J. and Cheong, H.-F. (1998). A size based ecosystem model for pelagic waters. *Ecol. Model.*, **112**, 53–72.

Haake, B., Ittekkot, V., Rixen, T., Ramaswamy, V., Nair, R.R. and Curry, W.B. (1993). Seasonality and interannual variability of particle fluxes to the deep Arabian Sea. *Deep-Sea Res.*, **40**(7), 1323–1344.

Hansen, F.C. (1992). *Zooplankton Grazing an* Phaeocystis *mit besonderer Berücksichtigung der calanoiden Copepoden.* Ber. Institut für Meereskunde 229. Christian-Albrechts-Universität zu Kiel, 137 pp.

Haupt, O.J. (1995). *Modellstudien zum pelagischen Stickstoffumsatz und vertikalen Partikelfluß in der Norwegensee.* Berichte aus dem Sonderforschungsbereich 313 60. Christian-Albrechts-Universität zu Kiel, 140 pp.

Hill, P.S. (1992). Reconciling aggregation theory with observed vertical fluxes following phytoplankton blooms. *J. Geophys. Res.*, **97**(c2), 2295–2308.

Honjo, S. and Manganini, S.J. (1993). Annual biogenic particle fluxes to the interior of the North Atlantic Ocean studied at 23°N 21°W and 48°N 21°W. *Deep-Sea Res. II*, **40**(1/2), 587–607.

Honjo, S., Doherty, K.W., Agrawal, Y.C. and Asper, V.L. (1984). Direct optical assessment of large amorphous aggregates (marine snow) in the deep ocean. *Deep-Sea Res.*, **31**, 67–76.

Hurtt, G.C. and Armstrong, R.A. (1996). A pelagic ecosystem model calibrated with BATS data. *Deep-Sea Res. II*, **43**(2/3), 653–683.

Hustedt, F. (1930). Die Kieselalgen. *Chap. 7, page 845pp. of: Rabenhorst's Kryptogamen-Flora von Deutschland, Österreich und der Schweiz.* Leipzig: Akademische Verlagsgesellschaft.

Jackson, G.A. (1990). A model for the formation of marine algal flocs by physical coagulation processes. *Deep-Sea Res.*, **37**(8), 1197–1211.

Jackson, G.A. and Lochmann, S.E. (1992). Effect of coagulation on nutrient and light limitation of an algal bloom. *Limnol. Oceanogr.*, **37**(1), 77–89.

Jackson, G.A., Logan, B.E., Alldredge, A.L. and Dam, H.G. (1995). Combining particle size spectra from a mesocosm experiment measured using photographic and aperture impedance (Coulter and Elzone) techniques. *Deep-Sea Res. II*, **42**(1), 139–157.

Jochem, F. J., Pollehne, F. and Zeitzschel, B. (1993). Productivity regime and phytoplankton size structure in the Arabian Sea. *Deep-Sea Res. II*, **40**(3), 711–735.

Jonasz, M. and Fournier, G. (1996). Approximation of the size distribution of marine particles by a sum of log-normal distributions. *Limnol. Oceanogr.*, **41**(4), 744–754.

Kaltenböck, E. and Herndl, G.J. (1992). Ecology of amorphous aggregations (marine snow) in the Northern Adriatic Sea. IV. Dissolved nutrients and the autotrophic component associated with marine snow. *Mar. Ecol. Progr. Ser.*, **87**, 147–159.

Keen, T.R., Kindle, J.C. and Young, D.K. (1997). The interaction of Southwest Monsoon upwelling, advection and primary production in the northwest Arabian Sea. *J. Mar. Systems*, **13**(1-4), 61–82.

Kilps, J.R., Logan, B.E. and Alldredge, A.L. (1994). Fractal dimensions of marine snow determined from image analysis of in-situ photographs. *Deep-Sea Res.*, **41**(8), 1159–1169.

Kiørboe, T., Andersen, K.P. and Dam, H.G. (1990). Coagulation efficiency and aggregate formation in marine phytoplankton. *Mar. Biol.*, **107**, 235–245.

Krey, J. (1973). Primary Production of the Indian Ocean. *Chap. 2.1, pages 155–126 of:* Zeitzschel, B. (ed), *The Biology of the Indian Ocean.* Berlin: Springer.

Krey, J. and Babenerd, B. (1976). *Phytoplankton production.* Atlas of the International Indian Ocean Expedition. Institut für Meereskunde an der Christian-Albrechts-Universität Kiel, 70 pp.

Lambert, C.E., Jehanno, C., Silverberg, N., Brun-Cottan, J.C. and Chesselet, R. (1981). Log-normal distribution of suspended particles in the open ocean. *J. Mar. Res.*, **39**(1), 77–98.

Lampitt, R.S. (1985). Evidence for the seasonal deposition of detritus to the deep-sea floor and its subsequent resuspension. *Deep-Sea Res.*, **32**(8), 885–897.

Lampitt, R.S., K.F. Wishner, C.M. Turley and Angel, M.V. (1993a). Marine snow studies in the Northeast Atlantic Ocean: distribution, composition and role as a food source for migrating plankton. *Mar. Biol.*, **116**, 689–702.

Lampitt, R.S., Hillier, W.R. and Challenor, P.G. (1993b). Seasonal and diel variation in the open ocean concentration of marine snow aggregates. *Nature*, **362**, 737–739.

Landry, M.R., Brown, S.L., L.Campbell, Constantinou, J. and Liu, H. (1998). Spatial patterns in phytoplankton growth and microzooplankton grazing in the Arabian Sea during monsoon forcing. *Deep-Sea Res. II*, in press.

Lee, C., Murray, D.W., Barber, R.T., Buesseler, K.O., Dymond, J., Hedges, J.I., Honjo, S., Manganini, S.J., Marra, J., Mosers, C., Peterson, M.L., Prell, W.L. and Wakeham, S.G. (1998). Particulate organic carbon fluxes: Results from the U.S. JGOFS Arabian Sea Process Study by the Arabian Sea Carbon Flux Group. *Deep-Sea Res. II*, in press.

Lenz, J., Morales, A. and Gunkel, J. (1993). Mesozooplankton standing stock during the North Atlantic spring bloom study in 1989 and its potential grazing pressure on phytoplankton: a comparison between low, medium and high latitudes. *Deep-Sea Res. II*, **40**(1/2), 559–572.

Li, X. and Logan, B.E. (1995). Size distributions and fractal properties of particles during a simulated phytoplankton bloom in a mesocosm. *Deep-Sea Res. II*, **42**(1), 125–138.

Lochte, K., Ducklow, H.W., Fasham, M.J.R. and Stienen, C. (1993). Plankton succession and carbon cycling at 47°N 20°W during the JGOFS North Atlantic Bloom Experiment. *Deep-Sea Res. II*, **40**(1/2), 91–114.

McCave, I.N. (1984). Size spectra and aggregation of suspended particles in the deep ocean. *Deep-Sea Res.*, **31**(4), 329–352.

McCreary, J.P., Kohler, K.E., Hood, R.R. and Olson, D.B. (1996). A four-component ecosystem model of biological activity in the Arabian Sea. *Prog. Oceanog.*, **37**, 193–240.

Meyerhöfer, M. (1994). *Plankton-Pigmente und deren Abbauprodukte als Biomarker zur Beschreibung und Abschätzung der Phytoplankton-Sukzession und -Sedimentation im Nordatlantik.* Ber. Institut für Meereskunde 251. Christian-Albrechts-Universität zu Kiel, 188 pp.

Morrison, J., Codispoti, L.A., Gaurin, S., Jones, B., Manghnani, V. and Zheng, Z. (1998). Seasonal variation of hydrographic and nutrient fields during the U.S. JGOFS Arabian Sea Process Study. *Deep-Sea Res. II*, in press.

Mullin, M.M, Sloan, P. R. and Eppley, R. W. (1966). Relationship between carbon content, cell volume, and area in phytoplankton. *Limnol. Oceanogr.*, **11**, 307–311.

Noji, T. (1989). *The influence of zooplankton on sedimentation in the Norwegian Sea.* Ber. Sonderforschungsbereich 313 17. Christian-Albrechts-Universität zu Kiel, 183 pp.

Noji, T. (1991). The influence of macrozooplankton on vertical particulate flux. *Sarsia*, 1–9.

Passow, U., Peinert, R. and Zeitzschel, B. (1993). Distribution and sedimentation of organic matter during the intermonsoon period off Oman (West Arabian Sea). *Deep-Sea Res. II*, **40**(3), 573–568.

Passow, U., Alldredge, A.L. and Logan, B.E. (1994). The role of particulate carbohydrate exudates in the flocculation of diatom blooms. *Deep-Sea Res.*, **41**(2), 335–357.

Peinert, R., Saure, A., Stegmann, P., Stienen, C., Haardt, H. and Smetacek, V. (1982). Dynamics of primary production and sedimentation in a coastal ecosystem. *Neth. Jour. Sea Res.*, **16**, 276–289.

Pollehne, F., Klein, B. and Zeitzschel, B. (1993a). Low light production and export production in the deep chlorophyll maximum layer in the northern Indian Ocean. *Deep-Sea Res. II*, **40**(3), 737–752.

Pollehne, F., Zeitzschel, B. and Peinert, R. (1993b). Short-term sedimentation patterns in the northern Indian Ocean. *Deep-Sea Res. II*, **40**(3), 821–831.

Pruppacher, H.R. and Klett, J.D. (1978). *The microphysics of clouds and precipitation.* Dordrecht: Riedel.

Reed, R.K (1976). On estimating insolation over the ocean. *Journal of Physical Oceanography*, **7**, 482–485.

Riebesell, U. (1991). Particle aggregation during a diatom bloom. I. Physical aspects. *Mar. Ecol. Progr. Ser.*, **69**, 273–280.

Riebesell, U. and Wolf-Gladrow, D. (1992). The relationship between physical aggregation of phytoplankton and particle flux: a numerial model. *Deep-Sea Res.*, **39**(7/8), 1085–1102.

Ruiz, J. and Izquierdo, A. (1997). A simple model for the break-up of marine aggregates by turbulent shear. *Oceanologica Acta*, **20**(4), 597–605.

Schnack, S. (1983). On the feeding of copepods on *Thalassiosira parthenia* from the Northwest African upwelling area. *Mar. Ecol. Progr. Ser.*, **11**, 49–53.

SCOR (1992). *Joint Global Ocean Flux Study Implementation Plan.* JGOFS Report 9. Bergen, Norway, 78 pp.

SCOR (1995). *JGOFS Arabian Sea Process Study.* JGOFS Report 17. Bergen, Norway, 64 pp.

Shaw, T.J., Smoak, J.M. and Lauermann, L. (1998). Scavenging of ex^{234}Th, ex^{230}Th and ex^{210}Pb by particulate matter in the water column of the California Continental Margin. *Deep-Sea Res. II*, **45**, 763–779.

Shetye, S. R., Gouveia, A. D. and Shenoi, S. S. C. (1994). Circulation and water masses of the Arabian Sea. *Proc. Indian Acad. Sci. (Earth Planet. Sci.)*, **103**(2), 9–25.

Smayda, T.J. (1970). The suspension and sinking of phytoplankton in the sea. *Mar. Biol. Ann. Rev.*, **8**, 353–414.

Smayda, T.J. and Boleyn, B.J. (1965). Experimental observations on the flotation of marine diatoms. II. *Skeletonema costatum* and *Rhizosolenia setigera*. *Limnol. Oceanogr.*, **11**, 18–34.

Smetacek, V. (1980). Annual cycle of sedimentation in relation to plankton ecology in Western Kiel Bight. *Ophelia, Suppl.*, **1**, 65–76.

Smetacek, V.S. (1985). Role of sinking in diatom life-history cycles: ecological, evolutionary and geological significance. *Mar. Biol.*, **84**, 239–251.

Smith, S., Roman, M., Wishner, K., Gowing, M., Codispoti, L., Barber, R., Marra, J., Prusova, I. and Flagg, C. (1998). Seasonal response of mesozooplankton to monsoonal reversals in the Arabian Sea. *Deep-Sea Res. II*, in press.

Smith, S.L. (1982). The northwestern Indian Ocean during the monsoons of 1979: distribution, abundance, and feeding of zooplankton. *Deep-Sea Res.*, **29**(11A), 1331–1353.

Smith, S.L. (1984). Biological indications of active upwelling in the northwestern Indian Ocean in 1964 and 1979, and a comparison with Peru and northwest Africa. *Deep-Sea Res.*, **31**, 951–967.

Smith, S.L., Banse, K., Cochran, J.K., Codispoti, L.A., Ducklow, H.W., Luther, M.E., Olson, D.B., Peterson, W.T., Prell, W.L., Surgi, N., Swallow, J.C. and Wishner, K. (1991). *US JGOFS: Arabian Sea Process Study.* US JGOFS Planning Rep. 13. Woods Hole Oceanographic Institution, Woods Hole, Massachusetts.

Stachowitsch, M., Fanuko, N. and Richter, M. (1990). Mucus aggregates in the Adriatic Sea: An overview on stages and occurences. *Mar. Ecol. Progr. Ser.*, **11**(4), 327–350.

Steele, J.H. and Henderson, E.W. (1992). The role of predation in plankton models. *J. Plank. Res.*, **14**(1), 157–172.

Waite, A., Bienfang, P.K. and Harrison, P.J. (1992b). Spring bloom sedimentation in a subarctic ecosystem. I. Nutrient sensitivity. *Mar. Biol.*, **114**.

Waite, A., Bienfang, P.K. and Harrison, P.J. (1992a). Spring bloom sedimentation in a subarctic ecosystem. II. Succession and sedimentation. *Mar. Biol.*, **114**, 131–138.

Waite, A.M. and Thompson, P.A. (1992). Does energy control the sinking rates of marine diatoms? *Limnol. Oceanogr.*, **37**(3), 468–477.

Young, D.K. and Kindle, J.C. (1994). Physical processes affecting the availability of dissolved silicate for diatom production in the Arabian Sea. *J. Geophys. Res.*, **99**(C11), 22619–22632.

Zuur, E.A.H. and Nyffeler, F. (1992). Theoretical distributions of suspended particles in the ocean and a comparison with observations. *J. Mar. Systems*, **3**, 529–538.

A Solutions

A.1 Aggregation in the 0D-model

The solution for the integral for collisions due to shear can be found evaluating the integral of the shear kernel as given in Jackson (1990) over the integral $[m,\infty) \times [m,\infty)$, and substituting PHYNOS for $A\,m^{1-\epsilon}/(1-\epsilon)$:

$$\begin{aligned}\xi_{shear} &= A^2 shear\, 0.163 \int_m^\infty \int_m^\infty (\theta+\Theta)^3 \theta^{-\epsilon}\Theta^{-\epsilon}\,\mathrm{d}\theta\,\mathrm{d}\Theta \\ &= 2A^2 shear\, 0.163 m^{5-2\epsilon} FF \\ &= 2 shear\, 0.163\, \mathrm{PHYNOS}^2 m^3 (1-\epsilon)^2 FF \end{aligned} \tag{37}$$

with

$$FF = \frac{1}{(4-\epsilon)(1-\epsilon)} + \frac{3}{(2-\epsilon)(3-\epsilon)}$$

The solution for the integral for collisions due to differential settlement can be found evaluating the integral of the settlement kernel as given in Jackson (1990) over the integral $[m,\infty) \times [m,\Theta]$, and substituting PHYNOS for $A\,m^{1-\epsilon}/(1-\epsilon)$:

$$\begin{aligned}\xi_{sett} &= 0.125\,\pi\,2\,A^2 B \int_m^\infty \int_m^\Theta \theta^2(\Theta^\eta - \theta^\eta)\theta^{-\epsilon}\Theta^{-\epsilon}\,\mathrm{d}\theta\,\mathrm{d}\Theta \\ &= 0.125\,\pi\,2\,A^2 B m^{4+\eta-2\epsilon} FF \\ &= 0.125\,\pi\,2\,\mathrm{PHYNOS}^2\, m^2\, w_m\, (1-\epsilon)^2\, FF \end{aligned} \tag{38}$$

where w_m is the sinking speed of one cell, and

$$\begin{aligned} FF = {} & \frac{1}{(1+\eta-\epsilon)(3-\epsilon)} - \frac{\eta}{(4+\eta-2\epsilon)(3-\epsilon)(3+\eta-\epsilon)} \\ & - \frac{1}{(3+\eta-\epsilon)(1-\epsilon)} \end{aligned}$$

A.2 Sedimentation in the 1D-model

Let

$$F_M = \left(\frac{M}{m}\right)^{1-\epsilon(z)}$$

be the fraction of particles being larger than the upper bound, M, and $w_M = BM^\eta$ the constant sinking speed of particles larger than M, $w_m = bm^\eta$ the sinking speed of a single cell and $w(z,\theta) = B\,\theta^\eta$ the size dependent sinking speed of a particle smaller than M. The equation for sedimentation of numbers of particles with $p(z,\theta) = A\,\theta^{\epsilon(z)}$ being the number distribution at a certain depth is then

$$\begin{aligned}\Phi(z) &= A\,\frac{C}{dz}\left[\int_m^M p(z,\theta)\; w(z,\theta)\mathrm{d}\theta + \int_M^\infty p(z,\theta)\; w_M \mathrm{d}\theta\right] \\ &= \text{PHYNOS}\left(\frac{(1-\epsilon(z))\,w_m}{1+\eta-\epsilon(z)} + \frac{F_M\,\eta\,w_M}{1+\eta-\epsilon(z)}\right)\end{aligned}$$

If the mass of a particle of size θ is described by $C\;\theta^\zeta$ and if the fraction of mass of particles larger than M is given by

$$Fmass_M = \left(\frac{M}{m}\right)^{1+\zeta-\epsilon(z)}$$

then

$$\begin{aligned}\Psi(z) &= A\,\frac{C}{dz}\left[\int_m^M p(z,\theta)\;\theta^\zeta\; w(z,\theta)\mathrm{d}\theta + \int_M^\infty p(z,\theta)\;\theta^\zeta\; w_M \mathrm{d}\theta\right] \\ &= \text{PHY}\left(\frac{(1+\zeta-\epsilon(z))\,w_m}{1+\zeta+\eta-\epsilon(z)} + \frac{Fmass_M\;\eta\;w_M}{1+\zeta+\eta-\epsilon(z)}\right)\end{aligned}$$

The expression in in large brackets corresponds to the average mass sinking rate as presented for example in Fasham *et al.* (1990), or to the $\bar{w}$ as described in chapter 3, equation 21.

A.3 Aggregation in the 1D-model

For the evaluation of collisions due to shear, there are four double integrals to be solved:

$$\begin{aligned}I_1 &= \int_m^M\int_m^M \beta_{shear}(\theta,\Theta)p(z,\theta)p(z,\Theta)\mathrm{d}\theta\mathrm{d}\Theta \\ &= 0.163\,shear\,PHYNOS^2 \\ &\quad 2\left[(F_M-1)(F_M M^3-m^3)\frac{1-\epsilon(z)}{4-\epsilon(z)}\right. \\ &\quad \left.+3(F_M M-m)(F_M M^2-m^2)\frac{(1-\epsilon(z))(1-\epsilon(z))}{(2-\epsilon(z))(3-\epsilon(z))}\right] \\ I_2 &= \int_m^\infty\int_m^M \beta_{shear}(\theta,\Theta)\;p(z,\theta)\;p(z,\Theta)\mathrm{d}\theta\mathrm{d}\Theta \\ &= 0.163\,shear\,PHYNOS^2 \\ &\quad F_M\left[\left(M^3+3\left(M^2 m\frac{1-\epsilon(z)}{2-\epsilon(z)}+Mm^2\frac{1-\epsilon(z)}{3-\epsilon(z)}\right)+m^3\frac{1-\epsilon(z)}{4-\epsilon(z)}\right)\right. \\ &\quad \left.-F_M M^3\left(1+3\left(\frac{1-\epsilon(z)}{2-\epsilon(z)}+\frac{1-\epsilon(z)}{3-\epsilon(z)}\right)+\frac{1-\epsilon(z)}{4-\epsilon(z)}\right)\right] \\ I_3 &= \int_m^M\int_M^\infty \beta_{shear}(\theta,\Theta)\;p(z,\theta)\;p(z,\Theta)\mathrm{d}\theta\mathrm{d}\Theta = I_2 \\ I_4 &= \int_M^\infty\int_M^\infty \beta_{shear}(\theta,\Theta)\;p(z,\theta)\;p(z,\Theta)\mathrm{d}\theta\mathrm{d}\Theta \\ &= 0.163\,shear\,PHYNOS^2\,F_M\,F_M\,8\,M^3\end{aligned}$$

The number of particles colliding due to shear forces, ξ_{shear} is then given by the sum of these four integrals:

$$\xi_{shear}(z) = I_1 + I_2 + I_3 + I_4 = I_1 + 2\,I_2 + I4 \tag{39}$$

Because particles larger than size M thereafter sink at a constant speed, the evaluation for the number of collisions due to differential settlement can be presented as follows, with TS_M giving the relationship between the sinking rate of large particles to the sinking rate of one single cell:

$$TS_M = \left(\frac{M}{m}\right)^{\eta} \tag{40}$$

$$\begin{aligned}
I_1 &= 2\int_m^M \int_m^\theta \beta_{sett}(\theta,\Theta)\; p(z,\theta)\; p(z,\Theta)\mathrm{d}\theta\mathrm{d}\Theta \\
&= 2\,\pi\,8\,\zeta\; PHYNOS^2\;(1-\epsilon(z))^2\; w_m \\
&\quad \left[\frac{(T_M\,T_M\,M^2\,TS_M - m^2)\,\eta}{(3+\eta-\epsilon(z))(3-\epsilon(z))(4+\eta-2\epsilon(z)))}\right. \\
&\quad \left. +m^2\left(\frac{(1-T_M\,TS_M)}{(3-\epsilon(z))(1+\eta-\epsilon(z))} - \frac{1-T_M}{(3+\eta-\epsilon(z))(1-\epsilon(z))}\right)\right] \\
I_2 &= \int_M^\infty \int_m^M \beta_{sett}(\theta,\Theta) p(z,\theta) p(z,\Theta)\mathrm{d}\theta\mathrm{d}\Theta \\
&= 2\,\pi\,8\,(1-\epsilon(z))\; PHYNOS^2\; T_M\; w_m \\
&\quad \left[TS_M\frac{m^2 - T_M\,M^2}{3-\epsilon(z)} - \frac{m^2 - T_M M^2 TS_M}{3+\eta-\epsilon(z)}\right] \\
I_3 &= \int_m^M \int_M^\infty \beta_{sett}(\theta,\Theta)\; p(z,\theta)\; p(z,\Theta)\mathrm{d}\theta\mathrm{d}\Theta = I_2 \\
I_4 &= 2\int_M^\infty \int_M^\infty \beta_{sett}(\theta,\Theta)\; p(z,\theta)\; p(z,\Theta)\mathrm{d}\theta\mathrm{d}\Theta = 0
\end{aligned}$$

The number of particles colliding due to shear forces, ξ_{sett} is then given by the sum of these four integrals:

$$\xi_{sett}(z) = I_1 + I_2 + I_3 + I_4 = I_1 + 2I_2 \tag{41}$$

Then the sum of equations 39 and 41 times stickiness give the loss of particles due to aggregation:

$$\xi(z) = 0.5\; stick(\xi_{shear}(z) + \xi_{sett}(z)) \tag{42}$$

B List of Symbols

α	initial slope of P-I curve
$\beta(\theta, \Theta)$	kernel of aggregation function
ϵ	size distribution exponent
ϵ_{zoo}	assimilation efficiency of zooplankton
κ_{ZOO}	quadratic zooplankton mortality
λ_{PHY}	mortality rate of phytoplankton
λ_{ZOO}	excretion rate of zooplankton
λ_{DET}	degradation rate of detritus
ψ	mass sedimentation flux
ϕ	number sedimentation flux
ξ	number of particles aggegregating
μ_{PHY}	maximum growth rate of phytoplankton
η	sinking exponent
ζ	N content exponent
θ, Θ	agggregate diameter
A	size distribution coefficient
B	sinking coefficient
b	breakup probability
C	N content coefficient
C_m	mass of one cell
k_c	attenuation coefficient of phytoplankton
k_w	attenuation coefficient of water
k_{NO3}	half-sat. const. for NO3 uptake
M	upper boundary of size class
MLD	mixed layer depth
m	lower boundary of sizeclass (= cell diameter)
N	average aggregate size
N_{sink}	average aggregate size in sinking matter
$P(\theta)$	cumulative number distribution function
$p(\theta)$	number distribution function
NO3	nitrate concentration
DET	detritus mass concentration
PHY	phytoplankton mass concentration
PHYNOS	phytoplankton number concentration
shear	shear rate
stick	stickiness
$w(\theta)$	size - sinking relationship
w_m	minimum sinking speed (= cell sinking speed)
w_M	maximum sinking speed
w_{DET}	sinking speed of detritus
$\bar{w}$	average mass sinking speed of phytoplankton
ZOO	zooplankton mass concentration

Danksagung

Ich danke herzlich meinem Doktorvater, Prof. B. Zeitzschel, für die Betreuung, für seine Unterstützung und für das Vertrauen, das er meinen Ideen und meiner Arbeit entgegenbrachte.

Ebenfalls für die ausgezeichnete Betreuung, die Ratschläge, Hinweise wie auch Ermutigung danke ich Dr. Geoffrey T. Evans. Ohne seine Hilfe wäre diese Arbeit nicht zustande gekommen. Vielen Dank!

Eine große Hilfe waren Dr. Andreas Oschlies und Joanna Waniek, die sich der Mühe unterzogen haben, die Arbeit zu kommentieren. Vielen herzlichen Dank.

Ein Dank geht weiterhin an die Arbeitsgruppe "JGOFS Arabische See", Dr. Klaus v. Bröckel, Dr. Ute Zeller, Claudia Sellmer und Kerstin Petuhov, für die zahlreichen Diskussionen und Hinweise über die Biologie der Arabischen See, sowie der wissenschaftlichen und technischen Besatztung der Forschungschiffe für das angenehme Arbeitsklima während der Reisen METEOR 32/5 und SONNE 120.

Thomas Mitzka, als JGOFS Datenmanager und Zimmernachbar, war zu jeder Zeit zu Diskussionen und zur Hilfe bereit. Ihm ein herzliches Dankeschön für angenehme drei Jahre.

Ich danke den Mitarbeitern der Abteilung Marine Planktologie für ihre Hilfsbereitschaft, Freundlichkeit und Kollegialität. Insbesondere Peter Fritsche und Kerstin Nachtigall, die den größten Teil der auf M32/5 erhobenen Daten gemessen und bei der Auswertung geholfen haben, gebührt mein herzlicher Dank. Anja Engel hat mir mit ihrem Wissen über die Biologie mariner Aggregate sehr geholfen. Uwe Fehner hat mir die Sinkstoffallendaten der NABE/BIOTRANS Station zur Verfügung gestellt. Danke!

Ich danke weiterhin Dr. L. Codispoti, Dr. R. Barber und Prof. S. Honjo, daßsie mir die Daten der US JGOFS Arabian Sea Process Study 1995 zur Verfügung gestellt haben, sowie C. Hammond für die äußerst benutzerfreundliche Bereitstellung der Daten im World Wide Web.

Ich danke ich meinem Mann Matthias Kriest: ohne seine Geduld, seine Unterstützung, vor allem aber seine Fähigkeit, mir zu zeigen, daß es noch andere wichtige Dinge neben dieser Arbeit gibt, hätte ich diese Arbeit nicht so gelassen fertiggestellt. Gleichzeitig danke ich meinem Sohn Johannes: dem strahlendsten kleinen Sonnenschein, den es gibt!

BERICHTE AUS DEM INSTITUT FÜR MEERESKUNDE
Verzeichnis der veröffentlichten Arbeiten

(Auskünfte über die vorangegangenen Veröffentlichungen erteilt die Bibliothek)

250 (1994)	SAYIN, E.	Modelling Water and Salt Exchange through the Belt and Sound
251 (1994)	MEYERHÖFER, M.	Plankton-Pigmente und deren Abbauprodukte als Biomarker zur Beschreibung und Abschätzung der Phytoplankton-Sukzession und -Sedimentation im Nordatlantik
252 (1994)	THETMEYER, H.	Respiration von *Gobiusculus flavescens* und *Pomatoschistus minutus* bei spontaner Schwimmaktivität
253 (1994)	QUACK, B.	Leichtflüchtige Halogenkohlenwasserstoffe in der marinen Atmosphäre: Bestand, Herkunft und Massenbilanzen über Nord- und Ostsee
254 (1994)	REUSCH, T.B.H.	Factors structuring the *Mytilus*- and *Zostera*-community in the Western Baltic: an experimental approach (Strukturbestimmende Faktoren für die *Mytilus*- und *Zostera*-Gemeinschaft der westlichen Ostsee: ein experimenteller Ansatz)
255 (1994)	KOEVE, W.	New Production of Phytoplankton in the tropical and subarctic North Atlantic
256 (1994)	OSCHLIES, A.	Assimilation of Satellite Altimeter Data into an Eddy-Resol Primitive Equation Model of the North Atlantic Ocean
257 (1994)	DÖSCHER, R.	Die thermohaline Zirkulation in einem numerischen Modell Nordatlantischen Ozeans: quasistationäre Zustände und Adapt tionsprozesse
258 (1994)	KRAUSS, W.	Sonderforschungsbereich 133 "Warmwassersphäre des Atlantiks" — Eine Dokumentation —
259 (1994)	NEHRING, ST.	Dinoflagellaten-Dauercysten in deutschen Küstengewässern: Vorkommen, Verbreitung und Bedeutung als Rekrutierungspotential
260 (1994)	HOLFORT, J.	Großräumige Zirkulation und meridionale Transporte im Südatlantik
261 (1994)	KÖSTER, F.W.	Der Einfluß von Bruträubern auf die Sterblichkeit früher Jugendstadien des Dorsches *(Gadus morhua)* und der Sprotte *(Sprattus sprattus)* in der zentralen Ostsee
262 (1994)	AUF DEM VENNE, H.	Zur Verbreitung und ökologischen Bedeutung planktischer Ciliaten in zwei verschiedenen Meeresgebieten: Grönlandsee und Ostsee
263 (1995)	DETMER, A.	Verbreitung, Abundanz und Bedeutung von autotrophem Pico- und Nanoplankton in polaren, temperierten und subtropischen Regionen
264 (1995)	HUMBORG, CH.	Untersuchungen zum Verbleib der Nährstoff-Frachten der Donau
265 (1995)	DIAZ, H.F. ISEMER, H.-J.	Proceedings of the International COADS Winds Workshop, Kiel, Germany, May 31 — June 2, 1994 (In Verbindung mit National Oceanic and Atmospheric Administration NOAA)
266 (1995)	WIELAND, K.	Einfluß der Hydrographie auf die Vertikalverteilung und Sterblichkeit der Eier des Ostseedorsches *(Gadus morhua callarias)* im Bornholmbecken, südliche zentrale Ostsee

267 (1995)	FUHRHOP, R.	Fehleranalyse passiver Mikrowellenmessungen des Special Sensor Microwave / Imager
268 (1995)	PULFRICH, A.	Reproduction and Recruitment in Schleswig-Holstein Wadden Sea Edible Mussel *(Mytilus edulis L.)* Populations
269 (1995)	HEISE, S.	Der Einfluß von Umweltfaktoren auf die Bildung von exopolymerer Substanz (EP) durch ein marines Bakterium
270 (1995)	SENOCAK, T.	Schwermetalluntersuchung an Fischen der deutschen Ostseeküste (Kliesche *Limanda limanda;* Flunder *Platichthys flesus;* Hering *Clupea harengus* und Dorsch *Gadus morhua*)
271 (1995)	SCHORIES, D.	Populationsökologie und Massenentwicklung von *Enteromorpha* spp. (Chlorophyta) im Sylter Wattenmeer
272 (1995)	KÖRTZINGER, A.	Anthropogenes CO_2 im Nordatlantik Methodische Entwicklungen und Messungen zur Quantifizierung des anthropogenen CO_2-Signals
273 (1995)	DAHMEN, K.	Vertikalverteilung und produktionsbiologische Bedeutung des Mesozooplanktons im Bornholm-Becken (Südliche Ostsee)
274 (1995)	SCHRADER, M.	Ein Dreiskalenmodell zur Berechnung der Reflektivität der Ozeanoberfläche im Mikrobwellenfrequenzbereich
275 (1995)	PALM, H.W.	Untersuchungen zur Systematik von Rüsselbandwürmern (Cestoda: Trypanorhyncha) aus atlantischen Fischen
276 (1995)	PIKER, L.	Dynamik der Sulfatatmung und ihre Bedeutung für die Kohlenstoff-Mineralisierung in Ostsee-Sedimenten
277 (1995)	BLANZ, TH.	Dokumentation und Massenbilanz des Chlorbiphenyl-Eintrags der Oder in die Südpommersche Bucht
278 (1995)	GROSSKLAUS, M.	Niederschlagsmessung auf dem Ozean von fahrenden Schiffen
279 (1995)	NEUGUM, A.	Systematische Einflüsse auf die Bestimmung der Schubspannung mit der "Dissipationsmethode" auf See
280 (1995)	PFANNKUCHE, O. HOPPE, H.-G. THIEL, H. WEIKERT, H.	BIO-C-FLUX — Biologischer Kohlenstoffffluß in der bodennahen Wasserschicht des küstenfernen Ozeans Schlußbericht für den Förderzeitraum 1.1.1990-31.12.1994
281 (1995)	ZANGENBERG, N.	Die Zirkulation des Oberflächen- und des Tiefenwassers im Südlichen Brasilianischen Becken
282 (1995)	HEVIA, M.	Ein Simulationsmodell zum Einfluß intensiver Lachszucht auf die Umwelt und Auswirkungen standortbedingter Umweltparameter auf das Wachstum des atlantischen Lachses *(Salmo salar L.)* an der Küste Chiles
283 (1996)	LUNDGREEN, U.	Aminosäuren im Nordatlantik: Partikelzusammensetzung und Remineralisierung

284 (1996)	MEIER, H.E.M.	Ein regionales Modell der westlichen Ostsee mit offenen Randbedingungen und Datenassimilation
285 (1996)	THUROW, F.	Estimation of the total fish biomass in the Baltic Sea during the 20th centry
286 (1996)	EFTHIMIOU,S.	Performance of juvenile and ongrowing common Dentex (Dentex dentex, L. 1758, Sparidae) in relation to nutrition under culture
287 (1997)	STUTZER, S.	Modellierung der mittleren Zirkulation im Südatlantik
288 (1997)	SIEDLER, G. ZENK, W.	Untersuchungen zu den tiefen Wassermassen und planktologische Beobachtungen im tropischen Westpazifik während der SONNE-Fahrt Nr. 113 (TROPAC)
289 (1997)	JAHN, A.	Ökophysiologische Untersuchungen an *Macoma balthica* (Bivalvia) und *Cyprideis torosa* (Ostracoda) über Anpassungen an den Umweltfaktor Schwefelwasserstoff
290 (1997)	SANDERS, D.	Alkenone in sedimentierenden Partikeln im Nordostatlantik: Regionale und saisonale Variabilität
291 (1997)	BRUHN, R.	Chlorierte Schadstoffe in Schweinswalen *(Phocoena phocoena)*: Verteilung, Akkumulation und Metabolismus in Abhängigkeit vor Struktur
292 (1997)	SEILERT, H.E.W.	Freilanduntersuchungen zur Verteilung der Miesmuschel *Mytilu edulis L.* in einem zweifach geschichteten Ästuar
293 (1997)	KAREZ, R.	Factors causing the zonation of three *Fucus* species (Phaeophyta) in the intertidal zone of Helgoland (German Bight, North Sea) Testing the validity of Keddy's 'competitive hierarchy model'
294 (1997)	DYNAMO GROUP	DYNAMO – Dynamics of North Atlantic Models: Simulation and assimilation with high resolution models
295 (1997)	DONNER, G.	Beziehungen zwischen Struktur und Funktion bakterieller Gemeinschaften in Mikrokosmos- und Freiwasser-Chemoklinen
296 (1997)	WIRYAWAN, B.	Mesozooplankton dynamics in the northern Adriatic Sea and the influence of eutrophication by the river Po
297 (1997)	FUHRHOP, R. SIMMER, C. SCHRADER, M. HEYGSTER, G. JOHNSEN, K.-P. SCHLÜSSEL, P.	Study of Remote Sensing of the atmosphere and surface ice
298 (1997)	BROWN, A.W.	Mikroorganismen als mögliche Indikatoren zur Beurteilung des Wasser- und Sedimentzustandes im Bereich küstennaher Zuchtanlagen für die Regenbogenforelle *(Oncorhynchus mykiss)*
299 (1997)	WIEDEMEYER, W.	Analysis of the benthic food web of a mangrove ecosystem at noreastern Brazil

300 (1998)	ENGEL, A.	Bildung, Zusammensetzung und Sinkgeschwindigkeiten mariner Aggregate
301 (1998)	BIASTOCH, A.	Zirkulation und Dynamik in der Agulhas-Region anhand eines numerischen Modells
101 (1982)	SIEDLER, G.	SI-Einheiten in der Ozeanographie SI Units in Oceanography
(1988)		2. revidierte Auflage
(1998)		3. revidierte Auflage
302 (1998)	KNOLL, M. MÜLLER, T.J. SIEDLER, G.	ESTOC/CANIGO cruises with FS POSEIDON: cruises 202/1, 212, 233, 237/3
303 (1998)	LOTZE, H.K.	Population dynamics and species interactions in macroalgal blooms: abiotic versus biotic control at different life-cycle stages
304 (1998)	FÜG, C.	Validierung des hydrologischen Zyklus des BALTEX-Gebietes im Regionalmodell REMO mit Mikrowellenbeobachtungen vom Satelliten aus
305 (1999)	RICK, S.	The spring bloom in the German Bight: Effects of high inorganic N:P ratios on the phytoplankton development
306 (1999)	KRIEST, I.	The influence of phytoplankton aggregation on sedimentation - A model study